Measurement and Assignment of the Size-Dependent Optical Spectrum in Cadmium Selenide (CdSe) Quantum Dots

by

David J. Norris

B.S. Chemistry
University of Chicago, 1990

Submitted to the Department of Chemistry
in Partial Fulfillment of the Requirements
for the Degree of

DOCTOR OF PHILOSOPHY

at the

MASSACHUSETTS INSTITUTE OF TECHNOLOGY

September 1995

Signature of Author_____
Department of Chemistry
August 2, 1995

Certified by_____
Moungi G. Bawendi
Associate Professor of Chemistry
Thesis Supervisor

Accepted by_____
Dietmar Seyferth
Chairman, Departmental Committee on Graduate Students

This doctoral thesis has been examined by a Committee of the Department of Chemistry as follows:

Professor Robert W. Field _____
Chairman

Professor Moungi G. Bawendi _____
Thesis Supervisor

Professor Bruce Tidor _____

Measurement and Assignment of the Size-Dependent Optical Spectrum in Cadmium Selenide (CdSe) Quantum Dots

by

David J. Norris

Submitted to the Department of Chemistry on August 2, 1995
in Partial Fulfillment of the Requirements for the Degree of
Doctor of Philosophy in Chemistry

Abstract

In this thesis the size-dependent optical properties of nanometer-scale semiconductor crystallites (or quantum dots) are investigated. Recently developed synthetic methods are utilized to fabricate a series of high quality, nearly monodisperse, cadmium selenide (CdSe) quantum dots with mean diameters ranging from ~24Å to ~105Å. Transient differential absorption (TDA), photoluminescence excitation (PLE), and fluorescence line narrowing (FLN) spectroscopies are used to extract "single dot" absorption and emission information. The size dependence of ten quantum dot absorption features is presented. Comparison with theoretical predictions allows six of the transitions to be confidently assigned. The most likely assignments for the remaining four are discussed. The size dependent data exhibit two avoided crossings, demonstrating the importance of valence band structure in the description of the excited states. In addition to this electronic structure, fine structure in the lowest quantum dot transition is discussed. Fine structure has been predicted to occur due to the crystal field and non-spherical shape of our dots, as well as the electron-hole exchange interaction. Since the lowest excited sublevel is predicted to be optically forbidden, the fine structure has important implications in quantum dot emission. Relaxation of the excited dot into this level, referred to as the "dark exciton", can explain the extremely long radiative lifetimes (~1μs at 10K) observed in these systems, an effect previously attributed to surface traps. Experimental evidence for the fine structure is presented in size-dependent absorption and emission results. Comparison of the experimental data with theoretical predictions strongly confirms the presence of the "dark exciton" and the fine structure in the lowest quantum dot transition.

Thesis Supervisor: Moungi G. Bawendi, Ph.D.
Title: Associate Professor of Chemistry

for my dearest Beth

Table of Contents

Section I

Chapter 1

Introduction

1.1 Definition: What is a Quantum Dot?

With the improvement of epitaxial growth techniques (e.g. MBE, MOCVD) and micro-characterization methods (e.g. TEM) in the 1970s and early 80s, solid state physicists began to investigate "quantum structures". The earliest quantum structure to be fabricated and studied was the quantum well,[1-4] which consists of a very thin layer (~10nm thick) of semiconducting material, sandwiched between much thicker insulating regions (see Fig. 1.1a). When the semiconductor layer absorbs a photon and promotes an electron from the valence band into the conduction band, an electron-hole pair is formed. In the direction perpendicular to this layer, the z direction, the carriers (electrons and holes) reside in a potential well, as seen in Fig. 1.1b. When the thickness of the layer is comparable to the characteristic lengths of the electron and hole, the carrier wavefunctions are quantized in the z direction. In the other two directions the carriers are not constrained. Therefore, quantum wells are often referred to as two-dimensional materials.

A quantum dot, illustrated in Fig. 1.2, is the zero-dimensional analog of the quantum well. In other words, a quantum dot is a nanometer-scale semiconductor crystallite which confines the electron-hole pair in all three dimensions. For cadmium selenide (CdSe), the semiconductor which I investigate in this thesis, the characteristic length scale of the electron-hole pair is ~112Å (twice the exciton Bohr radius). Therefore, if the size of the crystallite is comparable to this length, the electron and hole are "quantum confined" by the crystallite boundary. Although shown as a cube in Fig. 1.2, our dots are roughly spherical in shape. The largest CdSe quantum dots which are discussed here (~105Å diameter) have tens of thousands of atoms per crystallite. The smallest dots (~24Å diameter) have hundreds of atoms per crystallite.

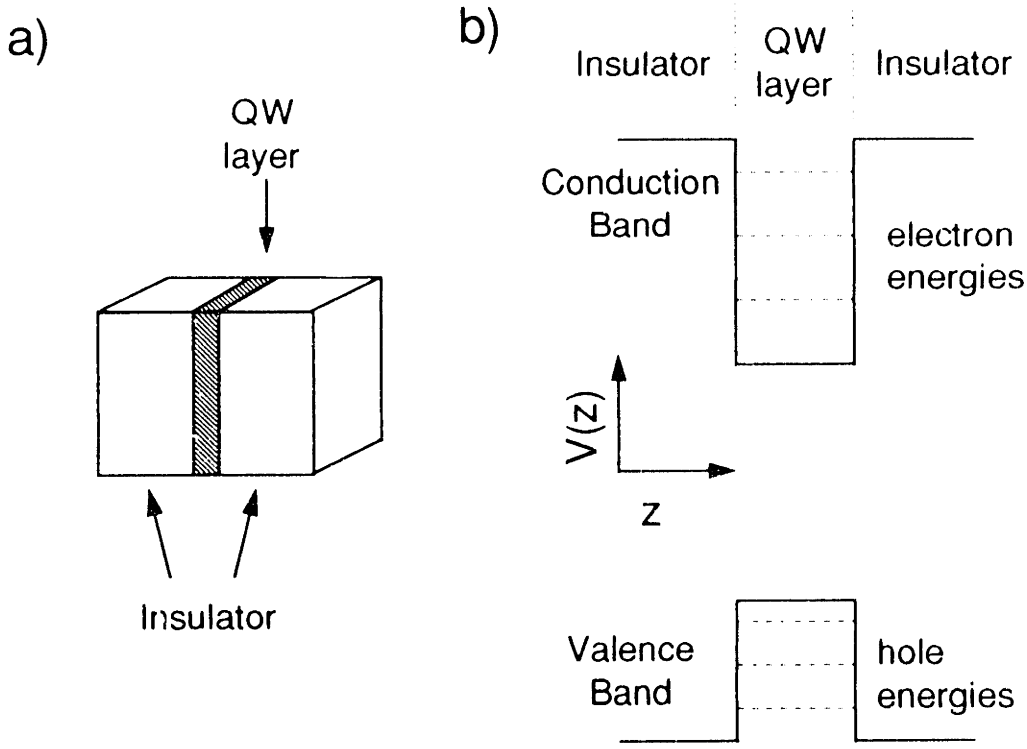

FIG. 1.1 (a) Quantum well (QW) structure. A thin semiconductor layer is grown between thicker insulating regions. (b) Potential well formed in the conduction and valence bands in the z-direction. The electron and hole energies are quantized due to the finite size of the semiconductor layer.

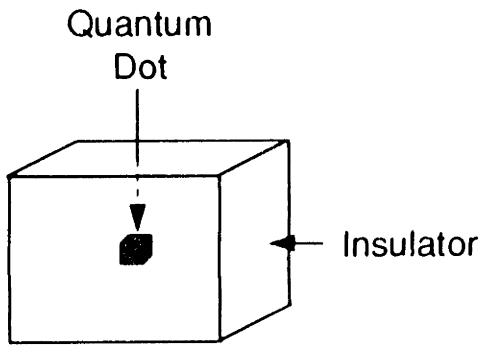

FIG. 1.2 Quantum dot structure. A nm-scale semiconductor crystallite is embedded inside an insulating material. The potential well in Fig. 1.1b now applies to all three directions (x,y, and z).

1.2 Motivation: Why Study Quantum Dots?

Quantum dots provide an opportunity to investigate semiconductor behavior in the finite size regime. Due to quantum confinement these materials have many fundamentally interesting and potentially useful optical properties. We study quantum dots both to understand their basic photophysics and to probe the new and perhaps unexpected physical phenomenon which occur in the quantum size regime. A central question, both in terms of the fundamental physics and potential applications, is how the semiconductor optical spectrum evolves with size. While in bulk semiconductors (at 300K) the absorption spectrum is a featureless continuum above the band gap of the material, in quantum dots the spectrum is highly structured. This structure arises due to the confinement of the electron-hole pair by the dot boundary. In principle, bulk oscillator strength is concentrated in a series of discrete atomic-like transitions For this reason, quantum dots are sometimes called "artificial atoms". However, while this atomic-like behavior would be incredibly useful in semiconductor optical devices, such as the "optical switch",[4] in practice this behavior has not been fully realized. A question which we attempt to address is whether the inability to fully attain the atomic-like behavior is inherent to the physics of quantum dots or due to imperfections in the sample distribution, such as size, shape, or structural variations, which inhomogeneously broaden spectral features.

However, even without the perfect atomic-like behavior predicted by early theories,[5] the uses of quantum dots are being heavily explored due to their unique properties. As semiconductor materials, quantum dots have high damage thresholds and may be useful as robust "chromophores". Since their transition energies are continuously tunable with dot diameter, these "chromophores" can be tailored for a particular application. In addition, the dots have high quantum yield in photoluminescence and electroluminescence has recently been demonstrated.[6,7] Due to their versatile surface chemistry, they can be dispersed in a variety of host materials, such as solvents, polymers, and even other semiconductors.[8] Recently, even ordered arrays of quantum dots (quantum dot solids) have been fabricated, presenting a whole new class of quantum dot materials.[9] In order to

fully utilize these unique properties in potential applications, a basic understanding of quantum dot photophysics is required.

1.3 Quantum Dot Theory: The Basics

1.3.1 "Particle-in-a-Sphere"

Much of the basic physics in quantum dot spectroscopy can be explained by the simple "particle-in-a-sphere" model.[10,11] This model considers a particle of mass m_o inside a spherical potential well of radius a,

$$V(r) = \begin{cases} 0 & r < a \\ \infty & r > a \end{cases} \tag{1.1}$$

Following Flügge,[12] the Schrödinger equation is solved yielding wavefunctions

$$\Phi(r,\theta,\phi) = C \frac{j_\ell(k_{n,\ell}\, r)\; Y_\ell^m(\theta,\phi)}{r} \tag{1.2}$$

where C is a normalization constant, $Y_\ell^m(\theta,\phi)$ is a spherical harmonic, $j_\ell(k_{n,\ell}\, r)$ is the ℓ^{th} order spherical Bessel function, and

$$k_{n,\ell} = \frac{\alpha_{n,\ell}}{a} \tag{1.3}$$

with $\alpha_{n,\ell}$ the n^{th} zero of j_ℓ. The energy of the particle is given by

$$E_{n,\ell} = \frac{\hbar^2 k_{n,\ell}^2}{2\, m_o} = \frac{\hbar^2 \alpha_{n,\ell}^2}{2\, m_o\, a^2} \tag{1.4}$$

Due to the symmetry of the problem the eigenfunctions (Eq. 1.2) are simple atomic-like orbitals which can be labeled by the quantum numbers n (*1*, *2*, *3*. . .), ℓ (*s*, *p*, *d*. . .), and m. The energies (1.4) are identical to the kinetic energy of the free particle, except that the wavevector, $k_{n,\ell}$, is quantized by the spherical boundary condition. Note also that the energy is proportional to $1/a^2$ and therefore is strongly dependent on the size of the sphere.

At first glance, this model may not seem useful for the quantum dot problem. After all, the particle above is confined to an empty sphere, while the quantum dot is filled with semiconductor atoms! However, by a series of approximations the quantum dot problem can be reduced to the "particle-in-a-sphere" form (Eq. 1.1).

First, the bulk conduction and valence bands are approximated by simple isotropic bands within the *effective mass approximation*. According to Bloch's theorem, the bulk wavefunctions can be written as

$$\Psi_{nk}(\vec{r}) = u_{nk}(\vec{r}) \exp(i\vec{k}\cdot\vec{r}) \qquad (1.5),$$

where u_{nk} is a function with the periodicity of the crystal lattice and the wavefunctions are labeled by the band index n and wavevector k. The energy of these wavefunctions are typically described in a "band diagram", a plot of E vs. k. Although band diagrams are in general quite complex and difficult to calculate, in the effective mass approximation the bands are assumed to have simple parabolic forms near extrema in the band diagram. For example, since CdSe is a direct gap semiconductor, both the valence band maximum and conduction band minimum occur at k=0 (see Fig. 1.3). In the effective mass approximation, the energy of both the conduction (n=c) and valence (n=v) bands are approximated as

$$\begin{aligned} E_k^c &= \frac{\hbar^2 k^2}{2\, m_{eff}^c} + E_g \\ E_k^v &= -\frac{\hbar^2 k^2}{2\, m_{eff}^v} \end{aligned} \qquad (1.6),$$

where E_g is the semiconductor bandgap and the energies are relative to the top of the valence band. In this approximation the carriers behave as free particles with an "effective mass", $m_{eff}^{c,v}$. Graphically, the effective mass accounts for the curvature of the conduction and valence bands at k=0. Physically, the effective mass incorporates the complicated periodic potential felt by the carrier in the lattice. This approximation allows us to completely ignore the semiconductor atoms in the lattice and treat the electron and hole as free particles.

If the effective mass approximation can be combined with a spherical boundary condition then the quantum dot problem is in the "particle-in-a-sphere" from (Eq. 1.1). However, in this case the quantum dot is treated as a "bulk" sample. In other words, we assume that the single particle (electron or hole) wavefunction can be written in terms of

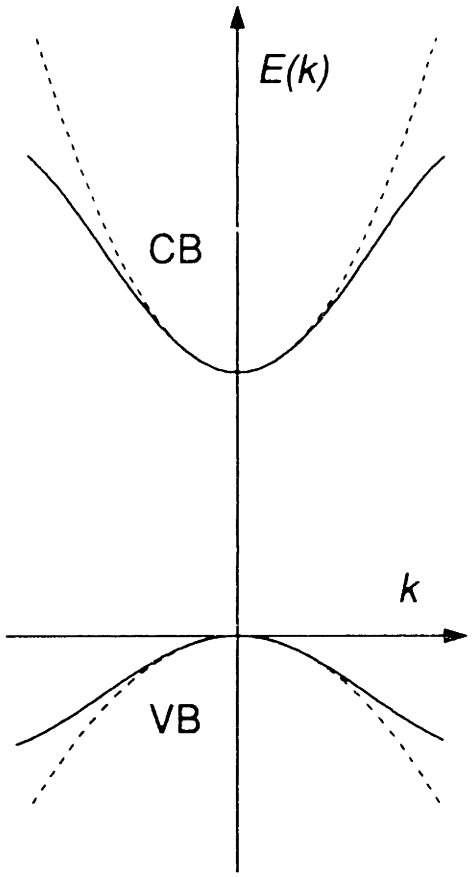

FIG. 1.3 Simple two band model for bulk semiconductors. The real band structure (solid lines) is approximated by parabolic bands (dashed lines) at k=0 in the effective mass approximation. The curvature of the bands reflects the "mass" of the electrons in the conduction band (CB) and the holes in the valence band (VB).

Bloch functions (Eq. 1.5). This approximation, sometimes called the *envelope function approximation*, is valid when the dot diameter is much larger than the lattice constant of the material. To satisfy the boundary condition the single particle (sp) wavefunction is then written as a linear combination of Bloch functions

$$\Psi_{sp}(\vec{r}) = \sum_{k} C_{nk}\ u_{nk}(\vec{r})\ \exp(i\,\vec{k}\cdot\vec{r}) \qquad (1.7),$$

with expansion coefficients, C_{nk}. If we assume that the functions u_{nk} have a weak k dependence then Eq. 1.7 can be rewritten as

$$\Psi_{sp}(\vec{r}) = u_{n0}(\vec{r}) \sum_{k} C_{nk} \exp(i\,\vec{k}\cdot\vec{r}) = u_{n0}(\vec{r})\, f_{sp}(\vec{r}) \qquad (1.8),$$

where $f_{sp}(\vec{r})$ is the single particle "envelope function". In the tight-binding approximation [or linear combination of atomic orbitals (LCAO) approximation] the periodic function u_{n0} is written as a sum of atomic wavefunctions, φ_n,

$$u_{n0}(\vec{r}) \approx \sum_i C_{ni}\ \varphi_n(\vec{r} - \vec{r}_i) \qquad (1.9),$$

where the sum is over lattice sites and n represents the conduction band or valence band for the electron or hole, respectively. Therefore, the functions u_{n0} can be determined and the quantum dot problem is reduced to determining the envelope functions for the single particle wavefunctions, $f_{n\mu}$. However, in spherically-shaped dots with an infinitely high potential barrier at the dot boundary, the envelope functions are given by the particle-in-a-sphere solutions, Eq. 1.2. Each carrier is treated as a "free particle" with mass m_{eff} subject to a constant potential inside a sphere of radius a. The energy of each particle is then described by Eq. 1.4 with the free particle mass m_o replaced by $m_{eff}^{c,v}$.

However, this treatment completely ignores the Coulombic attraction between the electron and the positively charged hole. In the bulk material this interaction can create bound hydrogenic-like states, or excitons. This effect should also be present in quantum dots.[13] To justify the neglect of this term, a third approximation is used, the *strong confinement approximation*.[1] Since the confinement energy of each carrier scales as $1/a^2$ (see Eq. 1.4), while the Coulomb interaction scales as $1/a$, in sufficiently small dots the quadratic confinement term dominates. This condition is satisfied when the size of the quantum dot is much smaller than the size of the bulk exciton. In this size regime, referred to as the strong confinement regime,[1] the electron and hole are treated independently and each is described as a "particle-in-a-sphere". The Coulomb term may then be added as a first order energy correction, E_C. Therefore, using Eqns. 1.4 and 1.8 the electron-hole pair (ehp) states are written as

$$\begin{aligned}\Psi_{ehp}(\vec{r}_e,\vec{r}_h) &= \Psi_e(\vec{r}_e)\,\Psi_h(\vec{r}_h) = u_c\ f_e(\vec{r}_e)\ u_v\ f_h(\vec{r}_h) \\ &= C\left[u_c\ \frac{j_{L_e}(k_{n_e,L_e} r_e)\ Y_{L_e}^{m_e}}{r_e}\right]\left[u_v\ \frac{j_{L_h}(k_{n_h,L_h} r_h)\ Y_{L_h}^{m_h}}{r_h}\right] \qquad (1.10),\end{aligned}$$

with energies

$$E_{ehp}(n_h L_h n_e L_e) = E_g + \frac{\hbar^2}{2a^2}\left\{\frac{\varphi^2_{n_h,L_h}}{m_{eff}^v} + \frac{\varphi^2_{n_e,L_e}}{m_{eff}^c}\right\} - E_c \qquad (1.11).$$

The states are labeled by the quantum numbers $n_hL_hn_eL_e$. For example, the lowest pair state is written as $1S_h1S_e$. For pair states with the electron in the $1S_e$ level, the first order Coulomb correction, E_c, is $1.8e^2/\varepsilon a$, where ε is the dielectric constant of the semiconductor. Equations 1.10 and 1.11 are usually referred to as the "particle-in-a-sphere" solutions to the quantum dot spectrum.

1.3.2 Optical Transition Probabilities

For a particular quantum dot pair state the transition probability is given by the dipole matrix element

$$P = \left| \left\langle \Psi_{ehp} \left| \vec{e} \cdot \hat{p} \right| 0 \right\rangle \right|^2 \qquad (1.12),$$

where $|0\rangle$ is the vacuum state and $\vec{e}$ is the polarization vector of the light. In the strong confinement approximation, Eq. 1.12 is commonly rewritten in terms of the single particle states

$$P = \left| \left\langle \Psi_e \left| \vec{e} \cdot \hat{p} \right| \Psi_h \right\rangle \right|^2 \qquad (1.13).$$

Since the momentum operator, $\hat{p}$, acts only on the unit cell portion of the wavefunction and the envelope functions do not change significantly over this length scale, Eq. 1.13 is simplified to

$$P = \left| \left\langle u_c \left| \vec{e} \cdot \hat{p} \right| u_v \right\rangle \right|^2 \left| \left\langle f_e \middle| f_h \right\rangle \right|^2 \qquad (1.14).$$

In the "particle-in-a-sphere" model this yields

$$P = \left| \left\langle u_c \left| \vec{e} \cdot \hat{p} \right| u_v \right\rangle \right|^2 \delta_{n_e,n_h} \delta_{L_e,L_h} \qquad (1.15),$$

due to the orthonormality of the "particle-in-a-sphere" envelope functions. Therefore, simple selection rules (Δn=0 and ΔL=0) are obtained.

1.4 The Bulk Band Diagram

1.4.1 The Real Band Structure

In the "particle-in-a-sphere" model the bulk conduction and valence bands are approximated by simple parabolic bands (Fig. 1.3). However, in general the band

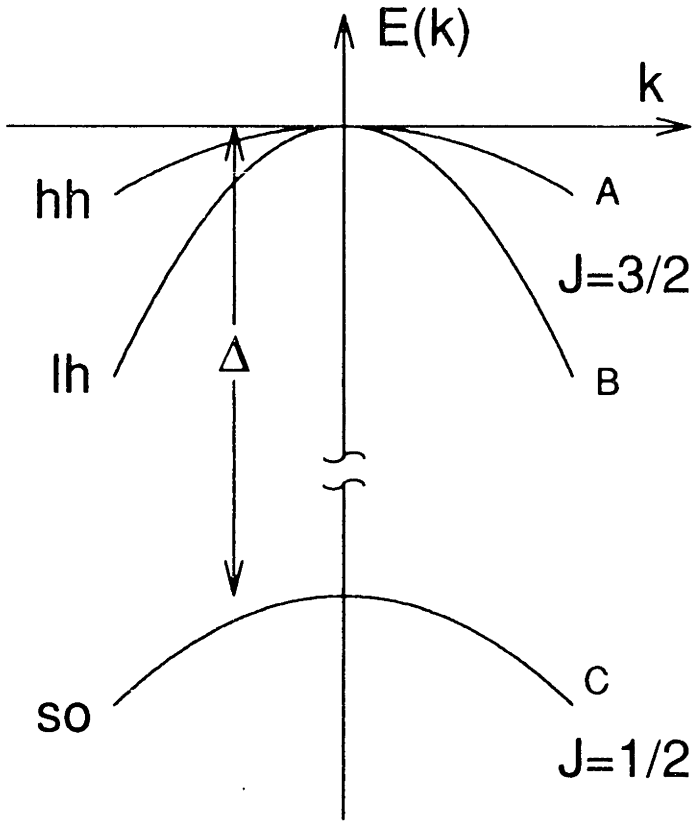

FIG. 1.4 Illustration of valence band structure at k=0 for diamond-like semiconductors. Due to spin-orbit coupling (Δ) the valence band is split into two bands (J=3/2 and J=1/2) at k=0. Away from k=0, the J=3/2 band is further split into the J_m=±3/2 heavy-hole (hh or A) and the J_m=±1/2 light-hole (lh or B) sub-bands. The J=1/2 band is referred to as the split-off (so or C) band.

structure of II-VI semiconductors, such as CdSe, is more complicated. While the conduction band is well approximated by the simple treatment in Fig. 1.3, the valence band is not. The valence band arises from Se 4p atomic orbitals and is 6-fold degenerate at k=0, including spin. (In contrast, the conduction band arises from Cd 5s orbitals and is only 2-fold degenerate at k=0). When this degeneracy is lifted, valence band sub-structure results. For quantum dot pair states, this structure strongly modifies the results of the "particle-in-a-sphere" model.[14]

For convenience CdSe is often approximated as having the diamond-like band structure, shown in Fig. 1.4. Due to strong spin-orbit coupling (Δ=0.42 eV in CdSe) the valence band degeneracy at k=0 is split into $p_{3/2}$ and $p_{1/2}$ sub-bands, where the subscript

refers to $J=l+s$ ($l=1$, $s=1/2$). Away from $k=0$ the $p_{3/2}$ band is further split into $J_m=\pm 3/2$ and $J_m=\pm 1/2$ sub-bands. The three sub-bands are referred to as either the heavy-hole, light-hole, and split-off-hole sub-bands, or the A, B, and C sub-bands, as depicted in Fig. 1.4.

For CdSe the structure shown in Fig. 1.4 is an approximation for two reasons. First, since the diamond unit cell consists of two identical carbon atoms, diamond has inversion symmetry. Therefore, according to Kramer's theorem all levels must be at least two-fold degenerate. In CdSe, where the unit cell consists of two different atoms, the inversion symmetry is absent. In detailed calculations this lack of inversion symmetry leads to linear terms in k which further split the A, B, and C sub-bands in Fig. 1.4 away from $k=0$. However, since these linear terms are small, they are generally neglected.

Second and more importantly, the band structure in Fig. 1.4 ignores the crystal field splitting which occurs in CdSe crystals with a wurtzite (or hexagonal) lattice. This lattice, with its unique "c" axis, has a crystal field which lifts the degeneracy of the A and B bands

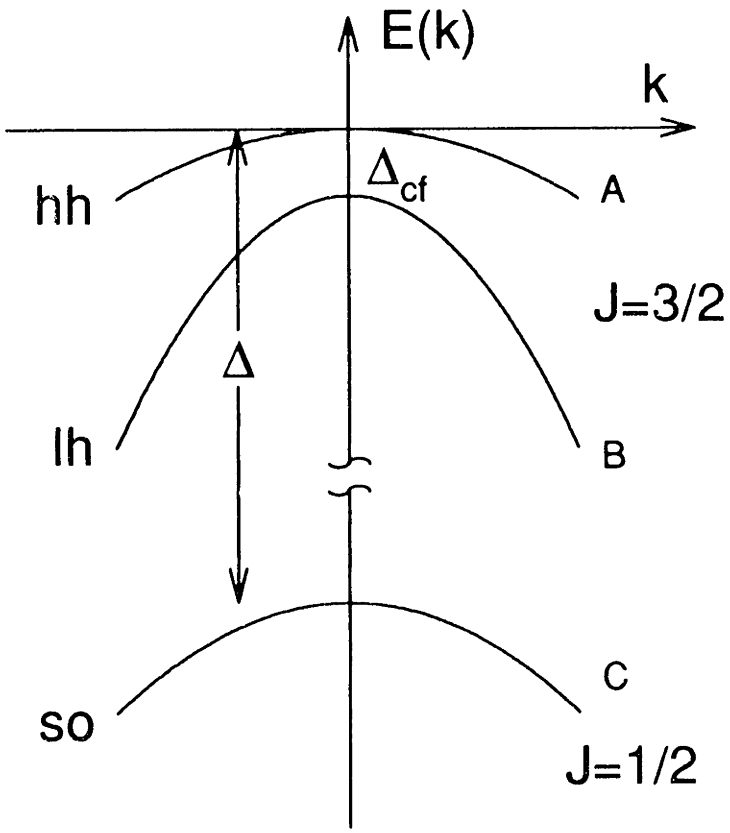

FIG. 1.5 Illustration of the bulk valence band for wurtzite (hexagonal) CdSe near $k=0$. Due to the crystal field of the hexagonal lattice the A and B bands are split by Δ_{cf} (25meV) at $k=0$.

at k=0 as shown in Fig. 1.5. This splitting, also referred to as the "A-B splitting", is small (25meV) in bulk CdSe and is often neglected in quantum dot calculations. However, in chapters 4-6 we show that this term can cause additional splittings to occur in the quantum dot transitions.[15]

1.4.2 The $k \cdot p$ Method (pronounced k-dot-p)

For quantum dot calculations it is important to have an accurate picture of the bulk bands. Although bulk band structure can be determined with high accuracy using a variety of computational methods, these methods rarely provide analytical expressions for the description of the bands. For this purpose a much simpler, but often sufficient approach, the $k \cdot p$ method, is used. In this method the bulk bands are expanded analytically around a particular point in k-space, typically k=0. Around k=0 the band energies and wavefunctions are then expressed in terms of the periodic functions u_{n0} and their energies E_{n0}.

To derive general expressions for u_{nk} and E_{nk} within this approach one considers the Bloch functions in Eq. 1.5. These functions are solutions of the Schrödinger equation for the single particle Hamiltonian

$$H_0 = \frac{p^2}{2m_o} + V(x) \qquad (1.16),$$

where $V(x)$ is the periodic potential of the crystal lattice. Using Eqs. 1.5 and 1.16 it is simple to show that the periodic functions, u_{nk}, satisfy the equation

$$\left[H_0 + \frac{1}{m_o}(k \cdot p) \right] u_{nk} = \lambda_{nk}\, u_{nk} \qquad (1.17),$$

where

$$\lambda_{nk} = E_{nk} - \frac{k^2}{2\, m_o} \qquad (1.18).$$

Since u_{n0} and E_{n0} are assumed known, Eq 1.17 can be treated in perturbation theory around k=0 with

$$H' = \frac{(k \cdot p)}{m_o} \qquad (1.19).$$

Then using non-degenerate perturbation theory to second order we obtain the energies

$$E_{nk} = E_{n0} + \frac{k^2}{2m_o} + \frac{1}{m_o^2} \sum_{m \neq n} \frac{\left| \vec{k} \cdot \vec{p}_{nm} \right|^2}{E_{n0} - E_{m0}} \qquad (1.20),$$

and functions

$$u_{nk} = u_{n0} + \frac{1}{m_o} \sum_{m \neq n} u_{m0} \frac{\vec{k} \cdot \vec{p}_{mn}}{E_{n0} - E_{m0}} \qquad (1.21),$$

with

$$\vec{p}_{nm} = \langle u_{n0} | \vec{p} | u_{m0} \rangle \qquad (1.22).$$

The summations in Eqs 1.20 and 1.21 are over all bands $m \neq n$. As one might expect the dispersion of band n is due to coupling with nearby bands. Terms linear in k are absent in Eq. 1.20 since we assume that parity is conserved. Actually, in CdSe parity is not strictly conserved and small linear terms appear. However, here, as in subsection 1.4.1, these terms are considered small and neglected. In addition, for the CdSe valence band, degenerate perturbation theory must be used. In this case the valence band must be diagonalized before coupling with other bands is considered.

In the above treatment we have neglected spin-orbit coupling terms. However, these terms are easily added as can be seen in Kittel.

1.4.3 The Kane Model

In some cases it is necessary to go beyond second order in the $k \cdot p$ approach to properly describe the bands. However, in higher orders this approach is often cumbersome and Kane[16] developed an alternate procedure which is more widely used. In the Kane model a small subset of bands are treated exactly by explicitly diagonalizing Eq. 1.17 (or the equivalent expression with spin-orbit included). This subset usually contains the bands of interest — e.g. the valence band and conduction band. Then the influence of outlying bands are included within the second order $k \cdot p$ approach. Due to the exact treatment, the dispersion of each band is no longer strictly quadratic as in Eq. 1.20. Therefore, the Kane Model better describes band "nonparabolicities".

1.4.4 The Luttinger Hamiltonian

For bulk diamond-like semiconductors the 6-fold degenerate valence band is described by the Luttinger Hamiltonian.[17,18] This expression, a 6x6 matrix, is derived within the context of degenerate $k \cdot p$ perturbation theory. The Hamiltonian is commonly simplified further using the spherical approximation.[19,20] In this case only terms of spherical symmetry in the Luttinger Hamiltonian are considered. Cubic "warping" terms are neglected and if desired, treated as a perturbation. For quantum dot theories which include the valence band degeneracies, the Luttinger Hamiltonian is the initial starting point to obtain the hole eigenstates and energies. We note that since CdSe is wurtzite, as discussed in 1.4.1 above, use of the Luttinger Hamiltonian for CdSe quantum dots is an approximation. It does not include the crystal field splitting that is present in wurtzite CdSe.

1.5 The Surface Model

While exciton recombination in bulk II-VI semiconductors occurs with a ~1ns lifetime,[21] CdSe quantum dots exhibit a ~1μs radiative lifetime at 10K. This effect is perhaps not surprising in early samples which were of poor quality and exhibited only weak "deep trap" emission.* However, more recent samples which are of much higher quality and emit strongly at the band edge, also have long radiative lifetimes. To explain this behavior, quantum dot emission has been rationalized as a "surface effect".[22-26] The anomalous emission lifetime has been explained by localization of the photoexcited electron and/or hole at the dot/matrix interface. Once the carriers are localized in surface "traps", the decrease in carrier overlap increases the recombination time. The influence of the surface on quantum dot emission is reasonable since these materials have such large surface-to-volume ratios (e.g. in a ~30Å diameter dot ~1/3 of the atoms are on the surface). This "surface model" can explain the long radiative lifetimes, luminescence polarization results,[26] and even the unexpectedly high longitudinal optical (LO) phonon

---

* "Deep trap" is emission which is strongly red-shifted from the HOMO-LUMO transition (or "band edge" in solid state terminology) of the quantum dot. While the true origin of this luminescence is unknown, it is generally assumed that its presence indicates defect and/or impurity states which are deep in the gap.

coupling observed in emission. The validity of the surface model is addressed in chapter 4.

1.6 Thesis Overview

This thesis describes the size-dependence of the optical spectrum in CdSe quantum dots. We investigate a series of samples with sizes which span the strong confinement regime (see subsection 1.3.1). The results are divided in two sections.

In section II (chapters 2 and 3) one of the original and basic experimental questions about quantum dots — how their electronic spectra evolve in the strong confinement regime — is addressed. New synthetic techniques[27] are utilized to fabricate a series of high quality CdSe quantum dot samples with mean diameters ranging from ~24 to ~105Å. Preliminary results are presented in chapter 2 using transient differential absorption spectroscopy. These results are expanded in chapter 3 using photoluminescence excitation (PLE) spectroscopy. The size dependence of ten absorption features is presented and compared with quantum dot effective mass theories.[28] We find sufficient agreement to confidently assign six of the transitions and provide possible assignments for the remaining four. In addition our size dependent data exhibit two strong avoided crossings, demonstrating the importance of valence band structure (Fig. 1.4) in the description of the excited states. From these results a more accurate theoretical model for the description of the quantum dot spectrum is emerging.

While section II deals with the *exciton structure*, section III (chapters 4, 5, and 6) focuses on the lowest excited state (labeled $1S_h1S_e$ in subsection 1.3.1) and investigates the *exciton fine structure*. Each of the electron-hole pair states predicted by standard quantum dot effective mass theory[28] is highly degenerate. However, according to more recent theory[29] these degeneracies are lifted by the crystal field of the lattice (see subsection 1.4.1), the non-spherical shape of our dots, and the electron-hole exchange interaction. This exciton fine structure is particularly interesting because it predicts that the lowest excited state is optically forbidden. Relaxation of the excited quantum dot into this level, referred to as the "dark exciton", can explain the long radiative lifetimes observed in CdSe quantum dots, an effect previously attributed to surface traps (see

section 1.5). In chapter 4 the observation of absorption structure in the lowest excited state is confirmed. This structure is assigned to the predicted exciton fine structure. The observation of the "dark exciton" in emission is discussed in chapter 5. Finally in chapter 6, further evidence for these assignments is provided by the size dependence of the band edge absorption and emission features. The data is compared with the theoretically predicted structure and reasonable agreement is obtained.

1.7 Bibliography

M. Aven and J. S. Prener, *Physics and Chemistry of II-VI Compounds* (North Holland, Amsterdam, 1967), Chapter 1.

L. Bányai and S. W. Koch, *Semiconductor Quantum Dots* (World Scientific, Singapore, 1993).

G. Bastard, *Wave Mechanics Applied to Semiconductor Heterostructures* (Wiley, New York, 1988), Chapters 2 and 3.

G. L. Bir and G. E. Pikus, *Symmetry and Strain-Induced Effects in Semiconductors* (Wiley, New York, 1974).

E. O. Kane in *Narrow Band Semiconductors. Physics and Applications* edited by W. Zawadzki, *Lect. Notes Phys.*, Volume 133 (Springer Verlag, Berlin) 1980.

C. Kittel, *Quantum Theory of Solids* (Wiley, New York, 1987), Chapters 9 and 14.

M. Tinkham, *Group Theory and Quantum Mechanics* (McGraw-Hill, New York, 1964), Chapter 8.

1.8 References

1. H. Okamoto, Jap. J. of Appl. Phys. **26**, 315 (1987).
2. D. S. Chemla and D. A. B. Miller, J. Opt. Soc. Am. B **2**, 1155, (1985).
3. D. S. Chemla, Physics Today, June 1993, p. 46.
4. E. Garmire, Physics Today, May 1994, p. 42.
5. S. Schmitt-Rink, D. A. B. Miller, and D. S. Chemla, Phys. Rev. B **35**, 8113 (1987).
6. V. Colvin, M. Schlamp, and A. P. Alivisatos, Nature **370**, 354 (1994).
7. B. O. Dabbousi, M. G. Bawendi, O. Onitsuka, and M. F. Rubner, Appl. Phys. Lett. **66**, 1316 (1995).
8. M. Danek, Ph.D. Thesis, Massachusetts Institute of Technology, 1995.
9. C. B. Murray, Ph.D. Thesis, Massachusetts Institute of Technology, 1995.
10. Al. L. Efros and A. L. Efros, Fiz. Tekh. Poluprovodn. **16**, 1209 (1982) [Sov. Phys. Semicond. **16**, 772 (1982)].
11. L. E. Brus, J. Chem. Phys. **79**, 5566 (1983); L. E. Brus, J. Chem. Phys. **80**, 4403 (1984).
12. S. Flügge, *Practical Quantum Mechanics* (Springer, Berlin, 1971), Vol. 1, p. 155.
13. Y. Z. Hu, M. Lindberg, and S. W. Koch, Phys. Rev. B **42**, 1713 (1990).
14. J. B. Xia, Phys. Rev. B **40**, 8500 (1989).
15. Al. L. Efros, Phys. Rev. B **46**, 7448 (1992).
16. E. O. Kane, J. Chem. Phys. Solids **1**, 249 (1957).
17. J. M. Luttinger and W. Kohn, Phys. Rev. **97**, 869 (1955).

18. J. M. Luttinger, Phys. Rev. **102**, 1030 (1956).
19. N. O. Lipari and A. Baldereschi, Phys. Rev. Lett. **42**, 1660 (1970); A. Baldereschi and N. O. Lipari, Phys. Rev. B **8**, 2697 (1973).
20. B. L. Ge'lmont and M. I. D'yakonov, Fiz. Tekh. Poluprovodn. **5**, 2191 (1971) [Sov. Phys. Semicond. **5**, 1905 (1972)].
21. C. H. Henry and K. Nassau, Phys. Rev. B **1**, 1628 (1970).
22. M. O'Neil, J. Marohn, and G. McLendon, J. Phys. Chem. **94**, 4356 (1990).
23. A. Eychmüller, A. Hässelbarth, L. Katsikas, and H. Weller, Ber. Bunsenges. Phys. Chem. **95**, 79 (1991).
24. A. Hässelbarth, A. Eychmüller, and H. Weller, Chem. Phys. Lett. **203**, 271 (1993).
25. M. G. Bawendi, W. L. Wilson, L. Rothberg, P. J. Carroll, T. M. Jedju, M. L. Steigerwald, and L. E. Brus, Phys. Rev. Lett. **65**, 1623 (1990).
26. M. G. Bawendi, P. J. Carroll, W. L. Wilson, and L. E. Brus, J. Chem. Phys. **96**, 946 (1992).
27. C. B. Murray, D. J. Norris and M. G. Bawendi, J. Am. Chem. Soc. **115**, 8706 (1993).
28. A. I. Ekimov, F. Hache, M. C. Schanne-Klein, D. Ricard, C. Flytzanis, I. A. Kudryavtsev, T. V. Yazeva, A. V. Rodina, and Al. L. Efros, J. Opt. Soc. Am. B **10**, 100 (1993).
29. Al. L. Efros, M. Rosen, M. Kuno, M. Nirmal, D. J. Norris, and M. G. Bawendi, (in preparation).

Section II
The Exciton Spectrum

Chapter 2

Preliminary Measurement of the Exciton Spectrum*

2.1 Introduction

Nanometer size structures provide the opportunity to observe and control the properties of materials as they evolve from molecules to the bulk. In particular, semiconductor electronic transitions show interesting and strongly size dependent properties in this size regime. Nanometer size semiconductor crystallites (quantum dots) which are small compared to the bulk exciton Bohr radius exhibit three dimensional quantum confinement.[1,2] Quantum dots, often called "artificial atoms", possess in principle discrete electronic excitations with wavefunctions delocalized within and confined by the dot boundary. The collapse of the bulk oscillator strength into a small number of extended molecule-like transitions should lead to highly polarizable excited states and enhanced non-linear optical properties.[3] Numerous studies[1-13] have probed the lowest photoexcited state in II-VI dots. Its confinement induced shift to higher energy with decreasing diameter is well established.[1,2] However, experimental investigation of the size evolution of the higher excited states has been difficult. The discrete nature of these states is usually concealed by sample inhomogeneities such as distributions in size, shape and stoichiometry.

The observation and assignment of a series of excited states in CdSe quantum dots, the variation of their spacings with dot size, and the comparison of these spacings with recent theory are the main focus of this chapter. Our ability to observe a series of excited states depends crucially on a recently developed synthesis which provides II-VI quantum dots with a high degree of monodispersity (<4% rms in diameter), consistent crystal structure and surface derivatization, and control of size from ~15 to ~120Å in diameter.[14] Unlike

---

* Much of chapter 2 has appeared in print: D. J. Norris *et al.*, Phys. Rev. Lett. **72**, 2612 (1994).

most samples prepared in silicate glasses and previous samples in polymer films which typically emit from deep trap states with low quantum yield, our samples show "band edge" luminescence[1] with little deep trap emission and high quantum yield (>0.1 and measured as high as 0.9 at 10K). The high quality of our samples is demonstrated in Fig. 2.1a by the absorption spectra of a series of sizes from 19 to 115Å in diameter. As many as six transitions can be resolved in a single sample.

Despite the high quality of our samples, the main contribution to the width of the absorption features remains sample inhomogeneities. Nanosecond pump-probe or transient differential absorption (TDA) spectroscopy can further resolve the transitions.[5-8] With this technique we optically select a subset of the quantum dot size distribution by exciting each sample on the red edge of its first transition with a spectrally narrow pump beam. The pump-induced change in optical density (OD) contains both bleached and induced absorptions arising from particles already containing an electron-hole pair (Fig. 2.1b). Comparison of pump-probe spectra (Fig. 2.1b) with absorption data (Fig. 2.1a) shows that bleached features correspond to the position of ground state transitions, but are more clearly resolved. To independently verify this conclusion we use another size-selective technique, photoluminescence excitation (PLE). In general PLE reveals the positions of ground state absorptions by measuring luminescence intensity as a function of excitation energy (see also chapters 3 and 6). To measure only a subset of the size distribution, we monitor a narrow spectral band on the blue edge of the full luminescence while scanning the excitation wavelength.[6] Our quantum dot PLE results (Figs. 2.1c and 2.1d) clearly confirm that pump-probe bleaches lie at the positions of ground state transitions. PLE then provides a second independent measurement which can verify the pump-probe results.

2.2 Experimental

CdSe quantum dots were prepared according to the method of Ref. 14 and obtained as powders. Each sample was redissolved in toluene and sonnicated (15 min.) to ensure that the dots were well dispersed. To this solution, 75mg/ml poly(vinyl butyral) [or PVB]

[1] Luminescence which occurs at the HOMO-LUMO transition.

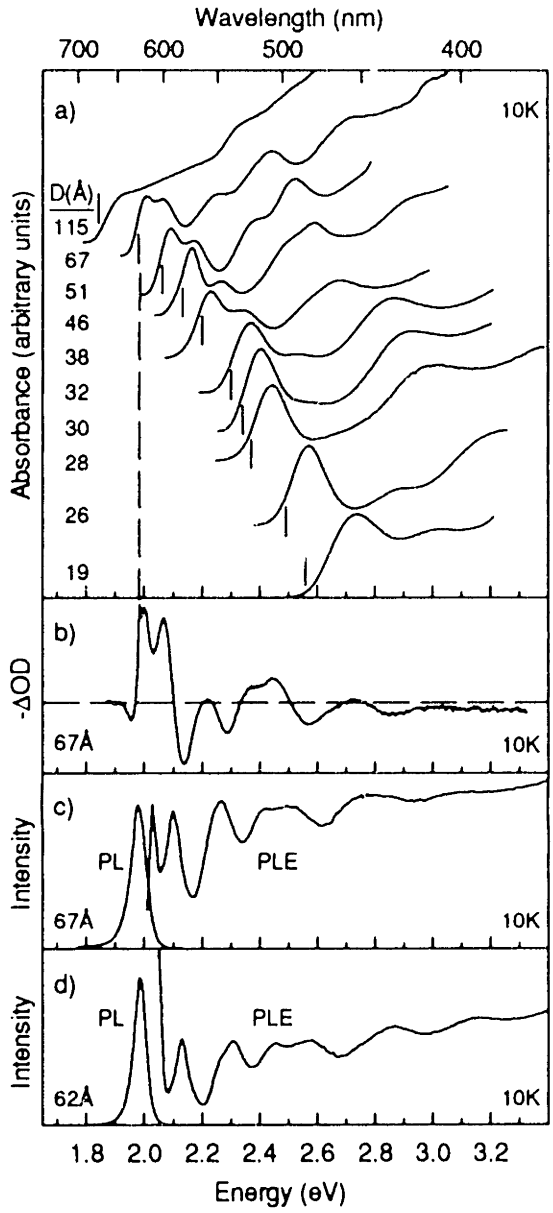

FIG. 2.1 (a) Absorption spectra for CdSe quantum dots embedded in optically clear poly(vinyl butyral) (PVB) films. Baselines are offset for clarity. Typical optical densities at the first absorption feature are 0.3-0.6. Mean diameters are measured by TEM. Black vertical lines mark pump frequencies in pump-probe experiments. (b) Bleach spectrum, plotted as negative change in optical density (-ΔOD), for 67Å dots. Positive (negative) peaks are bleaches (induced absorptions). The dashed horizontal line represents -ΔOD=0. (c) Photoluminescence (PL) and photoluminescence excitation (PLE) spectra for 67Å diameter dots (10K). Emission for PLE was observed at 2.016 eV with a ~1.5 meV bandpass. A small energy shift (utilized in Fig. 2.4) exists between the pump-probe and PLE spectra since the two techniques sample different portions of the size distribution. (d) PL and PLE spectra for ~62Å diameter dots (10K). Emission for PLE was observed at 2.022 eV with a ~0.7meV bandpass.

(Aldrich) was added, the mixture was again sonnicated (several hours), and a viscous polymer solution was obtained. Polymer films (~0.5mm thick) were then cast via evaporation, mounted between sapphire flats, and cooled to 10K in a continuous flow He cryostat (Janis Supertran). The PVB polymer films remained optically clear even at cryogenic temperatures.

The pump-probe apparatus is shown in Fig. 2.2 In a typical experiment a single 10 Hz *Q*-switched Nd:YAG laser (Continuum YG660-10) produced both the pump and probe beams (~7 ns pulses), separated by 12ns. A dye laser (Continuum TDL60), excited by the second harmonic (532nm) of the YAG, produced the spectrally narrow, tunable pump pulse. Pump intensity (<100 kW/cm^2) was carefully controlled to ensure linear absorption, checked via luminescence. To produce the spectrally broad probe pulse an ethanol/methanol solution of several laser dyes (typically Stilbene 420, Coumarin 480, Coumarin 540A, Rhodamine 590, and DCM from Exciton) was pumped through a "nozzle" (glass pipette) and the resulting dye stream was excited by the third harmonic (355nm) of the YAG. The broad spontaneous emission from the dye mixture was then focused onto the sample. The transmitted probe beam was refocused through an iris to reduce unwanted pump-induced luminescence, dispersed by a 0.25nm single grating (300g/mm) spectrometer (Aries FF250), and then detected by a 5ns-gated optical multichannel analyzer, or OMA (Princeton Instruments IRY-700G). Any residual pump-induced luminescence which reached the detector was corrected for by separately measuring the signal caused by the pump beam by itself and subtracting it from the pump-probe signal. For signal averaging, the experiment was driven by a personal computer (PC). The PC controlled two mechanical shutters (Vincent Associates VS14) to repetitively collect signals for all required permutations: background, pump only, probe only, pump and probe. To measure the lifetime of the pump-probe signal, a second *Q*-switched Nd:YAG laser (Continuum NY60-50), was used to produce delayed probe pulses. In this case both lasers and the detector were electronically synchronized via a digital pulse generator (Stanford Research Systems DG535).

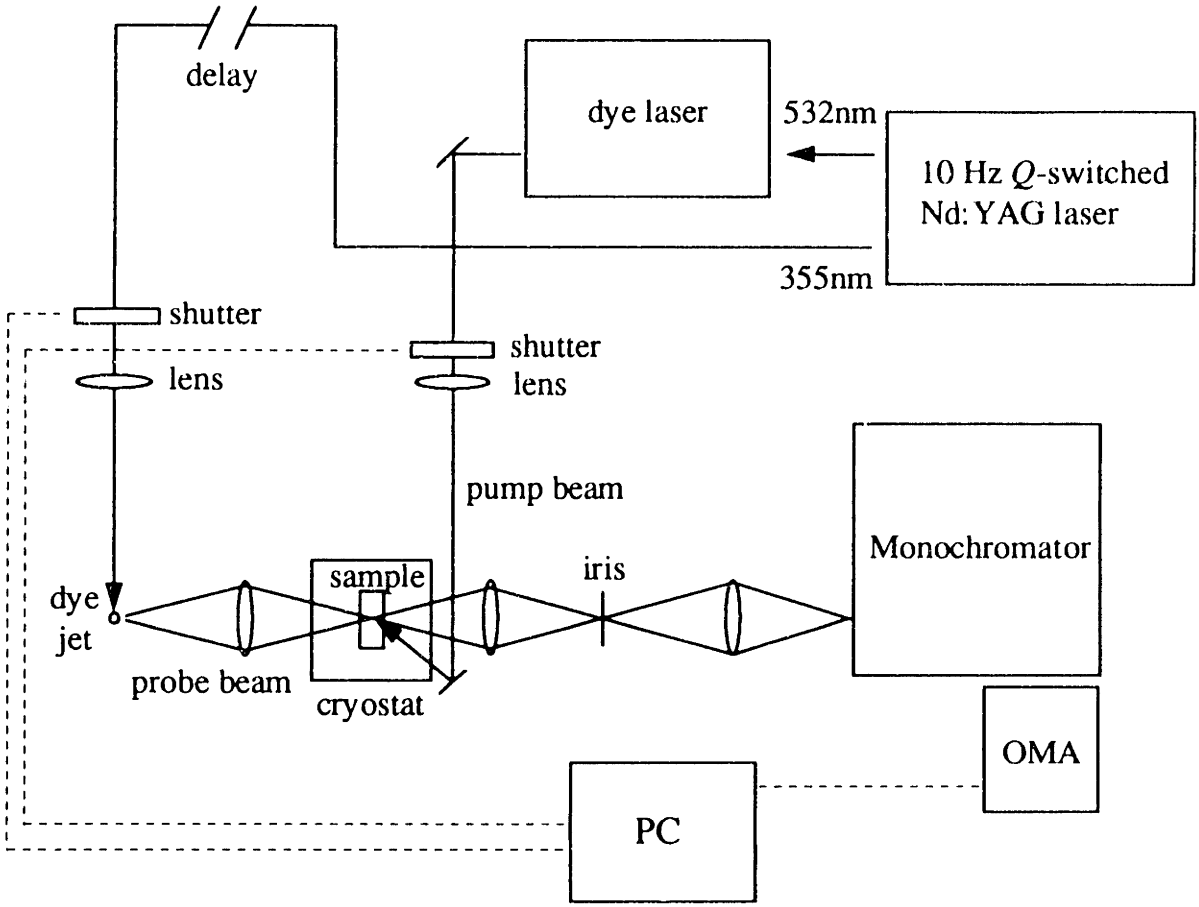

FIG. 2.2 Transient differential absorption (or pump-probe) apparatus. A single 10 Hz *Q*-switched Nd:YAG/dye laser system (~7ns pulses) produced both the pump and probe beams. The pump beam consists of the dye laser output. To produce a spectrally broad probe beam, the spontaneous emission from a dye jet, excited by the third harmonic (355nm) from the YAG, was focused onto the sample. The transmitted probe beam is dispersed by a 0.25nm monochromator (300g/mm) and detected by a 5ns-gated optical multichannel analyzer (OMA). The entire experiment is controlled via a personal computer (PC).

2.3 The Exciton Spectrum

Pump-probe spectra for our entire series of dots is shown in Fig. 2.3. This series spans the strong confinement regime in which electron-hole Coulomb interactions are much smaller than the confinement energy. This situation is addressed in early theoretical work by combining a simple two band isotropic effective mass model with a spherical boundary condition and treating the electron and hole separately.[1,2] The wavefunctions are described by "particle-in-a-sphere" envelope functions with electron and hole angular momenta L_e and L_h. However, this approach ignores the complexities of the CdSe valence band which is formed from Se p atomic orbitals. The sixfold degenerate (including spin) valence band is split by spin-orbit coupling into a band-edge fourfold degenerate J=3/2 band and a twofold degenerate J=1/2 band. For quantum dot hole levels arising from these bands the envelope function angular momentum, L_h, and the unit cell angular momentum, J, are not good quantum numbers. Only the total angular momentum, $F=L_h+J$, and parity are conserved. States with the same F and equal parity mix.[15-17] Therefore, each hole level with total momentum F, which is labeled as n_hL_F, is a mixture of L_h and L_h+2 envelope functions. The electron states, not affected by the valence band complications, are labeled as n_eL_e. [$n_{h(e)}$ are counters which number hole (electron) eigenstates for a given symmetry.] For example, the first excited state is written as $1S_{3/2}1S_e$, which contains contributions from the following hole states: (J=3/2, L_h=0, F=3/2), (J=3/2, L_h=2, F=3/2), and from the split off band (J=1/2, L_h=2, F=3/2). Within the strong confinement approximation, the Coulomb effect is added as a first order perturbation. In reality, especially for the larger dots, the Coulomb interaction further mixes these eigenstates and alters oscillator strengths.[18]

From Fig. 2.3 we extract the bleached absorption feature positions by fitting the spectra to a sum of positive- (bleaches) and negative-going (induced absorptions) Gaussians by standard nonlinear least squares methods.[19] Since some spectra were difficult to interpret due to overlap of bleaches with induced absorptions we assign only those features which we could follow through several sizes. Questionable peaks close to the zero crossing, such as the broad plateau at 0.7 eV for 32 and 30Å dots, were not

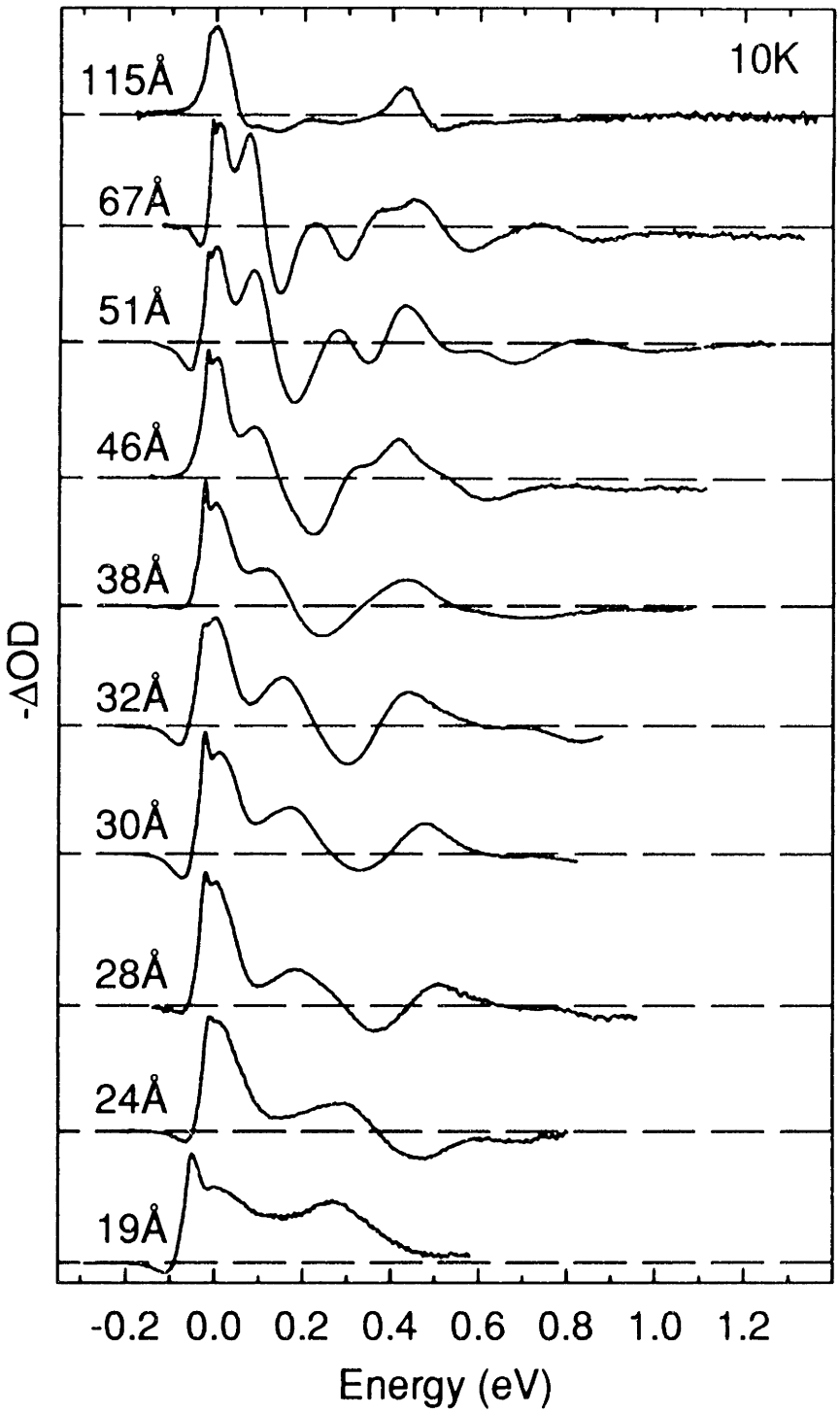

FIG. 2.3 Bleach spectra as in Fig. 2.1b with pump energies at 1.842, 1.984, 2.060, 2.130, 2.198, 2.296, 2.339, 2.366, 2.490, and 2.557 eV for 115 to 19Å dots. The lowest excited state ($1S_{3/2}1S_e$), typically bleached several percent, is set to zero energy in each spectrum.

included. When we compare our results with theory, we find that, as with simpler models, even the recent sophisticated effective mass theory of Ref. 17, which includes strong spin-orbit coupling, valence band degeneracies and the nonparabolicity of the conduction band, increasingly overestimates the confinement energy with decreasing size. This theory diverges in part due to its assumption of an infinite potential barrier at the dot boundary, but also due to the failure in general of effective mass theory for the smallest dots, which are better described in more molecular terms.[1,2,17,20] Most of the theoretical error originates in predicting the electron level due to the much lighter effective mass of the electron compared to that of the hole. Since the majority of the lowest allowed transitions contain the same electron level ($1S_e$), plotting transition energies relative to the first excited state ($1S_{3/2}1S_e$) minimizes the theoretical deviation in comparisons of theory with experimental results. Such a plot attempts to remove the common and problematic electron contribution.

Figure 2.4 (solid squares) shows our observed excited state energy spacings (relative to $1S_{3/2}1S_e$) as a function of the energy of the $1S_{3/2}1S_e$ state. We use this x-axis, instead of the more obvious dot diameter, since the energy of the $1S_{3/2}1S_e$ state is experimentally more precisely measured than dot size. Using size as the x-axis would introduce significant noise to the plot due to size measurement errors. In addition, the diameters measured and quoted in Fig. 2.1 are mean values which do not address the subset of the size distribution measured in the bleach results. Instead, we use the energy of the $1S_{3/2}1S_e$ state, which is easily and accurately determined and is a much better size dependent label for those dots that are actually probed.

The dashed lines in Fig. 2.4, visual guides for our assignments, trace the evolution of observed transitions with size. The solid lines are the prediction of Ref. 17. We do not plot theoretical curves for all allowed transitions, but rather those which best fit the experimental results. Our tentative assignments are based on the agreement between data and theory. According to the theoretical values from Ref. 17, we do not observe several transitions expected to be strongly allowed, e.g. $1P_{3/2}1P_e$. These transitions, as with other unobserved allowed transitions, poorly match the experimental points in Fig. 2.4, both in position and slope. However, the more detailed theoretical and experimental

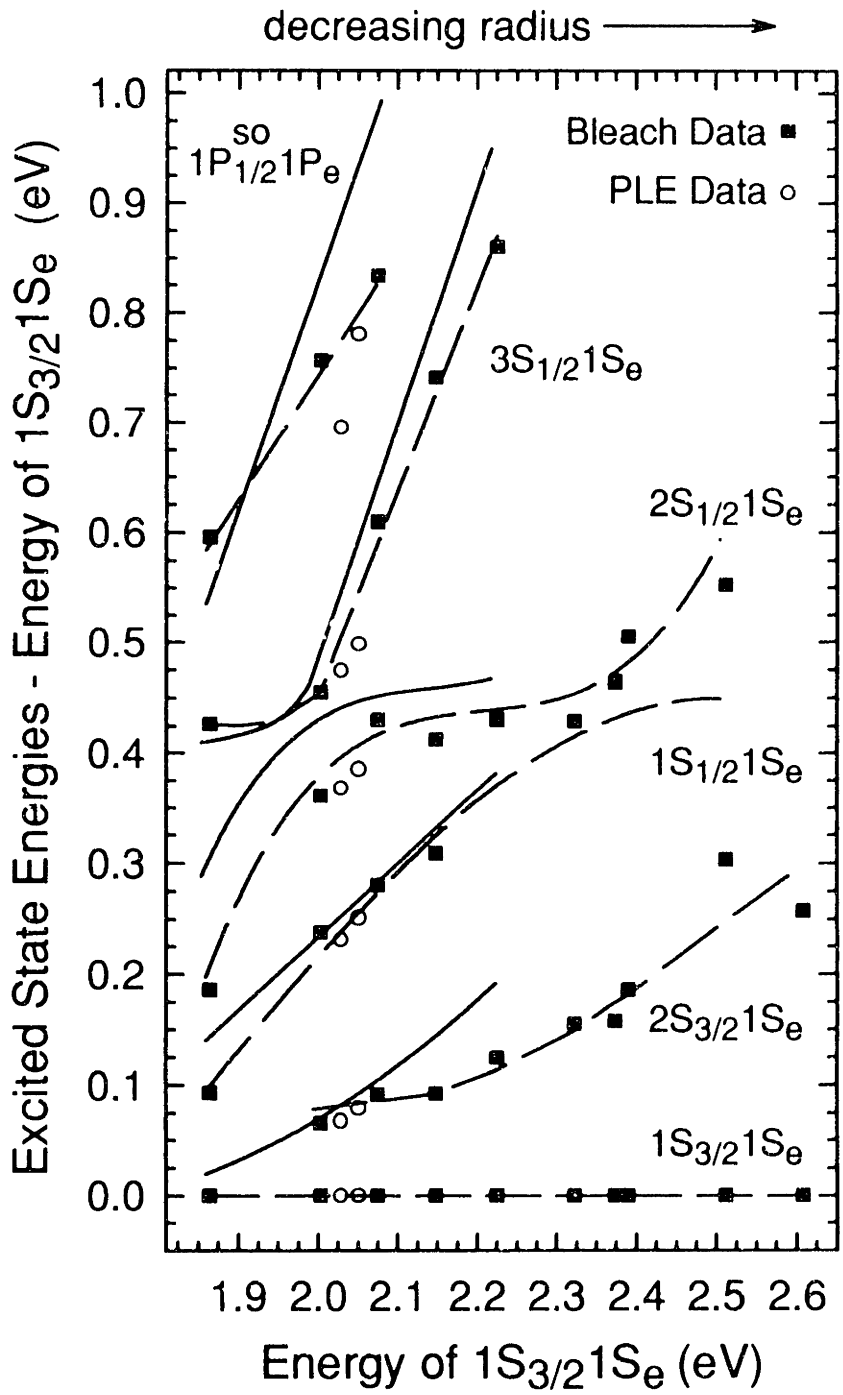

FIG. 2.4 Excited state spacings from Fig. 2.3 (solid squares). Transition energies are plotted relative to $1S_{3/2}1S_e$. The x-axis is the size dependent energy of $1S_{3/2}1S_e$. Dashed lines are visual guides for our assignments. Solid lines are predictions from Fig. 3 of Ref. 17. PLE data from Fig. 2.1c and Fig. 2.1d are plotted (open circles) to further support the observation of an avoided crossing. We note that the transition here attributed to $1S_{1/2}1S_e$ is properly assigned to $1P_{3/2}1P_e$, as discussed in chapter 3.

investigation in chapter 3 shows that the transition in Fig. 2.4 which is assigned to $1S_{1/2}1S_e$ is actually better described by $1P_{3/2}1P_e$. The true $1S_{1/2}1S_e$ transition is hidden in our pump-probe data by strong induced absorptions. In chapter 3 both $1P_{3/2}1P_e$ and $1S_{1/2}1S_e$ are clearly observed in PLE spectra.

We stress that simple effective mass theory cannot account for our data. A series of states split from $1S_{3/2}1S_e$ by spin-orbit coupling (0.42eV)[21] is seen in Fig. 2.4. These states, which evolve into the bulk spin-orbit band (C band), appear in zero'th order theory as a horizontal line due to the similar effective masses of the bulk A and C bands.[21] In reality this series of states is perturbed by nearby hole eigenstates with the same symmetry. We observe this situation in the bleach data as the avoided crossing of the $2S_{1/2}1S_e$ and $3S_{1/2}1S_e$ states for ~65Å dots. To independently confirm this claim we plot PLE data from Fig. 2.1 (c,d) at the crossing region in Fig. 2.4 (open circles).

The existence of an avoided crossing is intimately connected with the mixture of L_h and L_h+2 envelope functions in the hole eigenstates and, therefore, it is instructive to focus on the $2S_{1/2}1S_e$ state in Figs. 2.3 and 2.4 and follow the change in its L_h and L_h+2 components as a function of size. This state is a mixture of d-like (J=3/2, L_h=2, F=1/2) and s-like (J=1/2, L_h=0, F=1/2) hole levels only. All of the oscillator strength comes from the s-like component which couples strongly to the $1S_e$ electron level. In large dots, the $2S_{1/2}1S_e$ state has the hole mostly in the d-like J=3/2 level, and is a weak transition. After the avoided crossing with the $3S_{1/2}1S_e$ state, the hole state becomes mostly s-like from the J=1/2 band and gains oscillator strength. This variation in absorption strength is observed in Fig. 2.3 and provides additional evidence for our assignments. In small dots, the hole returns to weakly absorbing d-like character (J=3/2) after the avoided crossing with the $1S_{1/2}1S_e$ state.

It is surprising that the first excited state bleaches are so broad in our results. Pump-probe or PLE spectroscopies should considerably narrow the size distribution. The true homogeneous $1S_{3/2}1S_e$ linewidth, determined from previous pump-probe and fluorescence line narrowing experiments,[5,6,8,11] is significantly narrower (from 4 to 16meV, increasing with decreasing size).[11] We believe that the combination of a sharp bleach "spike" at the pump frequency and a broad bleach to the blue in each of our pump-probe spectra (Fig.

2.3) suggests an explanation. This structure is consistent with the existence of excitonic fine structure, predicted by theory. For example, our dots have a hexagonal (wurtzite) unit cell and are slightly prolate along the c-axis (aspect ratio of 1.0 to 1.3).[14] Both effects should cause four-fold degenerate hole states (F=3/2) to split,[22,23] analogous to the A-B band splitting observed in bulk wurtzite crystals. These effects, discussed in detail in chapters 4, 5 and 6, have important implications for quantum dot optical behavior.[24]

2.4 Proposed Bleach Mechanism

To help understand the origin of the TDA spectrum, Fig. 2.5 shows its dependence on the delay between the pump and probe pulses. The pump energy is chosen just below the first absorption line (Fig. 2.5a) so that the narrow and broad bleach features (the exciton fine structure in the first absorption feature) are clearly resolved. Both are present even with a 10μs delay (Fig. 2.5b). A plot of their integrated areas vs. time (inset to Fig. 2.5b) indicates that the decay of each feature can be divided into two components: an "early" (<500ns) component, where the bleach features decay on a 100ns timescale, and a longer μs component. At "long" times (>500ns) we extract a 4.4 μs time constant for each bleach using a biexponential least squares fit.

Since the band edge emission for this sample decays with a ~800ns time constant,[25] the 4.4μs bleach lifetime shown in Fig. 2.5 implies that at long times the bleach mechanism cannot be connected to populating the band edge emitting state. While "deep trap" states have much longer emission lifetimes, their quantum yield is much too small in this sample to explain the pump-probe decay. Therefore, we conclude that at long times the bleach is not caused by either band edge or "deep trap" emitting states. Rather long-lived "nonradiative" states must be responsible. (We define "nonradiative" states as those which either do not emit or emit further in the infrared.)

To explain the extremely long lifetime of the "nonradiative" states we assume that the electron and hole are separated in these states, perhaps localized at a defect or surface state. Previously, such carrier localization has been proposed as the origin of the pump-probe spectrum. The electric field produced by the separation of carriers induces a "Stark

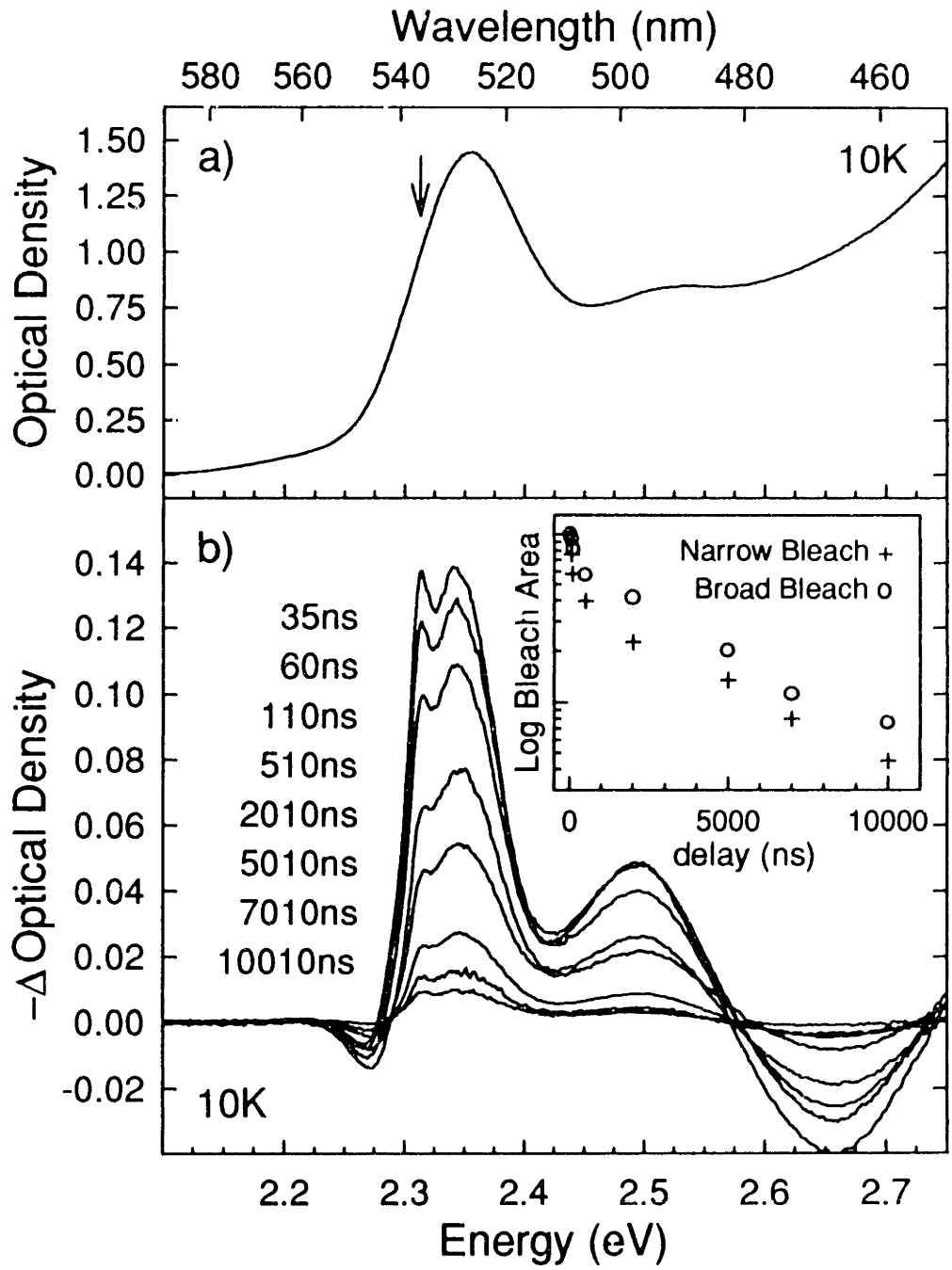

FIG. 2.5 (a) Absorption spectrum for ~35Å diameter CdSe quantum dots. The arrow marks the pump position used in b. (b) Pump-probe spectra as a function of the delay between pump and probe pulses. Both narrow and broad bleach features are resolved within the first absorption feature. These represent the band edge exciton structure discussed in chapters 4, 5, and 6. Inset: Log of the integrated area of the narrow and broad bleach features, obtained from a least squares fit, as a function of the pump-probe delay.

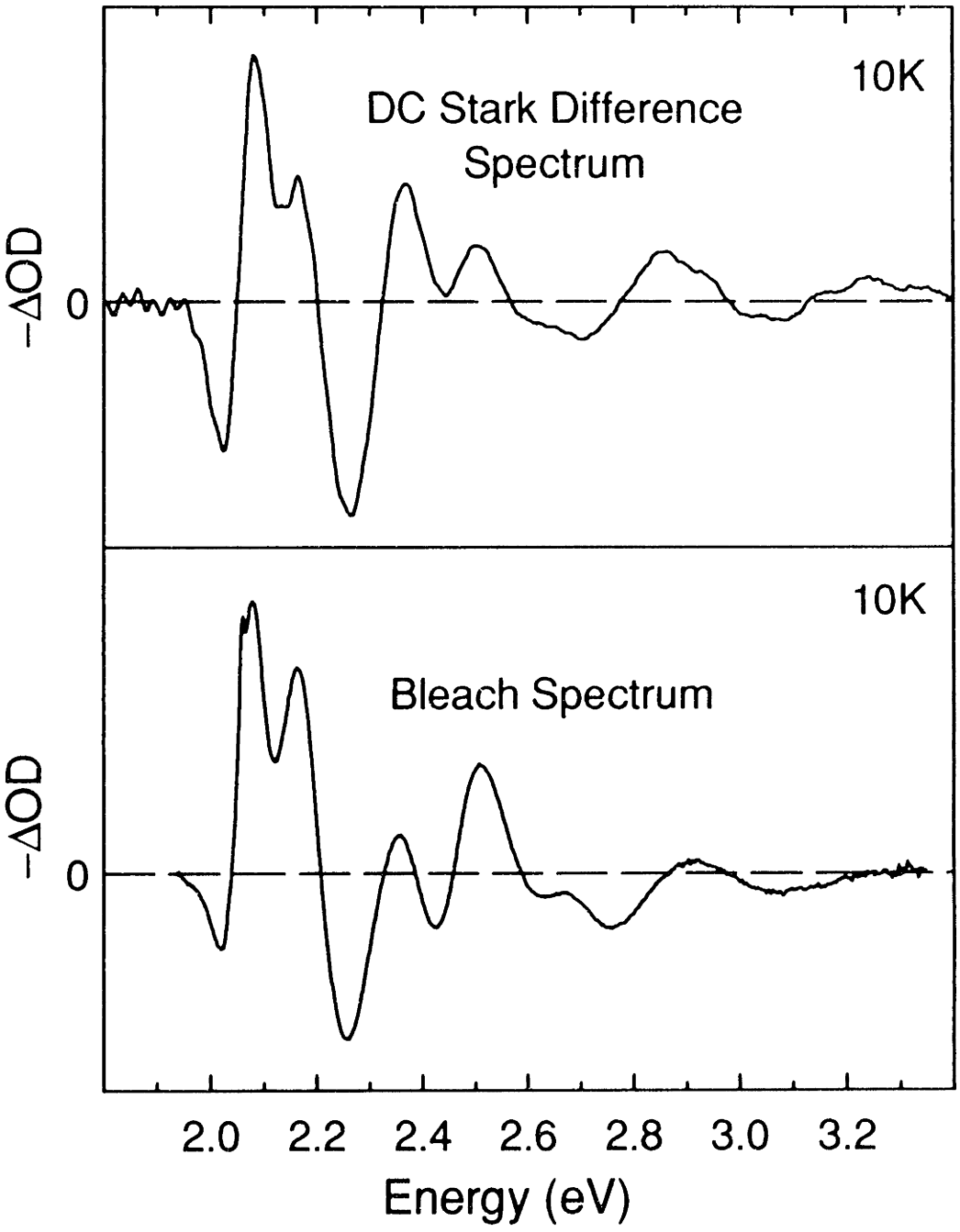

FIG. 2.6 dc Stark difference (field on-field off, ~$5x10^4$ V/cm internal field) and bleach spectra for ~51Å diameter CdSe quantum dots. With this field and pump power close to saturation the bleach signal is ~4x larger than the Stark signal for similar optical densities. For the pump-probe data, if we crudely model the dot as a delocalized electron with a "trapped", point source hole at the dot surface, we estimate that the electric field at the dot center is $2x10^5$ V/cm. This very roughly implies one fourth of the particles are excited, consistent with the experimental data given the large uncertainties of the estimation. (Stark data provided by A. Sacra)

effect" on the absorption of a second electron-hole pair.[9] The ability of the localized-carrier-induced Stark effect to explain our pump-probe results is supported by a comparison of dc Stark and pump-probe spectra, shown in Fig. 2.6. Stark difference spectra (field off minus field on) are nearly identical to pump-probe spectra obtained for the same sample.

In general a Stark field induces both a shift of state positions and a redistribution of oscillator strength. In the small field limit with well separated lineshapes the Stark difference spectrum is proportional to the first derivative of the absorption spectrum,

$$\Delta OD_{Stark}(\varepsilon) \propto E^2 f'(\varepsilon) \qquad (2.1),$$

where E is the electric field, f is the absorption lineshape, and ε is energy. This result can easily be shown by expressing the lineshape as a Taylor expansion in the Stark shift and calculating the perturbing Stark interaction to second order. However, in the small field limit with broad absorption linewidths, larger than both the field induced shift and the separation between interacting states, the Stark difference spectra is proportional to the second derivative of the absorption spectrum,

$$\Delta OD_{Stark}(\varepsilon) \propto E^2 \ f''(\varepsilon) \qquad (2.2).$$

This results from expressing the lineshape in a Taylor expansion in both the Stark shift and the spacing between interacting states. In the limit of broad linewidths, the second derivative lineshape implies that Stark bleaches appear at the positions of ground state transitions. The observable effect of the field is to bleach initially allowed transitions and cause induced absorptions due to a combination of shifting lines and initially forbidden transitions gaining oscillator strength. This limit is appropriate for our system in which the interacting levels are closely spaced relative to the linewidths (for example, a forbidden p-like hole state lies in between the first two observed transitions[17]) and this description agrees with experimental results. In Stark difference spectra for our dots, bleaches are observed at the positions of the absorption peaks,[26] as seen in previous studies.[27,28] These bleaches show no field dependent shift but increase quadratically in magnitude with the field. (A detailed treatment of these results, both theory and experiment, can be found in

Ref. 26.) Therefore, pump-probe bleaches in Fig. 2.3, which appear at the positions of ground state transitions are consistent with a trapped carrier induced Stark effect.

In addition to the Stark mechanism, at early times state filling may also contribute to the bleaching mechanism. When a particular state is occupied its absorption is decreased by the Pauli principle. Since most of the electron-hole pair states observed in absorption have the electron in the same level ($1S_e$) while the hole level changes ($1S_{3/2}$, $2S_{3/2}$, $1S_{1/2}$, etc.), the occupation of a single pair state (e.g. $1S_{3/2}1S_e$) can affect the absorption of many states via the electron level. Such state filling can bleach the absorption of a second electron-hole pair as long as the first electron level remains occupied. While we expect state filling of radiative states to contribute to the bleach mechanism at early times, we cannot determine the strength of this effect from our data.

In addition we cannot distinguish whether the "nonradiative" states responsible for the Stark bleach exist in every dot or if some dots in the distribution are radiative while others are "nonradiative", as has been suggested.[25,29] These issues are important since, if state filling contributes weakly to the bleach mechanism, the TDA signal would be due almost entirely to the "nonradiative states" (Stark mechanism). The existence of radiative and "nonradiative" subsets in the sample distribution could imply that the TDA results are unrelated to those dots which emit at the band edge. However, since our PLE spectra (Fig. 2.1), which arise from band edge emitting dots, show absorption structure similar to our TDA results, the absorption information obtained from TDA appears to be applicable to all dots. However, our data cannot resolve whether the same dots in the distribution yield both the TDA and luminescence results.

2.5 Conclusion

This chapter presents a measurement of the size dependence of a series of transitions in CdSe quantum dots. Good agreement with recent theoretical predictions allows us to assign the transitions. Our data show that the complexity of the valence band and the strong spin-orbit coupling in CdSe dominate the size dependence of excited state spacings. This is evident from the observation of an avoided crossing for ~65Å diameter quantum dots, observed in pump-probe spectra and confirmed by PLE. The strong similarity

between the full bleach spectrum and dc Stark data suggests that electric fields produced by carrier localization in "nonradiative" states induce a Stark effect in excited quantum dots. In our samples, we find that the Stark field manifests itself primarily as a transfer of oscillator strength rather than as a Stark shift. Therefore, bleached features due to the carrier induced fields appear at the position of allowed ground state transitions, in agreement with the experimental results.

2.6 References

1. Al. L. Efros and A. L. Efros, Fiz. Tekh. Poluprovodn. **16**, 1209 (1982) [Sov. Phys. Semicond. **16**, 772 (1982)].
2. L. E. Brus, J. Chem. Phys. **80**, 4403 (1984).
3. S. Schmitt-Rink, D. A. B. Miller, and D. S. Chemla, Phys. Rev. B**35**, 8113 (1987).
4. M. G. Bawendi, P. J. Carroll, W. L. Wilson, and L. E. Brus, J. Chem. Phys. **96**, 946 (1992).
5. A. P. Alivisatos, A. L. Harris, N. J. Levinos, M. L. Steigerwald, and L. E. Brus, J. Chem. Phys. **89**, 4001 (1988).
6. M. G. Bawendi, W. L. Wilson, L. Rothberg, P. J. Carroll, T. M. Jedju, M. L. Steigerwald, and L. E. Brus, Phys. Rev. Lett. **65**, 1623 (1990).
7. N. Peyghambarian, B. Fluegel, D. Hulin, A. Migus, M. Joffre, A. Antonetti, S. W. Koch, and M. Lindberg, IEEE J. Quantum Electronics **QE-25**, 2516 (1989).
8. U. Woggon, S. Gaponenko, W. Langbein, A. Uhrig, and C. Klingshirn, Phys. Rev. B**47**, 3684 (1993).
9. E. F. Hilinski, P. A. Lucas, and Y. Wang, J. Chem. Phys. **89**, 3435 (1988).
10. P. Roussignol, D. Ricard, C. Flytzanis, and N. Neuroth, Phys. Rev. Lett. **62**, 312 (1989).
11. D. J. Norris, M. Nirmal, C. B. Murray, A. Sacra, and M. G. Bawendi, Z. Phys. D **26**, 355 (1993).
12. M. O'Neil, J. Marohn, and G. McLendon, J. Phys. Chem. **94**, 4356 (1990).
13. A. Eychmüller, A. Hässelbarth, L. Katsikas, and H. Weller, Ber Bunsenges. Phys. Chem. **95**, 79 (1991).
14. C. B. Murray, D. J. Norris and M. G. Bawendi, J. Am. Chem. Soc. **115**, 8706 (1993).
15. J. B. Xia, Phys. Rev. B**40**, 8500 (1989).
16. G. B. Grigoryan, E. M. Kazaryan, Al. L. Efros and T. V. Yazeva, Sov. Phys. Solid State **32**, 1031 (1990).
17. A. I. Ekimov, F. Hache, M. C. Schanne-Klein, D. Ricard, C. Flytzanis, I. A. Kudryavtsev, T. V. Yazeva, A. V. Rodina, and Al. L. Efros, J. Opt. Soc. Am. B**10**, 100 (1993).
18. Y. Z. Hu, M. Lindberg, and S. W. Koch, Phys. Rev. B**42**, 1713 (1990).
19. W. H. Press, B. P. Flannery, S. A. Teukolsky, and W. T. Vetterling, *Numerical Recipes in C* (Cambridge University Press, Cambridge, 1988), Chapter 14.
20. Y. Wang and N. Herron, Phys. Rev. B**42**, 7253 (1990).
21. *Landolt-Bornstein Numerical Data and Functional Relationships in Science and Technology*, New Series, Group III Vol. 17b, K. H. Hellwege Editor, Springer-Verlag, Berlin, 1982.
22. Al. L. Efros, Phys. Rev. B**46**, 7448 (1992).
23. Al. L. Efros and A. V. Rodina, Phys. Rev. B**47**, 10005 (1993).
24. M. Nirmal, D. J. Norris, M. Kuno, M. G. Bawendi, Al. L. Efros, M. Rosen (submitted).
25. M. Nirmal, C. B. Murray, and M. G. Bawendi, Phys. Rev. B**50**, 2293 (1994).
26. A. Sacra, D. J. Norris, C. B. Murray, M. G. Bawendi, J. Chem. Phys. (in press).
27. F. Hache, D. Ricard, and C. Flytzanis, Appl. Phys. Lett. **55**, 1504 (1989).
28. V. L. Colvin and A. P. Alivisatos, J. Chem. Phys. **97**, 730 (1992).
29. W. L. Wilson, P. F. Szajowski, and L. E. Brus, Science **262**, 1242 (1993).

Chapter 3

Refined Measurement and Assignment of the Exciton Spectrum*

3.1 Introduction

A primary motivation in the study of nanometer scale semiconductor crystallites (or quantum dots) is to understand how the size of a semiconductor material influences its electronic properties. Quantum dots provide an opportunity to study the evolution of electronic behavior in a size regime intermediate between the molecular and bulk limits of matter. Interesting and strongly size dependent optical properties arise in these materials when the quantum dot is small compared to the natural length scale of the electron-hole pair, the exciton Bohr radius.[1,2] In this limit, referred to as the strong confinement regime,[1] the electron and hole wavefunctions experience three-dimensional quantum confinement due to the dot boundary. The confinement induces quantization of the bulk electronic bands such that quantum dots, sometimes called "artificial atoms", have discrete electronic transitions that shift to higher energies with decreasing size. These basic properties have been clearly demonstrated by numerous optical studies on II-VI semiconductor quantum dots, such as CdS and CdSe.[3-23]

However, one of the original and basic experimental questions about quantum dots — how their electronic spectra evolve with size in the strong confinement regime — remains largely unanswered. Early work on this question[3-10] was constrained by difficulties in preparing high quality, monodisperse samples. Inhomogeneities such as distributions in size and shape which conceal the higher transitions prevented a more complete investigation. Early efforts were limited both in the number of sizes as well as the number of states which were investigated. More recent studies[11-14] which do examine quantum

* Much of chapter 3 will appear in print: D. J. Norris and M. G. Bawendi, Phys. Rev. B (submitted).

dots of sufficient quality to resolve many of the higher states are restricted to one[11-13] or a few[14] sizes.

New methods in quantum dot fabrication now allow the size dependence question to be more satisfactorily addressed. We prepare colloidal CdSe quantum dots with a synthetic procedure[15] which provides extremely monodisperse (<4% rms) II-VI quantum dots ranging from ~15 to ~120Å in diameter, a size range which spans the strong confinement regime for CdSe.[24] In chapter 2 we used transient differential absorption (TDA) spectroscopy to report preliminary results on the size dependent spectrum of CdSe quantum dots in the strong confinement regime.[16] Although TDA effectively increases the resolution of the spectrum by optically selecting and bleaching a subset of the quantum dots, competition between bleach features and induced absorptions complicates the analysis. Here we present a more detailed investigation of the size dependent spectrum using photoluminescence excitation (PLE) spectroscopy which avoids this situation. We examine a much larger sample series and study the evolution of ten quantum dot absorption features as a function of dot diameter.

3.2 Experimental

We prepare CdSe quantum dots according to the method of Ref. 15. In this procedure the wet chemical synthesis is followed by size-selective precipitation to further narrow the size distribution. Highly monodisperse (<4% rms) samples are obtained which contain slightly prolate (aspect ratio 1.0 to 1.3), near defect-free, wurtzite crystallites with well passivated surfaces.[15,25,26] The dots exhibit strong band edge luminescence with a quantum yield (at 10K) greater than 0.1 and measured as high as 0.9. The intensity of deep trap emission, which dominates the luminescence behavior of dots prepared by many other methods, is size-dependent in our samples. Negligible in our largest dots, it slowly increases with decreasing size and becomes significant in our smallest size samples.

We study twenty-four samples with mean diameters ranging from ~24Å to ~105Å.[27] Three of the samples were used in our previous TDA results[16,22] (chapters 2 and 4). These older samples were isolated from the growth solution and redispersed in tri-n-butyl-phospine (TBP) with *o*-terphenyl added (200mg/ml) to form an optically clear organic

glass at cryogenic temperatures. Most samples, however, are isolated and redispersed in n-hexane with a small amount of tri-n-octyl-phosphine (TOP). An excess of TBP or TOP, both surface capping groups, maintains surface passivation and preserves the high photoluminescence quantum yield.[28] While our preparation method produces almost any desired dot diameter, certain sizes ("magic sizes") are preferred in the growth process.[15] Small dots (with their first absorption peak between ~2.58 and ~2.48eV) which are between two magic sizes seem to be the least stable. Over weeks their spectra broaden when stored at room temperature, presumably due to continued slow growth. To avoid this complication we record PLE spectra for the six smallest dot sizes immediately after preparation with the dots still in the reaction solution. Larger samples (with the first absorption peak <2.48eV) are stable for much longer (>months) periods of time.

For optical measurements each sample is placed between sapphire flats separated by a 0.5mm thick Teflon spacer and mounted in a helium cryostat. All spectra are obtained at 10K. We record photoluminescence and photoluminescence excitation (PLE) spectra using a SPEX Fluorolog-2 spectrofluorometer. This instrument consists of two double (0.22m) spectrometers. The first selects the desired excitation energy from the emission of a xenon arc lamp. The second chooses the emission energy detected by a photomultiplier tube (R928). Under experimental conditions for PLE the combined resolution of our instrument was ~3meV (FWHM).

3.3 Measurement of the Exciton Spectrum

Although the quality of our samples is among the highest reported, inhomogeneities remain which broaden absorption features and conceal transitions. PLE reduces these effects by optically selecting a subset of the sample distribution.[11] In Fig. 3.1 we demonstrate this technique along with absorption and luminescence spectra for ~56Å diameter dots.[27] When excited well above the first transition, emission occurs from the entire sample distribution and a broad luminescence band is observed (FWHM 56meV, dashed line in Fig. 3.1a). However, fluorescence line narrowing (FLN) experiments[11,17,18] show that "single dot" emission is characterized by a vibrational (LO phonon) progression with much narrower features (FWHM ~8meV). The difference between the single dot and

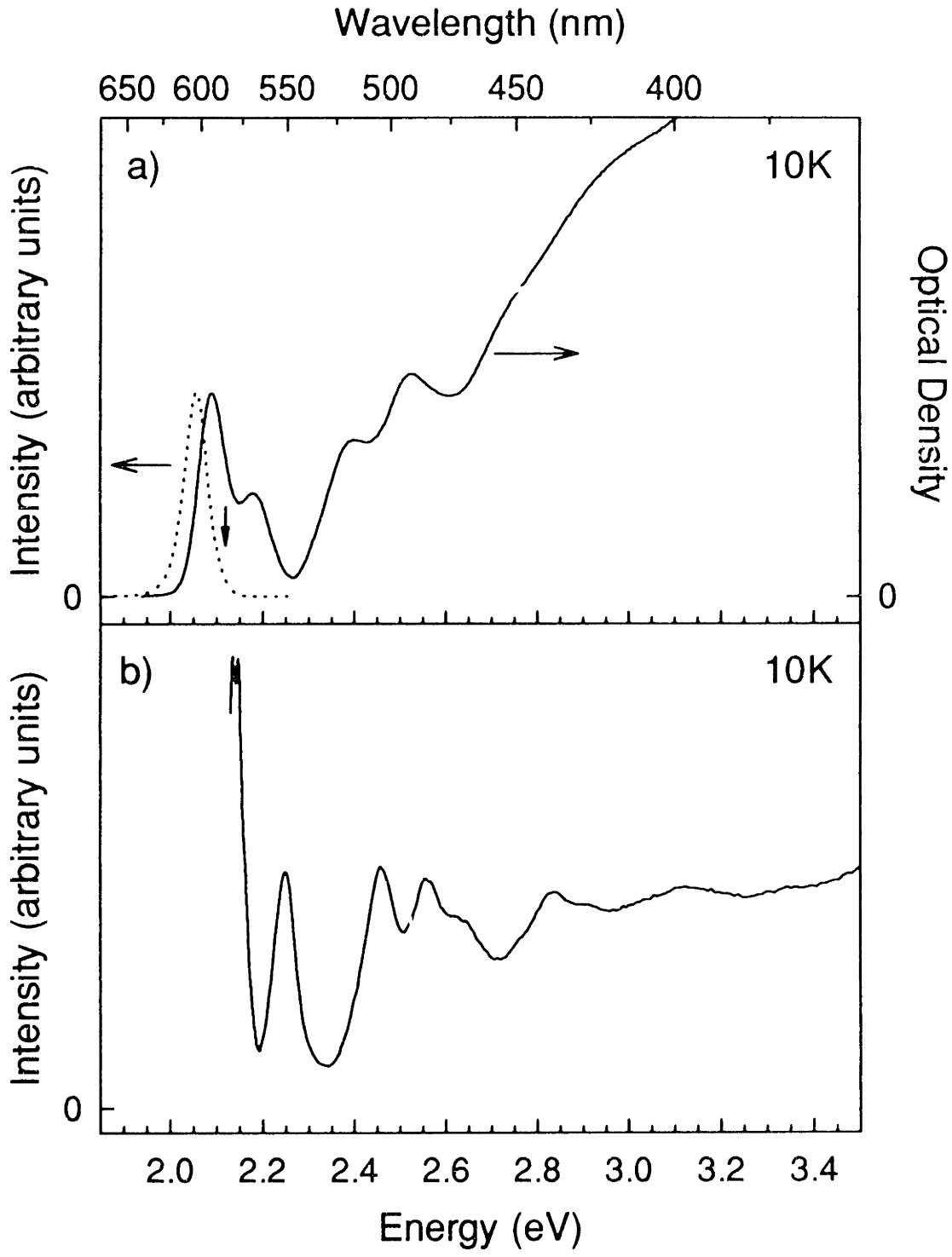

FIG. 3.1 (a) Absorption (solid line) and photoluminescence (dashed line) spectra for ~56Å diameter quantum dots. In luminescence the sample was excited at 2.655eV (467.0nm). The downward arrow marks the emission position monitored in PLE. (b) PLE scan for ~56Å diameter dots.

inhomogeneous emission linewidths allows PLE to select a specific portion of the sample distribution. By monitoring a narrow spectral band of the full luminescence while scanning the excitation energy, PLE reveals absorption features with inhomogeneous broadening greatly reduced.[11,19-21] As seen in Fig. 3.1, transitions which overlap in direct absorption (Fig. 3.1a) are resolved by PLE (Fig. 3.1b).

To obtain PLE data for each sample we first measure its broad luminescence band. Since features are most efficiently resolved in PLE when the emission is monitored on the blue edge of the luminescence,[11] we then generally select an emission energy where the blue edge intensity is ~1/3 the peak height. For example, in Fig. 3.1b we use the energy denoted by the downward pointing arrow in Fig. 3.1a. We then record PLE spectra at emission positions slightly to the red and to the blue of this original energy (generally +/- 5nm). This allows us to increase the number of "sizes" which are investigated since the emission energy chosen in PLE decides which subset of the sample distribution is probed. Below we analyze 53 different "sizes" generated from 24 samples.

In Figs. 3.2, 3.3, and 3.4 we show one PLE spectrum for each of our samples. The quantum dots are grouped into "small" (Fig. 3.2, ~24Å to ~33Å in diameter), "medium" (Fig. 3.3, ~35Å to ~50Å in diameter), and "large" (Fig. 3.4, ~53Å to ~105Å in diameter) subgroups[27] and are arranged in order of increasing diameter. Quantum confinement clearly shifts the transitions blue with decreasing size. The high quality of our dots allows us to resolve as many as eight absorption features in a single spectrum. We also observe additional structure on the first absorption peak, as seen in Figs. 3.2-3.4. In most spectra a narrow line with LO phonon replicas is observed on top of a much broader feature. Similar narrow and broad sub-structure is seen in TDA experiments[11,16,22] and may represent experimental evidence of fine structure in the first quantum dot transition.[22] These additional features will be discussed in chapters 4, 5, and 6. Here we focus solely on the higher excited states.

Figures 3.2-3.4 present raw experimental data which describe the quantum dot spectrum as a function of dot size. To quantify this information we extract the energies of the quantum dot transitions using the fitting procedure demonstrated in Fig. 3.5. Each

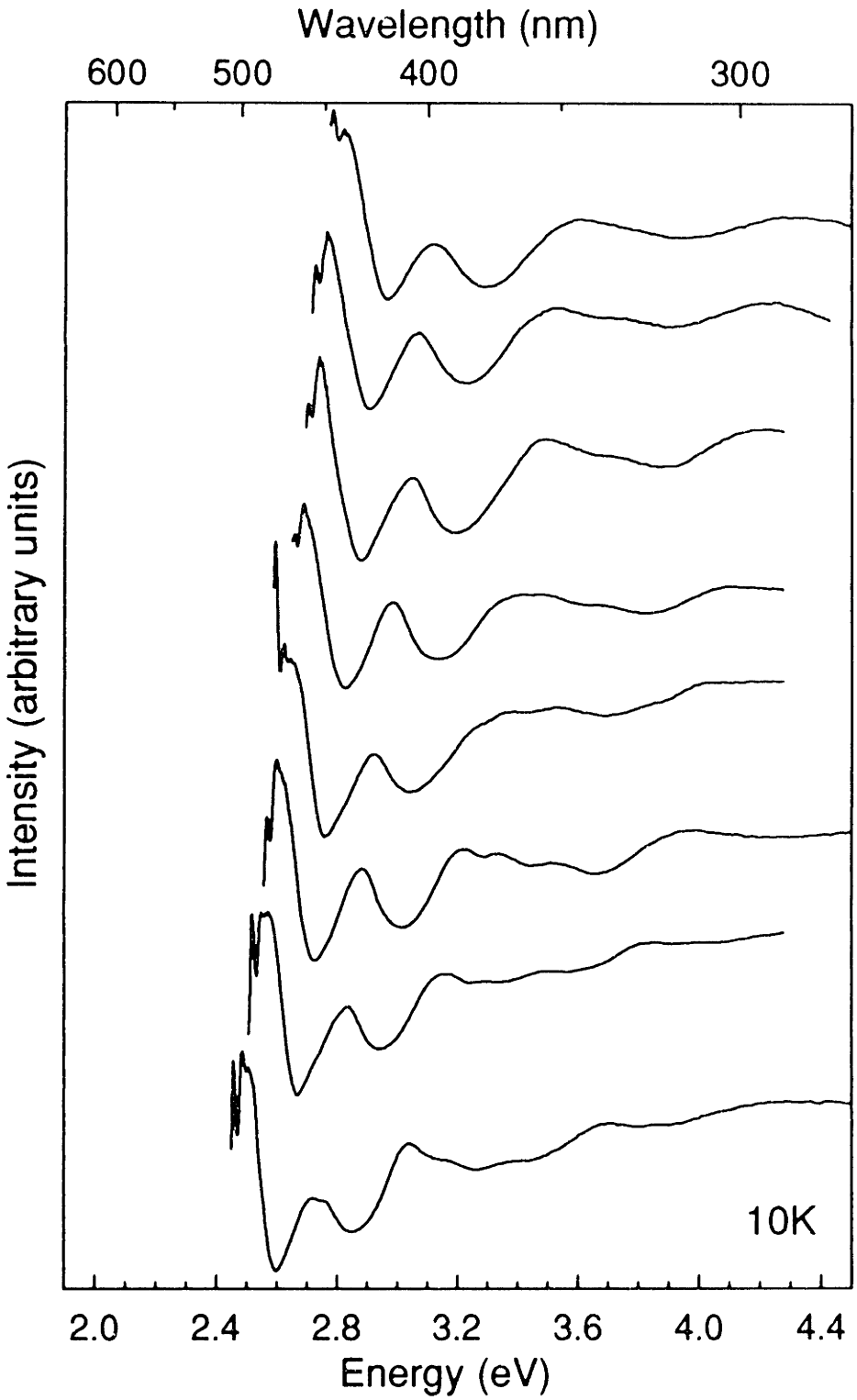

FIG. 3.2 Normalized PLE scans for eight different "small" size quantum dot samples. Size increases from top to bottom and ranges from ~24Å to ~33Å in diameter.

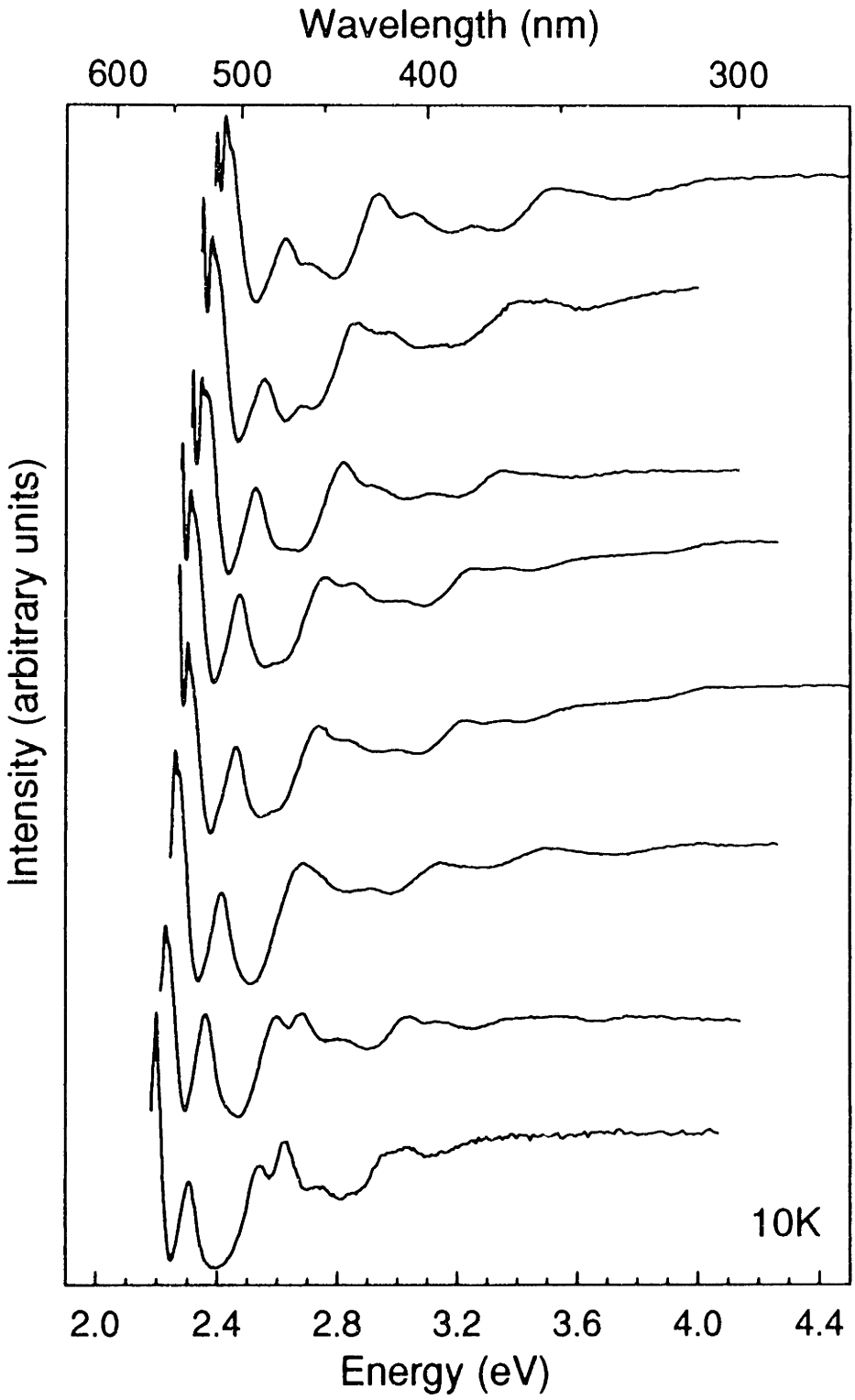

FIG. 3.3 Normalized PLE scans for eight different "medium" size quantum dot samples. Size increases from top to bottom and ranges from ~35Å to ~50Å in diameter.

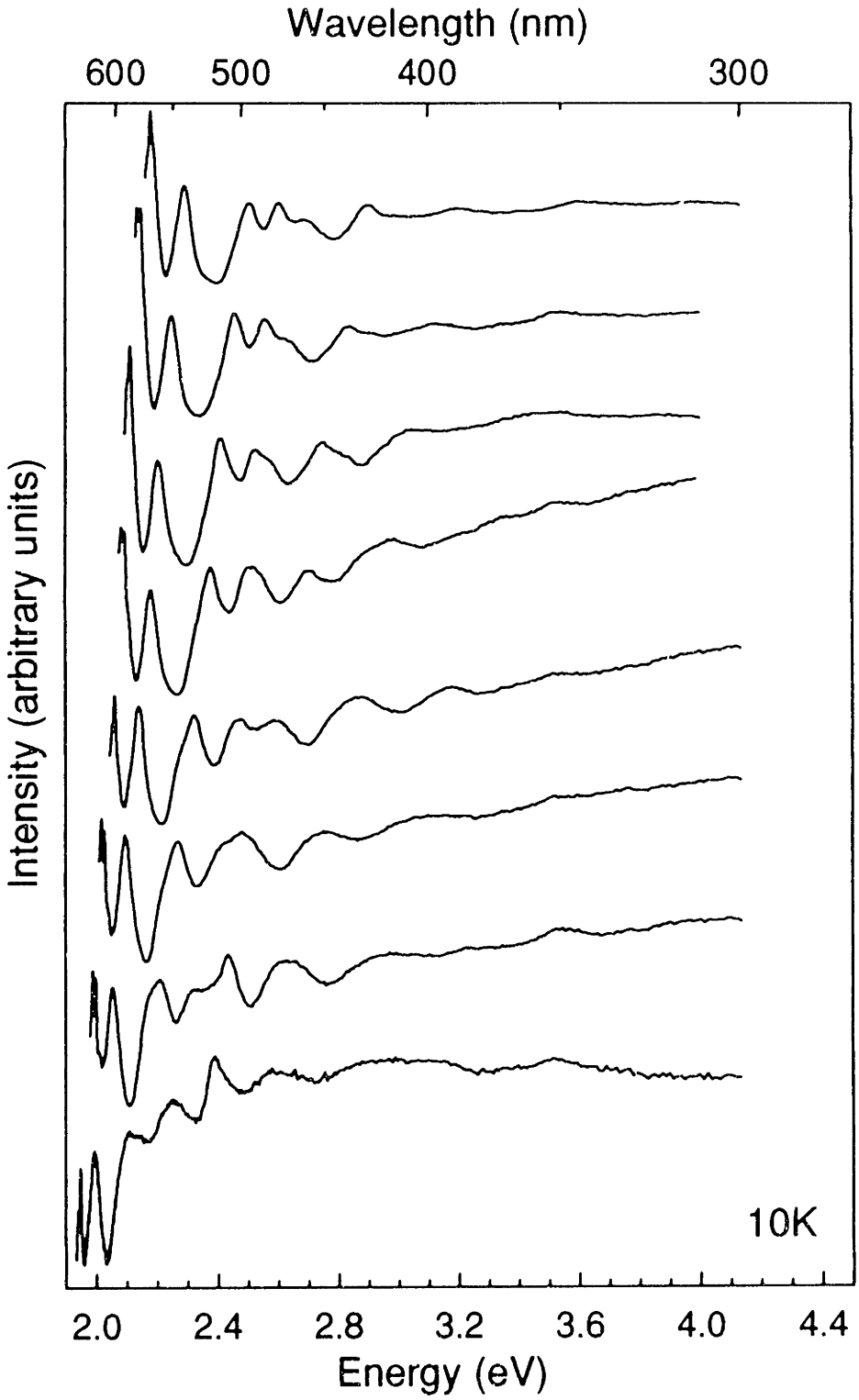

FIG. 3.4 Normalized PLE scans for eight different "large" size quantum dot samples. Size increases from top to bottom and ranges from ~53Å to ~105Å in diameter. In many of the scans a broad lamp artifact appears at ~3.5eV. This feature was ignored in the data analysis.

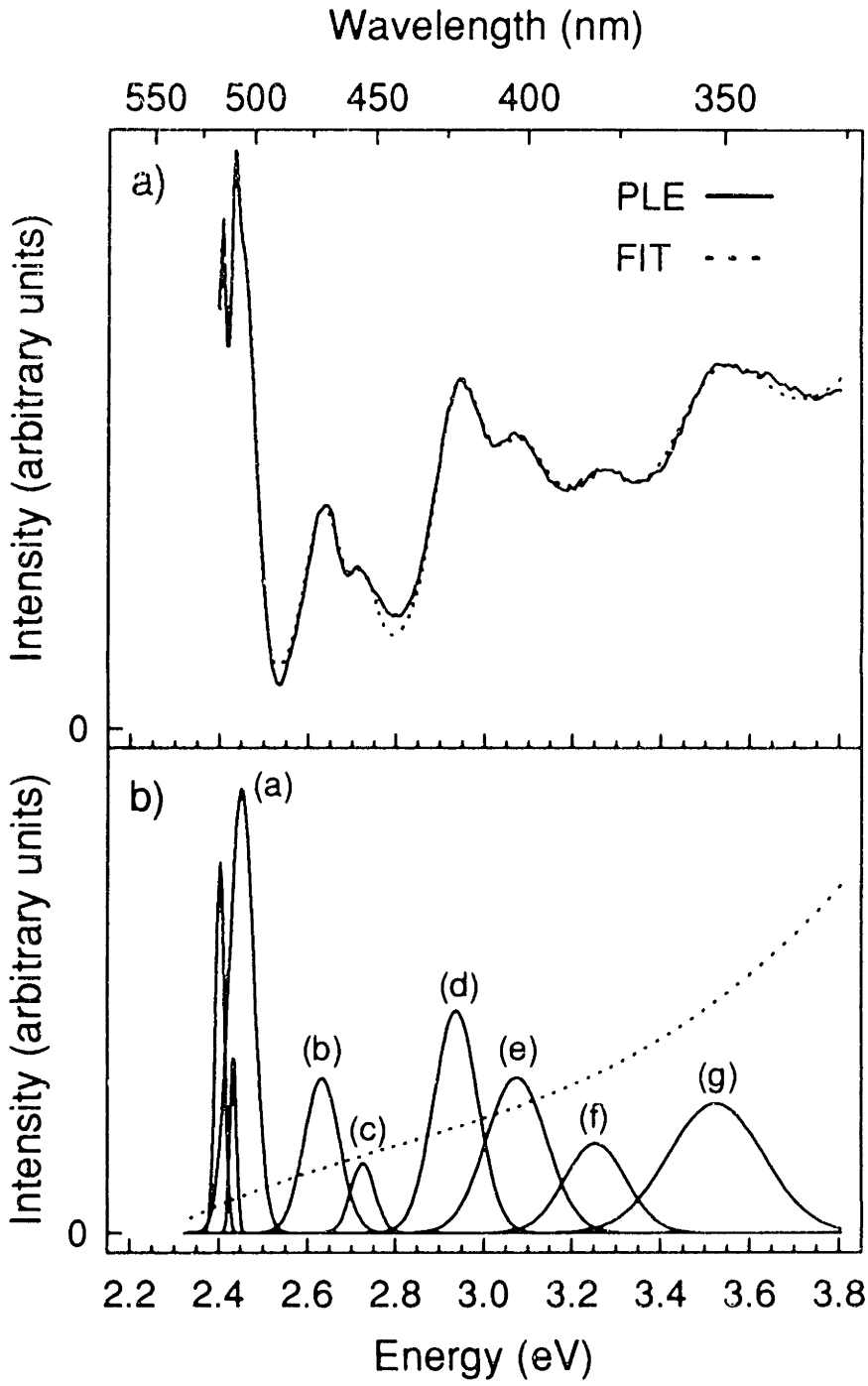

FIG. 3.5 (a) Demonstration of the fitting procedure used to extract PLE peak positions. The PLE scan (solid line) is compared to the fit (dashed line) for a ~35Å diameter sample. The structure on the first absorption is clearly visible in this plot. (b) The individual Gaussian components (solid lines) and the cubic background (dashed line) which combine to form the fit. The first absorption peak is decomposed into two narrow features slightly to the red of a broader absorption peak. For comparison the peaks are labeled as in Fig. 3.6.

PLE spectrum is fit with a sum of Gaussians using standard nonlinear least squares methods.[29] To model the continuum-like nature of underlying transitions which are not resolved we use a cubic background curve (dashed line in Fig. 3.5b). The narrow and broad components of the lowest transition, mentioned above, are clearly observed in Fig. 5. The broad component, which carries most of the oscillator strength, is used for the energy of the first transition in our analysis.

In agreement with previous work, our fits show that transition linewidths increase with increasing energy[11,19] (Fig. 3.5) and decreasing size.[16,19] Rough estimates of oscillator strength based on our fits also confirm that excited state transitions are comparable to or weaker than the first transition, as expected from theory.[14,34] Unfortunately, a more quantitative analysis of the transition strengths is prevented by the presence of the unresolved states, modeled by the cubic background. In addition, since PLE represents a combination of absorption and emission behavior, a detailed knowledge of emission quantum yield for each transition would be required to quantify the absorption strength of the states observed in PLE.[19]

The final results of the fitting procedure for our entire data set are shown in Fig. 3.6. In this plot we choose what may seem to be unusual axes. The x-axis is the energy of the first excited state. Energy is more easily and precisely measured than dot size and is also a better size dependent label. Using the average radius as determined by transmission electron microscopy (TEM) as the x-axis would introduce significant size measurement error, both systematic and random. In addition, the mean sizes obtained would not represent the subset of the size distribution that is measured in PLE. The energy of the first transition better describes those dots which are actually probed. The y-axis is energy relative to the first excited state.

Figure 3.6 summarizes our experimental results and shows the size-dependent spectrum of CdSe quantum dots in the strong confinement regime. While Figs. 3.2-3.4 show only one PLE spectrum per sample, Fig. 3.6 shows all of our data (53 "sizes") and includes several PLE scans per sample, as discussed above. Our spectra describe the size evolution of ten quantum dot absorption features, labeled (a) through (j) in Fig. 3.6.

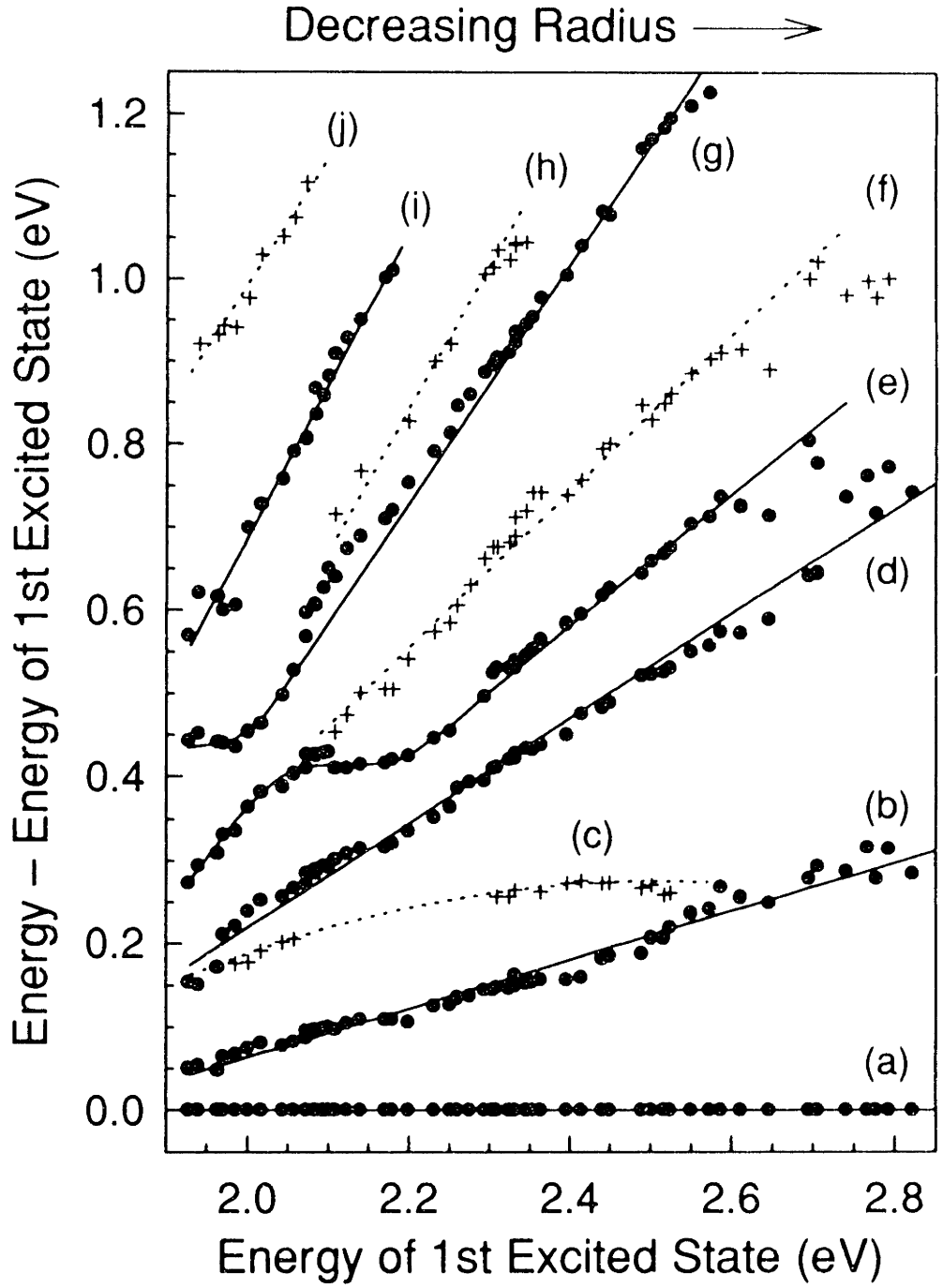

FIG. 3.6 Transition energies (relative to the first excited state) vs. the energy of the first excited state. Peak positions are extracted from PLE data as described in the text and shown in Fig. 3.5. While Figs. 3.2-3.4 show one PLE scan per sample, this plot shows all of our PLE data, including several PLE scans per sample. Strong (weak) transitions are denoted by circles (crosses). The solid (dashed) lines are visual guides for the strong (weak) transitions to clarify their size evolution.

Strong (weak) features are denoted by circles (crosses) with solid (dashed) lines drawn as visual guides to clarify their size evolution. We note that due to complications with overlapping induced absorptions, the four weak transitions in Fig. 3 6 (dashed lines) were not observed in our TDA results in chapter 2.[16]

3.4 The Exciton Spectrum: Theoretical Overview

The size range studied in this chapter is in the strong confinement regime[1,2] where the confinement energy of the electron and hole is much larger than their Coulomb interaction. The carriers can then be treated independently and the Coulomb term included as a perturbation. Working in the strong confinement limit allows the theoretical problem to be conveniently divided into separate electron and hole components. The electron and hole wavefunctions are each described by the product of a unit cell basis function and an envelope function which satisfies the spherical boundary condition. Since the unit cell components are assumed identical to the bulk, quantum dot theory focuses on determining the envelope functions of the individual carriers.

Early theoretical work[1,2] assumed a simple two band isotropic effective mass model to approximate the bulk valence and conduction bands. When confined by an infinite potential barrier at the dot boundary, each carrier is described by a "particle-in-a-sphere" envelope function, the product of a spherical harmonic and a spherical Bessel function. The hole (electron) envelope function is labeled by its angular momentum, L_h (L_e), and radial quantum number, n_h (n_e). The total quantum dot wavefunction is the product of the individual hole and electron components. In this model the first excited state is written as $1S_h1S_e$, with the hole and electron both in the first (n_h=1, n_e=1) S-like (L=0) envelope function.

In general the valence band of diamond-type semiconductors, illustrated in Fig. 3.7, is more complicated than the simple parabolic band assumed above.[30] The valence band, which arises from p atomic orbitals, has an inherent six-fold degeneracy (including spin) at k=0. When spin orbit coupling (Δ) is strong this degeneracy is split into a four-fold degenerate $p_{3/2}$ band and a "split off" two-fold degenerate $p_{1/2}$ band. [The subscript

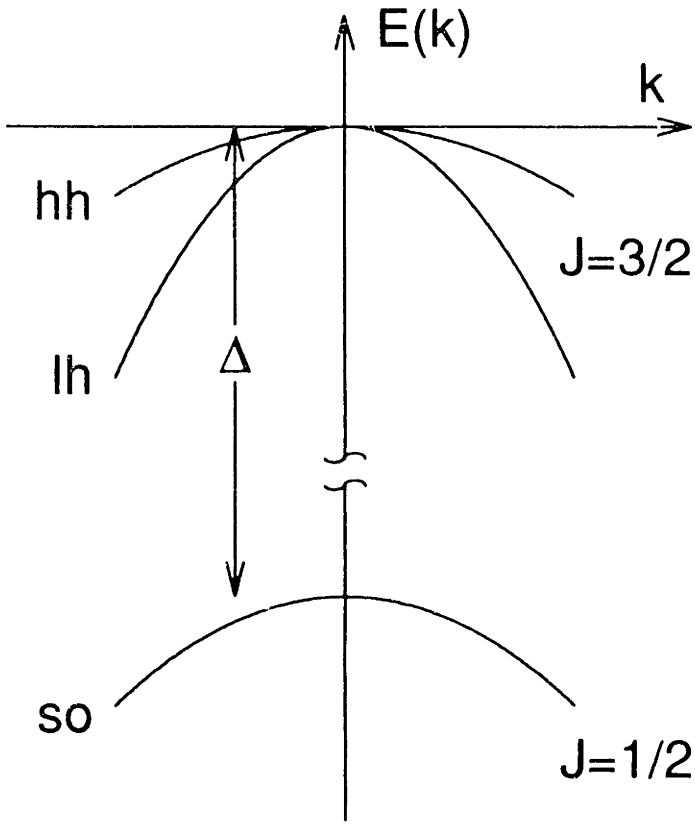

FIG. 3.7 Illustration of the valence band for diamond-type semiconductors near k=0, which is split into heavy hole (hh), light hole (lh), and split off hole (so) sub-bands. Δ is the spin orbit coupling. The valence band structure of CdSe with cubic (zinc blende) symmetry is well approximated by this structure.

describes the total unit cell angular momentum ($J = \ell + s$).] Away from k=0 the J=3/2 band splits further into the heavy hole (J_m=±3/2) and light hole (J_m=±1/2) bands, both doubly degenerate.[30]

More recent quantum dot theoretical work[14,34-38] considers the valence band degeneracy and includes a better description of the CdSe valence band. For convenience theory assumes a cubic (zinc blende) crystal lattice. [Below we discuss the effects of the correct hexagonal (wurtzite) lattice.] In this case the CdSe valence band is well approximated near k=0 by the diamond-like band structure[30-33] (Fig. 3.7) and is described by the Luttinger Hamiltonian.[39,40] When this Hamiltonian is combined with a spherical

potential in the spherical band approximation, mixing between the bulk valence bands occurs.[41,42] While this mixing is weak in bulk excitons,[41] it is significant in quantum dots.[14,34-38] The main result is that parity and the total hole angular momentum, $F=L_h+J$, are the only good quantum numbers for the hole envelope function. L_h and J are not conserved. Quantum dot hole states have contributions from L_h and L_h+2 spherical harmonics, commonly referred to as "S-D mixing", as well as contributions from the heavy hole, light hole, and split-off valence sub-bands. Following the notation of Ref. 14, we label quantum dot hole states as n_hL_F, where L_F designates the combination of L and $L+2$ spherical harmonics which have total angular momentum F. The electron envelope function, not affected by the valence band complexities, is still labeled by n_eL_e. In this notation the first excited pair state is labeled as $1S_{3/2}1S_e$ but contains the three hole components: (F=3/2, J=3/2, L_h=0), (F=3/2, J=3/2, L_h=2), and (F=3/2, J=1/2, L_h=2). A special notation is required for transitions involving the P-like hole states with F=1/2. These hole states are not affected by valence band mixing and states arising from the light hole sub-band ($1P^{\ell}_{1/2}$) must be distinguished from those from the split off sub-band ($1P^{so}_{1/2}$).[14]

A rigorous treatment of the valence band is important not only for determination of pair state energies but also for selection rules. Quantum dot transition strengths are determined by the overlap between electron and hole envelope functions.[1] Due to the valence band mixing, the simple selection rules of early theories, $\Delta n = 0$ and $\Delta L = 0$,[1] are no longer valid.[34]

3.5 Calculations

We assign the features of Fig. 3.6 by calculating quantum dot transitions as a function of size using the effective mass theory of Ref. 14 which includes valence band mixing and uses the Kane model[33,43] to incorporate the nonparabolicity of the conduction band. While the hole calculations assume an infinite potential boundary condition, a finite barrier (V_e) is used for the much lighter electron to allow penetration into the surrounding matrix.[44]

While our hole calculations strictly follow Ref. 14, a simplified boundary condition, better suited to our system, is used for the electron. Electron eigenvalues are evaluated by numerically solving the boundary condition[45]

$$\left[1+2f+\frac{E_p}{3}\left(\frac{2}{E+E_g/2}+\frac{1}{E+E_g/2+\Delta}\right)\right]\frac{\partial}{\partial r}\ln\left[j_\ell\left(k_s r\right)\right]\Big|_{r=a} = \frac{\partial}{\partial r}\ln\left[K'_\ell\left(k_m r\right)\right]\Big|_{r=a} \tag{3.1}$$

which matches the semiconductor conduction band with the surrounding matrix. A simple free-electron form is assumed for the matrix, which in our samples is an organic solvent. Here a is the quantum dot radius, E_g is the semiconductor band gap, Δ is the spin-orbit coupling, $j_\ell(z)$ is the ℓ^{th} order spherical Bessel function, and

$$K'_\ell(z) = (\pi/2z)^{1/2} K_{\ell+1/2}(z), \tag{3.2}$$

with $K_{\ell+1/2}(z)$ the modified Bessel function. The energy of the electron level (E) is measured from mid-gap. The wave vectors in the semiconductor (k_s) and matrix (k_m) are given by

$$k_s^2 = \frac{2m_0}{\hbar^2}\left[E-E_g/2\right]\left[1+2f+\frac{E_p}{3}\left(\frac{2}{E+E_g/2}+\frac{1}{E+E_g/2+\Delta}\right)\right]^{-1}$$

$$k_m^2 = -\frac{2m_0}{\hbar^2}\left[E-V_e-E_g/2\right], \tag{3.3}$$

where m_0 is the free electron mass. In these equations E_p and f are Kane model parameters which describe the conduction band curvature. E_p (f) accounts for the influence of the valence band (higher bands) on the conduction band.[46] Since E_p and f are related to m_e, the effective mass of the electron at the bottom of the conduction band,[46] the electron levels are described by the parameters: Δ, E_g, V_e, m_e, and E_p.

In any model the electron-hole Coulomb interaction is problematic because it cannot be addressed analytically. Within the strong confinement approximation the Coulomb term is typically included as a first order energy correction. We correct pair states to first order by adjusting states which contain S_e (P_e) by $-1.8e^2/\epsilon a$ ($-1.7e^2/\epsilon a$), where ϵ is the semiconductor dielectric constant.[2] This approximation is used since a more rigorous

approach is not necessary to assign the transitions. However, more detailed treatments by Koch and co-workers demonstrate that even in the strong confinement regime the Coulomb term can be important.[38,47] In particular the electron-hole pair states are mixed by the Coulomb interaction. Since our assignments ignore this effect, the labels we use below are in reality only approximate. Consequences of the Coulomb mixing are discussed further below.

We use standard nonlinear least squares methods[29] to globally fit a subset of the experimental data. We use size estimates for our data and fit the $1S_{3/2}1S_e$, $2S_{3/2}1S_e$ and $1P_{3/2}1P_e$ transitions to features (a), (b), and (d) in Fig. 3.6. These transitions are chosen since they exhibit simple size dependent behavior (no avoided crossings) and their assignment is relatively certain. Our fitting routine adjusts three parameters: the Luttinger band parameters γ_1 and γ,[40] which describe the curvature of the three valence sub-bands, and the potential barrier for the electron, V_e. We assume that the parameters Δ, E_g, m_e, and E_p are well represented by literature values [Δ = 0.42eV,[48] E_g(10K) = 1.839eV,[48] $m_e = 0.11m_0$,[14] E_p = 17.5eV[14]]. Our best fit is obtained with γ_1 = 2.04 and γ = 0.58, in close agreement with Ekimov *et al.*[14] This corresponds to valence band effective masses m_{hh} = 1.14, m_{lh} = 0.31, and m_{so} = 0.49 for the heavy hole, light hole, and split off sub-bands (Fig. 3.7). The ratio of light to heavy hole effective masses, β, is 0.28. The best fit also requires that V_e = 8.9eV. Although high, it is not surprising that this parameter is not physically meaningful. It depends strongly on the particular boundary condition assumed in Eq. 3.1. In addition it incorporates not only the finite barrier for the electron but all other deviations from the model. Therefore, while in theory this parameter describes the influence of the finite boundary condition on the electron, in practice V_e is used as a fitting parameter.

Figure 3.8 compares the calculated size-dependence of the first excited state (solid line) with experimental data (crosses). The theoretical model reproduces the general trend of the experimental data, but not its curvature. Since the theory includes the nonparabolicity of the conduction band, the observed deviation implies that an additional

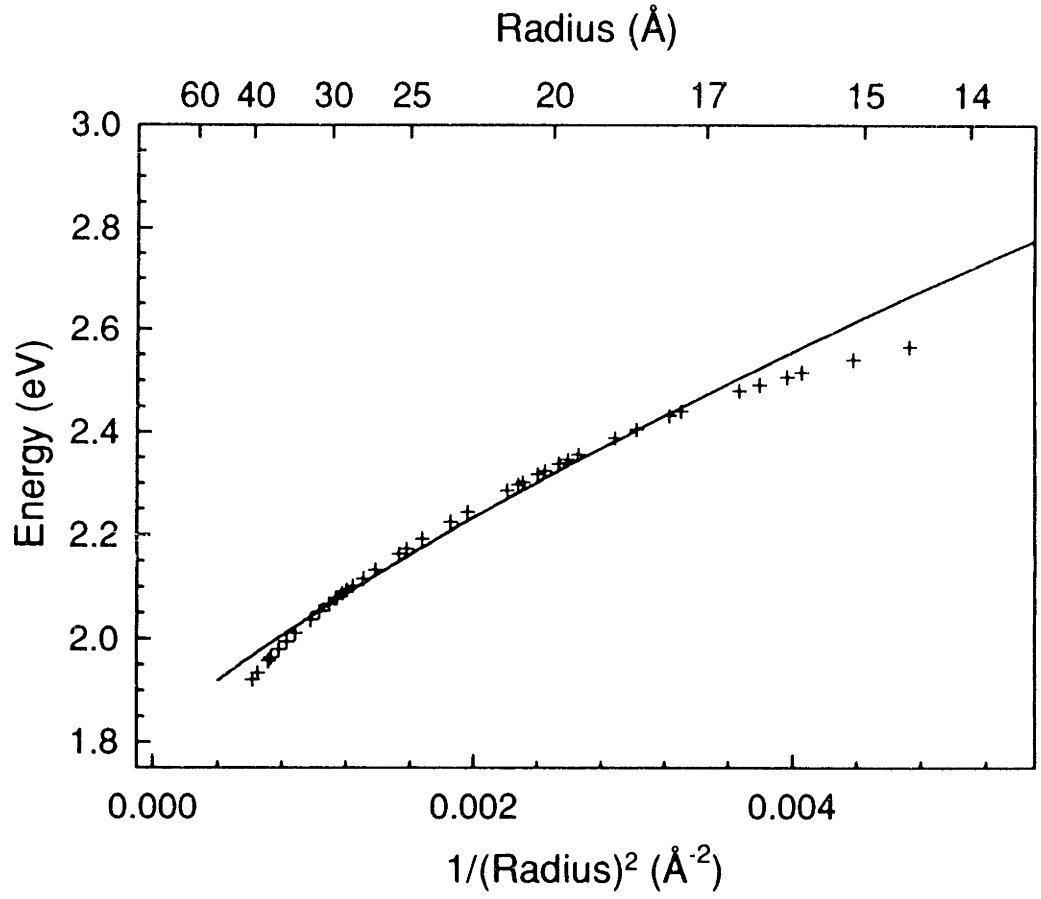

FIG. 3.8 Energy of the first excited state ($1S_{3/2}1S_e$) vs. 1/radius^2. The curve (solid line) obtained from theory is compared with PLE data (crosses).

"nonparabolicity" is present which is not accounted for by the theory. The most likely explanation for the deviation in small dots is the breakdown of the effective mass approximation. Another possibility is the simplistic choice of quantum dot boundary condition, either infinite or square-well. The data also diverge from theory at large sizes perhaps due to the increasing importance of the Coulomb interaction in the intermediate confinement regime. In any case, the discrepancy in the first transition is not large enough to keep us from our goal — assignment of the higher excited states.

The higher excited states are assigned by using the best fit parameters to calculate the energies of all allowed transitions ($n_h \leq 4$, $F_h \leq 5/2$) below feature (j) in Fig. 3.6, yielding ~60 transitions. The strength of each state is calculated and only the strongest transitions are

considered. Figures 3.9-3.12 show the best theoretical curves for features (a) through (j) from Fig. 3.6. Although the number of allowed states below feature (g) is fairly sparse and the assignments are relatively straight forward, the large density of allowed states prevents definitive assignment of features at higher energies.

3.6 Assignment of the Exciton Spectrum

Figure 3.9 compares features (a), (b), and (d) in Fig. 3.6 to the calculated $1S_{3/2}1S_e$, $2S_{3/2}1S_e$, and $1P_{3/2}1P_e$ transitions. The strong quantitative agreement between experiment and theory demonstrates the quality of the fitting procedure. These assignments are also consistent with intensity calculations which indicate that $1S_{3/2}1S_e$ and $1P_{3/2}1P_e$ should be two of the strongest transitions, as observed. $2S_{3/2}1S_e$ should be weaker but clearly resolved due to its spectral isolation. These properties are demonstrated in Fig. 3.5 where features (a) [$1S_{3/2}1S_e$] and (d) [$1P_{3/2}1P_e$] dominate the spectrum while the weaker feature (b) [$2S_{3/2}1S_e$] is observed between them.

Figure 3.10 assigns features (c), (e), and (g) to $1S_{1/2}1S_e$, $2S_{1/2}1S_e$, and $3S_{1/2}1S_e$, respectively. An avoided crossing between the $2S_{1/2}1S_e$, and $3S_{1/2}1S_e$ states which was initially reported in our preliminary results[16] in chapter 2 is now unambiguously observed at ~2.0eV. In addition we now observe a repulsion between the $1S_{1/2}1S_e$ and $2S_{1/2}1S_e$ states above 2.2eV. Both avoided crossings are predicted by theory and their presence in the data is strong support for our assignments. However, Fig. 3.10 demonstrates that theory underestimates the repulsion in both avoided crossing regions, causing theoretical deviations in the predictions of the $1S_{1/2}1S_e$ and $2S_{1/2}1S_e$ states. The Coulomb mixing of the pair states, ignored by the model, couples the $n_hS_{1/2}1S_e$ transitions such that these states "push off" each other more strongly. The Coulomb term also causes $1S_{1/2}1S_e$ and $2S_{1/2}1S_e$ to avoid one another through their individual repulsion from the strongly allowed $1P_{3/2}1P_e$ [feature (d)] which lies between them. Because of these deviations from theory feature (d) was incorrectly assigned to $1S_{1/2}1S_e$ in chapter 2.[16] The more complete data set now suggests that it is more reasonable to assign feature (c), not observed in the TDA data,[16] to $1S_{1/2}1S_e$. Feature (d) is now assigned to the $1P_{3/2}1P_e$ state, as discussed above.

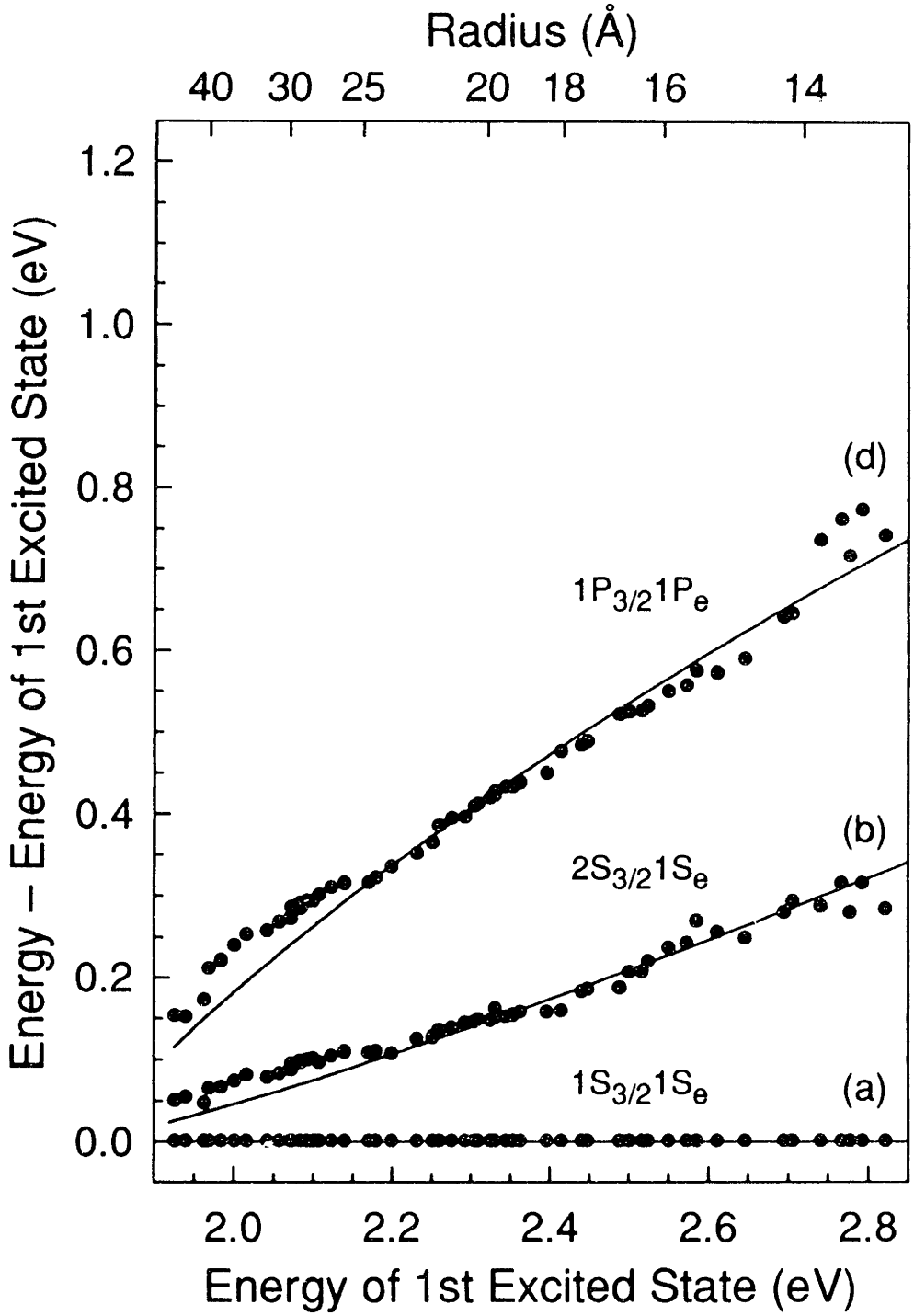

FIG. 3.9 Theoretically predicted pair states (solid lines) assigned to features (a), (b), and (d) in Fig. 3.6. The experimental data is shown for comparison (circles).

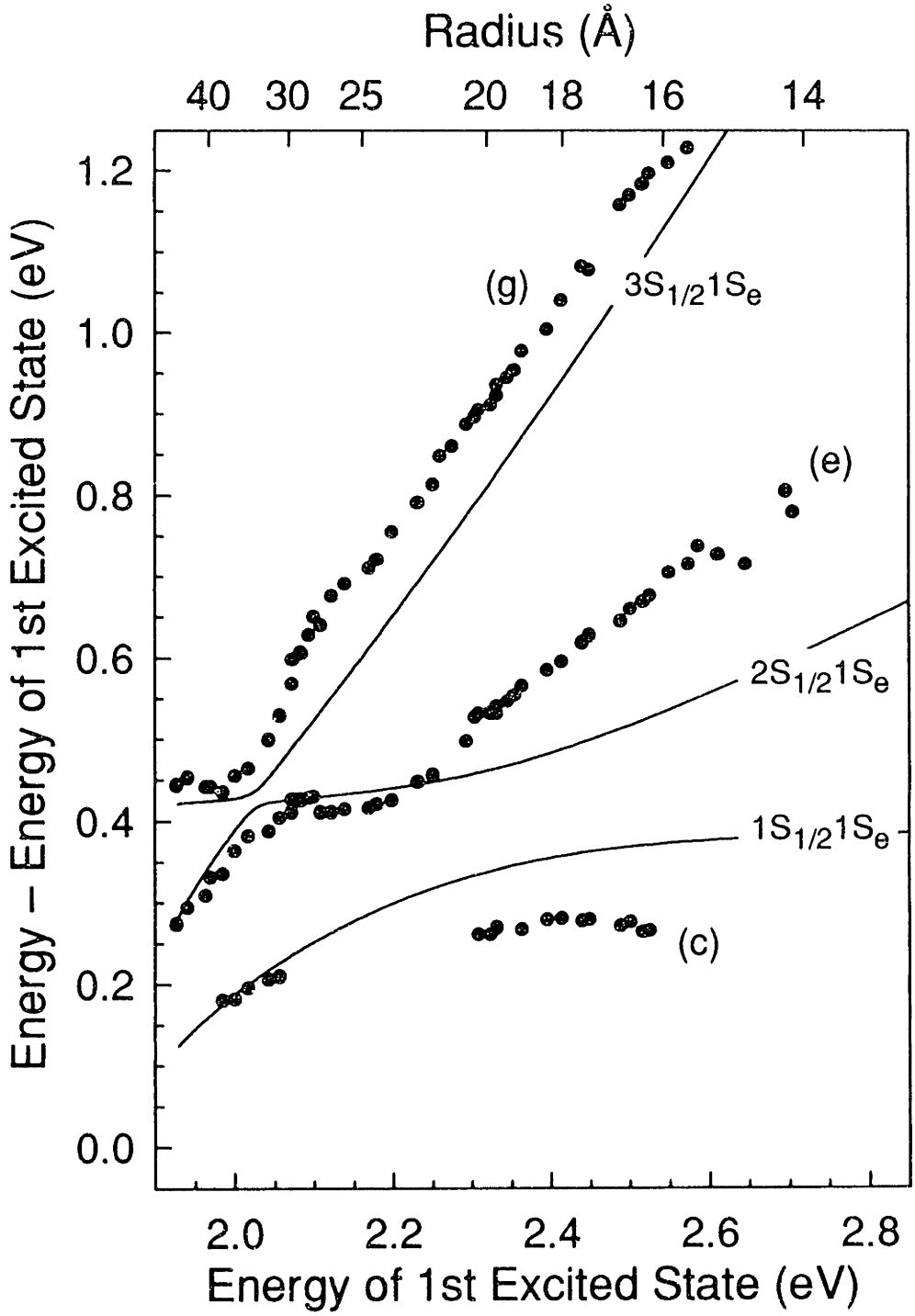

FIG. 3.10 Theoretically predicted pair states (solid lines) assigned to features (c), (e), and (g) in Fig. 3.6. The experimental data is shown for comparison (circles).

The behavior of the $n_h S_{1/2} 1S_e$ transitions demonstrates the importance of valence band structure in CdSe quantum dots since the avoided crossings are intimately related to the valence band mixing. Like the $S_{3/2}$ hole state, $S_{1/2}$ is a mixture of L_h=0 and L_h=2 components due to S-D mixing. However, in $S_{1/2}$ the S and D components arise from different valence sub-bands. The D component comes from the J=3/2 band and the S component, which carries the oscillator strength, comes from the split off J=1/2 band (see Fig. 3.7). In the absence of valence band mixing, the first S-type hole envelope function from the split off band would cause a $1S_h1S_e$-like pair state to appear 0.42eV (the spin-orbit coupling in CdSe[48]) above the first excited state. In Fig. 3.6 this transition would appear as a nearly horizontal line at 0.42eV. States containing D-type hole envelope functions from the J=3/2 bands, which carry no oscillator strength, would cross this "spin-orbit line". Once valence band mixing is considered, the intersection of these S and D states is forbidden and avoided crossings result. Below 2.0eV in Fig. 3.10 the $3S_{1/2}1S_e$ transition is mostly a $1S_h1S_e$-like pair state from the split off band (J=1/2) and the $2S_{1/2}1S_e$ and $3S_{1/2}1S_e$ states are mostly D-like hole states which try to cross the spin orbit line.

The valence band mixing also implies that the hole character of the $n_h S_{1/2} 1S_e$ states changes after an avoided crossing. When the theoretical model outlined above is used to calculate quantum dot eigenfunctions,[14] we find that the $2S_{1/2}$ hole state is 70% D-like for 60Å radius dots. After the avoided crossing with $3S_{1/2}$ the hole component becomes 97% S-like for 25Å radius dots. The S character of $2S_{1/2}$ then falls again to 67% at 10Å radius due to the interaction with the D-like $1S_{1/2}$. Such changes are important because they influence the strength of the observed transitions. In large dots $1S_{1/2}$ is mostly D-like (>80%). The $1S_{1/2}1S_e$ transition is then weakly observed due to the poor overlap of $1S_{1/2}$ with $1S_e$. However, as mixing with $2S_{1/2}$ increases, $1S_{1/2}$ becomes more S-like with decreasing dot size. This explains why experimentally $1S_{1/2}1S_e$ [feature (c)] increases in intensity with decreasing size. Although appearing as a subtle shoulder on $1P_{3/2}1P_e$ in the largest sizes, it is clearly resolved in the ~35Å diameter sample shown in Fig. 3.5. With decreasing size $1S_{1/2}1S_e$ gains strength, eventually merging with the stronger $2S_{3/2}1S_e$ transition (Fig. 3.6).

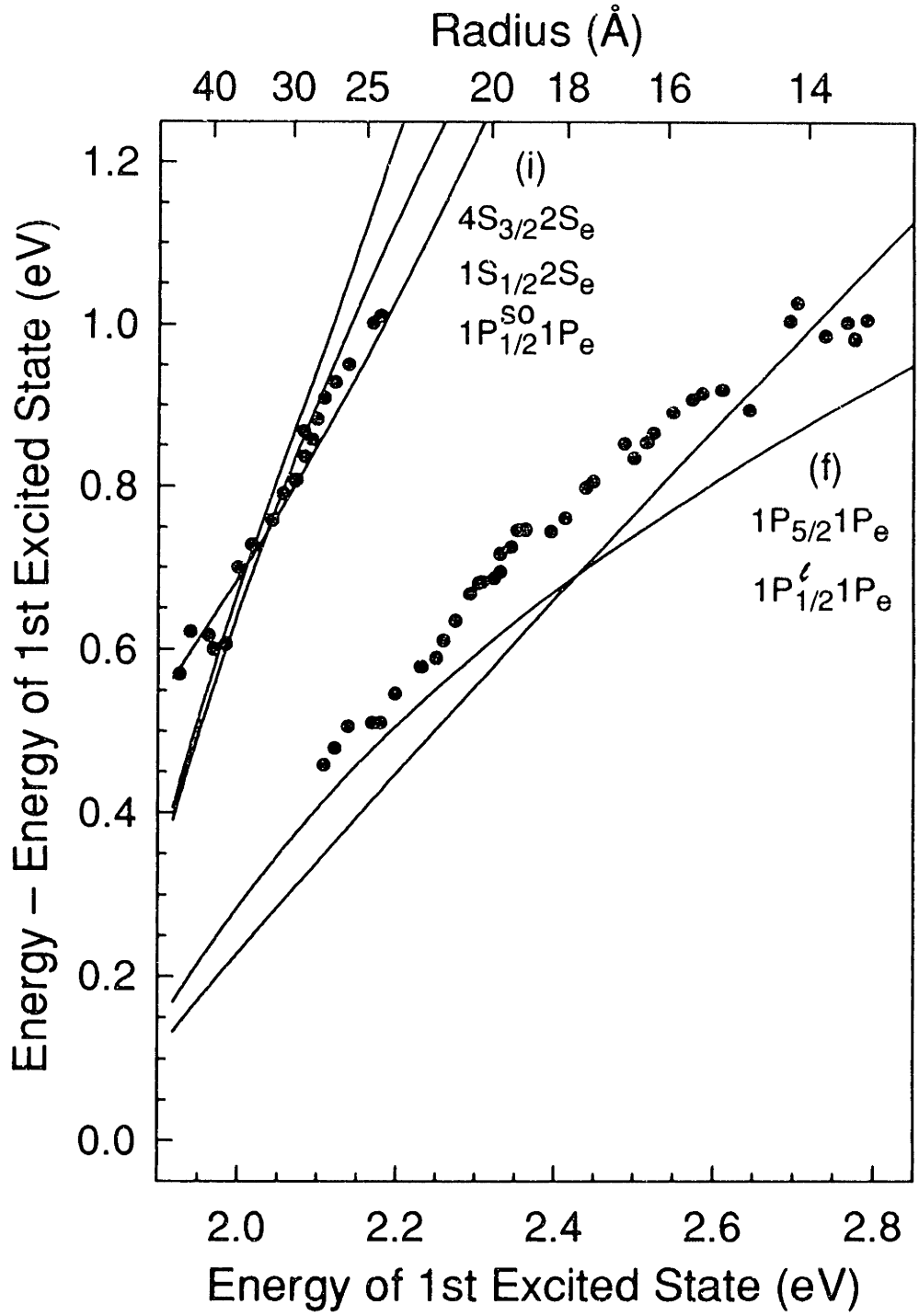

FIG. 3.11 Theoretically predicted pair states (solid lines) which are possible assignments for feature (f) and (i) in Fig. 3.6. The experimental data is shown for comparison (circles).

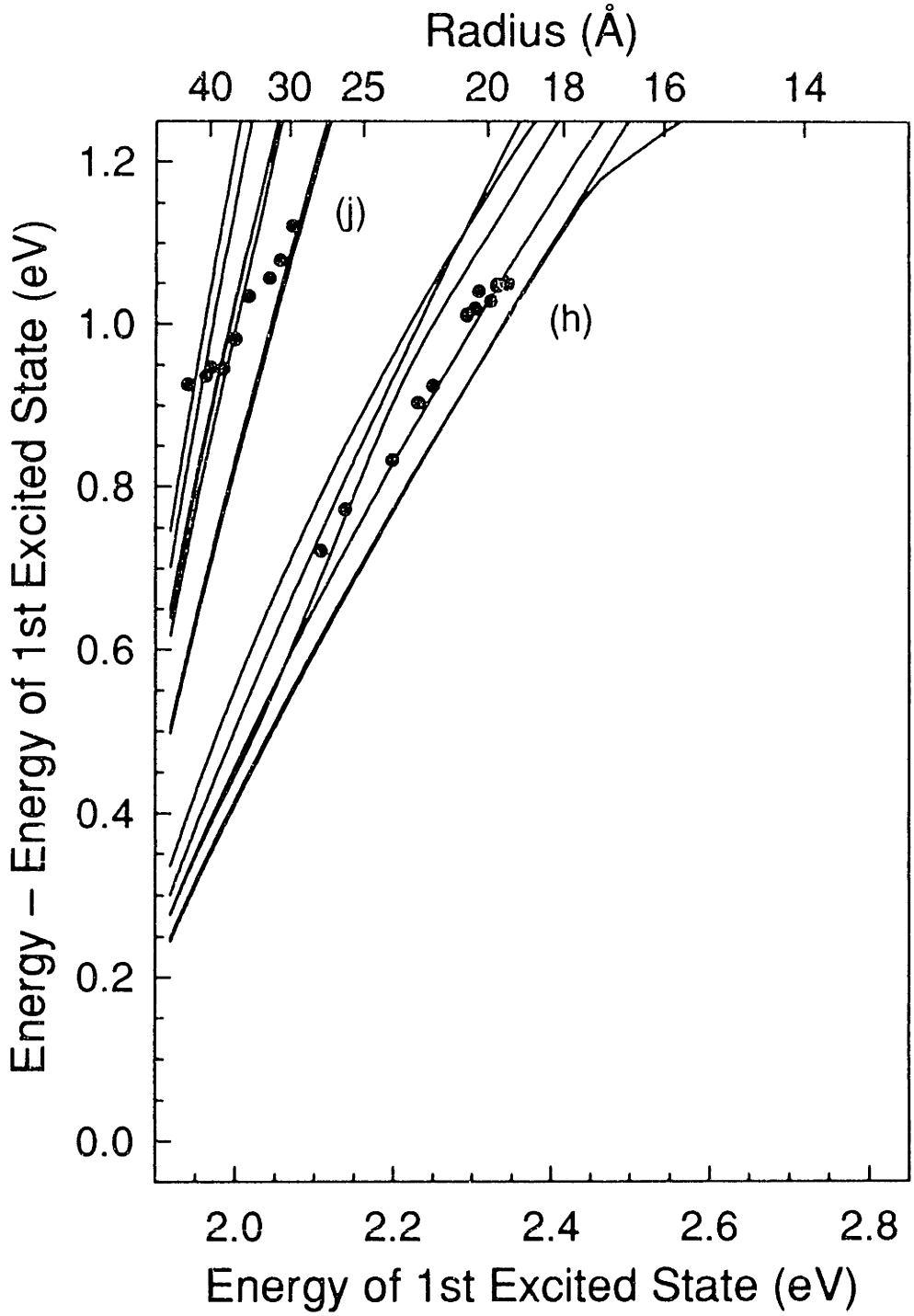

FIG. 3.12 Theoretically predicted pair states (solid lines) which are possible assignments for feature (h) [$1S_{1/2}1D_e$, $2S_{3/2}2S_e$, $1S_{3/2}2S_e$, $2S_{3/2}1D_e$, $1D_{5/2}1D_e$, and $4P_{3/2}1P_e$] and (j) [$2P^{\ell}_{1/2}2P_e$, $3S_{3/2}3S_e$, $2P_{3/2}2P_e$, $4P_{3/2}2P_e$, $2P_{5/2}2P_e$, $4P_{5/2}2P_e$, and $3S_{3/2}2D_e$] in Fig. 3.6. The experimental data is shown for comparison (circles).

The agreement between theory and data in Figs. 3.8-3.10 allows us to be confident in the assignment of the features discussed above ($1S_{3/2}1S_e$, $2S_{3/2}1S_e$, $1P_{3/2}1P_e$, $1S_{1/2}1S_e$, $2S_{1/2}1S_e$, and $3S_{1/2}1S_e$). The increasing density of allowed states at high confinement energy makes the remaining assignments more difficult. Figures 3.11 and 3.12 present possibilities for features (f), (h), (i), and (j) in Fig. 3.6. We assign (f) to $1P^{\ell}_{1/2}\,1P_e$ and/or $1P_{5/2}1P_e$ (Fig. 3.11). These transitions best reproduce the behavior of (f), which begins near the avoided crossing of $2S_{1/2}1S_e$ and $3S_{1/2}1S_e$. Figure 3.11 also shows the best assignments for feature (i): $1P^{so}_{1/2}\,1P_e$, $4S_{3/2}2S_e$, and/or $1S_{1/2}2S_e$. $1P^{so}_{1/2}\,1P_e$ shows the best agreement with the data, but all three transitions are expected to be strongly allowed. Figure 3.12 presents possible assignments for feature (h) [$1S_{1/2}1D_e$, $2S_{3/2}2S_e$, $1S_{3/2}2S_e$, $2S_{3/2}1D_e$, $1D_{5/2}1D_e$, and $4P_{3/2}1P_e$] and for feature (j) [$2P^{\ell}_{1/2}\,2P_e$, $3S_{3/2}3S_e$, $2P_{3/2}2P_e$, $4P_{3/2}2P_e$, $2P_{5/2}2P_e$, $4P_{5/2}2P_e$, and $3S_{3/2}2D_e$]. To assign features (h) or (j) to one of these states is impossible and potentially misleading since the eigenstates yielding (h) and (j) are likely to be mixtures of these states.

3.7 Additional Complications

Each theoretical pair state shown in Figs. 3.8-3.12 is a single, but highly degenerate, state. In reality the pair states are split by additional terms in the Hamiltonian which for simplicity are neglected by the model. These more subtle effects are commonly ignored because they are not necessary to explain most experimental results. It is however worthwhile to mention the assumptions and to consider their effect on theoretical predictions. While the model assumes that the dots are spherically shaped crystallites with cubic (zinc blende) lattice symmetry, structural studies show that the dots are slightly prolate (aspect ratio 1.0 to 1.3) with a hexagonal (wurtzite) crystal lattice.[15] These physical attributes partially lift the degeneracies.[49,50] In the bulk crystal the wurtzite modification causes a crystal field splitting between the light and heavy hole valence sub-bands at k=0, demonstrated in Fig. 3.13. The crystal field similarly splits quantum dot hole states.[49] For exar. ple, $1S_{3/2}$, which is a four-fold degenerate hole state in the cubic model, splits into doubly degenerate $1S_{3/2,\pm 3/2}$ and $1S_{3/2,\pm 1/2}$ sublevels, where the second subscript denotes the projection of F_h along the unique axis of the hexagonal lattice. A

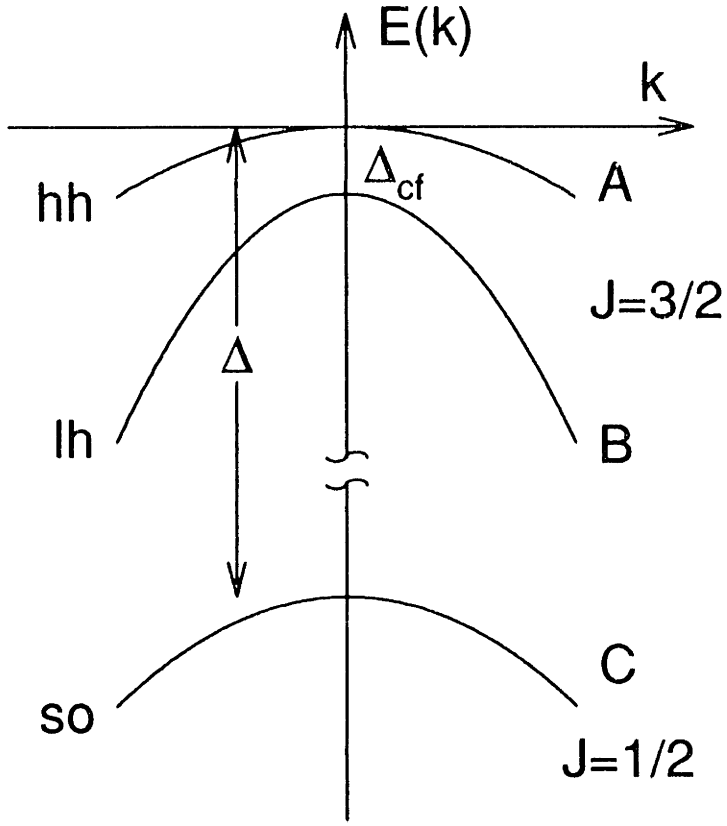

FIG. 3.13 Illustration of the bulk valence band for wurtzite (hexagonal) CdSe near k = 0. As in diamond-type semiconductors the valence band is split into heavy hole (hh), light hole (lh), and split off hole (so) sub-bands. Δ is the spin orbit coupling (0.42eV). However, due to the crystal field of the hexagonal lattice the heavy hole and light hole bands are split by Δ_{cf} at k = 0 (25 meV). Since the heavy hole and light hole bands are referred to as the A and B bands respectively, the crystal field splitting is sometimes called the "A-B splitting". A similar splitting is predicted for quantum dot hole states in wurtzite CdSe.

similar splitting occurs due to the nonspherical shape of the dots.[50] In prolate dots with β>0.14 this effect splits the states in the opposite direction from the crystal field splitting (or "A-B splitting").[50] We estimate that for one of our medium-sized samples (20Å radius) the splitting caused by the hexagonal lattice (~20meV) is diminished ~50% by the nonspherical shape.[49,50]

The exchange interaction between the electron and hole[23,51,52] and the Coulomb term[38,47] also affect the degeneracies. The exchange interaction splits the sublevels according to their total angular momentum, $N = F_h + F_e$. Due to this effect $1S_{3/2}1S_e$ should be split into $N = 2$ and $N = 1$ sublevels.[23,51,52] Although small in bulk CdSe excitons (0.13meV)[54] the exchange splitting has been predicted[23,51-53] to be important in quantum dots due to the increased overlap of the electron and hole. The Coulomb interaction[38,47] causes splittings by mixing sublevels which have the same N and the same projection, N_m. In states which contain $1S_e$, these splittings should be weak. For example in $1S_{3/2}1S_e$ each sublevel is uniquely described by its quantum numbers, N and N_m. Therefore intra-sublevel mixing does not occur in $1S_{3/2}1S_e$.[55] However, transitions with $L_e>0$, such as those which include $1P_e$, are further split by the Coulomb term. In the $1P_{3/2}1P_e$ multiplet two sublevels exist with $N = 2$ and two sublevels with $N = 1$. These levels are mixed and additional Coulomb splittings are expected.

In a treatment of the first excited state ($1S_{3/2}1S_e$) which includes the effect of hexagonal symmetry, nonspherical shape, and the exchange interaction, the initially eight-fold degenerate $1S_{3/2}1S_e$ state is split into five sublevels.[53] The sublevels are described by the projection quantum number N_m: one sublevel with $N_m=\pm2$, two with $N_m=\pm1$, and two with $N_m=0$. This fine structure implies that each transition shown in Figs. 3.9-3.12 is actually a multiplet of sublevels. Variations in sublevel spacings due to size, shape, and structure inhomogeneities along with broad sublevel linewidths may explain why the fine structure is generally not resolved.

Although it is not yet clear what role such splittings play in our experimental data, the multiplet structure may be important for two reasons. First, the multiplet splittings may explain the band edge structure observed in our PLE and TDA results. This possibility will be considered in chapters 4, 5, and 6. Secondly, the splittings may be responsible for some portion of the observed transition linewidths. The observation that linewidths increase with increasing energy, commonly explained by lifetime broadening, may result from the fact that higher transitions have higher angular momentum and may exhibit broader widths due to the increased complexity of their multiplets. In this case states with low angular momentum would be more likely to be resolved. For example, of the

two possible assignments shown in Fig. 3.11 for feature (f), $1P'_{1/2}1P_e$ is 12-fold degenerate before consideration of multiplet splittings while $1P_{5/2}1P_e$ is initially 36-fold degenerate. (For comparison the dominant $n_hS_{1/2}1S_e$ and $n_hS_{3/2}1S_e$ transitions are initially four-fold and eight-fold degenerate, respectively.) If both transitions have similar oscillator strength and if their multiplet width is proportional to their initial degeneracy, $1P'_{1/2}1P_e$ would ride above a much broader and unresolved $1P_{5/2}1P_e$. $1P'_{1/2}1P_e$ would then be responsible for feature (f). This description, in which high angular momentum transitions are concealed by overlapping low angular momentum states is also consistent with our fits (Fig. 3.5) which require an effective continuum (cubic background) to represent underlying transitions which are not resolved.

3.8 Conclusion

In this chapter we address one of the original and basic questions about quantum dots — how their electronic spectra evolve with size in the strong confinement regime. We present the size dependence of ten absorption features observed in CdSe quantum dots ranging from ~24Å to ~105Å in diameter. By comparing the experimental results with effective mass calculations, we find sufficient agreement between theory and experiment to confidently assign six transitions and present possible assignments for the remaining four. Avoided crossings in the $n_hS_{1/2}1S_e$ transitions, predicted by theory, are clearly present in our data and demonstrate the importance of valence band structure in the description of the quantum dot pair states. Quantitative differences between experiment and theory suggest that the model would be further improved by a more rigorous treatment of the Coulomb interaction. We also speculate about the influence of fine structure in our data which should occur due to more subtle effects ignored by the model.

3.9 References

1. Al. L. Efros and A. L. Efros, Fiz. Tekh. Poluprovdn. **16**, 1209 (1982) [Sov. Phys. Semicond. **16**, 772 (1982)].
2. L. E. Brus, J. Chem. Phys. **80**, 4403 (1984).
3. A. I. Ekimov, Al. L. Efros and A. A. Onushchenko, Solid State Commun. **56**, 921 (1985).
4. A. I. Ekimov and A. A. Onushchenko, Pis'ma Zh. Eksp. Teor. Fiz. **40**, 337 (1984) [JETP Lett. **40**, 1136 (1984)].

5. R. Rossetti, R. Hull, J. M. Gibson and L. E. Brus, J. Chem. Phys. **82**, 552 (1985).
6. A. I. Ekimov, A. A. Onushchenko and Al. L. Efros, Pis'ma Zh. Eksp. Teor. Fiz. **43**, 292 (1986) [JETP Lett. **43**, 376 (1986)].
7. N. Chestnoy, R. Hull and L. E. Brus, J. Chem. Phys. **85**, 2237 (1986).
8. A. P. Alivisatos, A. L. Harris, N. J. Levinos, M. L. Steigerwald, and L. E. Brus, J. Chem. Phys. **89**, 4001 (1988).
9. A. I. Ekimov, Al. L. Efros, M. G. Ivanov, A. A. Onushchenko and S. K. Shumilov, Solid State Commun. **69**, 565 (1989).
10. Y. Wang and N. Herron, Phys. Rev. B **42**, 7253 (1990).
11. M. G. Bawendi, W. L. Wilson, L. Rothberg, P. J. Carroll, T. M. Jedju, M. L. Steigerwald and L. E. Brus, Phys. Rev. Lett. **65**, 1623 (1990).
12. N. Peyghambarian, B. Fluegel, D. Hulin, A. Migus, M. Joffre, A. Antonetti, S. W. Koch and M. Lindberg, IEEE J. Quantum Electron. **25**, 2516 (1989).
13. V. Esch, B. Fluegel, G. Khitrova, H. M. Gibbs, X. Jiajin, K. Kang, S. W. Koch, L. C. Liu, S. H. Risbud and N. Peyghambarian, Phys. Rev. B **42**, 7450 (1990).
14. A. I. Ekimov, F. Hache, M. C. Schanne-Klein, D. Ricard, C. Flytzanis, I. A. Kudryavtsev, T. V. Yazeva, A. V. Rodina and Al. L. Efros, J. Opt. Soc. Am. B **10**, 100 (1993).
15. C. B. Murray, D. J. Norris and M. G. Bawendi, J. Am. Chem. Soc. **115**, 8706 (1993).
16. D. J. Norris, A. Sacra, C. B. Murray and M. G. Bawendi, Phys. Rev. Lett. **72**, 2612 (1994).
17. D. J. Norris, M. Nirmal, C. B. Murray, A. Sacra and M. G. Bawendi, Z. Phys. D **26**, 355 (1993).
18. M. Nirmal, C. B. Murray and M. G. Bawendi, Phys. Rev. B **50**, 2293 (1994).
19. W. Hoheisel, V. L. Colvin, C. S. Johnson, and A. P. Alivisatos, J. Chem. Phys **101**, 8455 (1994).
20. C. R. M. de Oliveira, A. M. de Paula, F. O. Plentz Filho, J. A. Medeiros Neto, L. C. Barbosa, O. L. Alves, E. A. Menezes, J. M. M. Rios, H. L. Fragnito, C. H. Brito Cruz, and C. L. Cesar, Appl. Phys. Lett. **66**, 439 (1995).
21. P. A. M. Rodrigues, G. Tamulaitis, P. Y. Yu, and S. H. Risbud, Solid State Commun. **94**, 583 (1995).
22. D. J. Norris and M. G. Bawendi, J. Chem. Phys. (in press).
23. M. Chamarro, C. Gourdon, P. Lavallard and A. I. Ekimov, Jpn. J. Appl. Phys. **34**, Suppl. 34-1, 12 (1995).
24. The bulk exciton Bohr radius in CdSe is 56Å.
25. L. R. Becerra, C. B. Murray, R. G. Griffin and M. G. Bawendi, J. Chem. Phys. **100**, 3297 (1994).
26. J. E. Bowen Katari, V. L. Colvin and A. P. Alivisatos, J. Phys. Chem. **98**, 4109 (1994).
27. Sizes reported are estimated from extensive size dependent transmission electron microscopy (TEM) and small angle X-ray measurements and are based on the energy of the first absorption peak.
28. C. B. Murray and M. G. Bawendi (unpublished).
29. W. H. Press, B. P. Flannery, S. A. Teukolsky, and W. T. Vetterling, *Numerical Recipes in C* (Cambridge University Press, Cambridge, 1988), Chapter 14.
30. C. Kittel, *Quantum Theory of Solids* (John Wiley & Sons, New York, 1987), Chapter 14.
31. R. H. Parmenter, Phys. Rev. **100**, 573 (1955).
32. G. Dresselhaus, Phys. Rev. **100**, 580 (1955).
33. E. O. Kane, J. Phys. Chem. Solids **1**, 249 (1957).
34. J. B. Xia, Phys. Rev. B **40**, 8500 (1989).
35. G. B. Grigoryan, E. M. Kazaryan, Al. L. Efros and T. V. Yazeva, Fiz. Tverd. Tela **32**, 1772 (1990) [Sov. Phys. Solid State **32**, 1031 (1990)].
36. K. J. Vahala and P. C. Sercel, Phys. Rev. Lett. **65**, 239 (1990).
37. P. C. Sercel and K. J. Vahala, Phys. Rev. B **42**, 3690 (1990).
38. S. W. Koch, Y. Z. Hu, B. Fluegel and N. Peyghambarian, J. Crystal Growth **117**, 592 (1992).
39. J. M. Luttinger and W. Kohn, Phys. Rev. **97**, 869 (1955).
40. J. M. Luttinger, Phys. Rev. **102**, 1030 (1956).
41. A. Baldereschi and N. O. Lipari, Phys. Rev. B **8**, 2697 (1973).
42. In the spherical band approximation, outlined in Ref. 41 for the charged impurity problem, only terms of spherical symmetry in the Luttinger Hamiltonian are considered in first order. Cubic "warping" terms are neglected but may be added as a small perturbation.

43. C. R. Pidgeon and R. N. Brown, Phys. Rev. **146**, 575 (1966).
44. D. B. Tran Thoai, Y. Z. Hu, and S. W. Koch, Phys. Rev. B **42**, 11261 (1990).
45. Al. L. Efros, personal communication.
46. R. L. Aggarwal, in *Semiconductors and Semimetals*, R. K. Willardson and A. C. Beer, eds. (Academic Press, New York, 1972), Vol. 9, p. 151.
47. Y. Z. Hu, M. Lindberg and S. W. Koch, Phys. Rev. B **42**, 1713 (1990).
48. *Landolt-Bornstein Numerical Data and Functional Relationships in Science and Technology*, New Series, Group III, Vol. 17b, edited by K. H. Hellwege (Springer-Verlag, Berlin, 1982).
49. Al. L. Efros, Phys. Rev. B **46**, 7448 (1992).
50. Al. L. Efros and A. V. Rodina, Phys. Rev. B **47**, 10005 (1993).
51. S. Nomura, Y. Segawa and T. Kobayashi, Phys. Rev. B **49**, 13571 (1994).
52. T. Takagahara, Phys. Rev. B **47**, 4569 (1993).
53. Al. L. Efros, M. Rosen, M. Kuno, M. Nirmal, D. J. Norris, and M. G. Bawendi (in preparation).
54. V. P. Kochereshko, G. V. Mikhailov, and I. N. Ural'tsev, Fiz. Tverd. Tela **25**, 769 (1983) [Sov. Phys. Solid State **25**, 439 (1983)].
55. The $1S_{3/2}1S_e$ sublevels should be split by mixing with nearby states, such as $2S_{3/2}1S_e$, but this effect should be weaker.

Section III
Exciton Fine Structure

Chapter 4

Structure in the Lowest Absorption Feature: Exciton Fine Structure or Surface States?*

4.1 Introduction

Nanometer size semiconductor crystallites, or quantum dots, exhibit electronic properties dramatically different from bulk semiconductors. They fall in a size regime intermediate between molecular and bulk behavior and provide an opportunity to investigate the evolution of semiconductor properties with size. When quantum dots are small compared to the natural length scale of the electron-hole pair, the exciton Bohr radius, their electronic wavefunctions experience three dimensional quantum confinement due to the dot boundary.[1,2] This confinement induces quantization of the bulk electronic bands so that quantum dots have discrete electronic transitions that shift to higher energies with decreasing size. Numerous optical studies[5-27] on II-VI semiconductor quantum dots, such as CdS and CdSe, have confirmed these characteristics and revealed much information about the absorbing and emitting states. Many models have been presented which describe, at least qualitatively, their fundamental photophysics. However, most use two different mechanisms to explain their absorption and emission behavior. While their emission is attributed to surface-localized trap states,[5-9] their absorption is described by solid state theories[27-32] which completely ignore the surface.

To combine these ideas a simple quantum dot model has been proposed[8] in which two classes of electronic states exist: "core" states, with the electron and hole delocalized within and confined by the dot boundary, and surface states, with one or both of the carriers localized at or near the dot/matrix interface. (In this model the true eigenstates may be linear combinations of core and surface components.[8]) Since luminescence from core states should exhibit a ~1ns lifetime as in bulk II-VI semiconductors,[3] surface traps

---

* Much of chapter 4 will appear in print: D. J. Norris and M. G. Bawendi, J. Chem. Phys. (in press).

were proposed to explain the extremely long radiative lifetime of II-VI quantum dots (~1μs at 10K).[5-9] These states have been attributed to surface polarization,[4] interface "roughness",[9] or the dot analog of bulk surface bands.[8] However, while recent quantum dot emission studies[5-9,18] use surface states to explain the experimental results, the data are also consistent with newer models which ignore surface effects. Solid state theories which explain quantum dot absorption properties[27-32] can now also rationalize emission behavior based solely on core effects.[33-38] These core models predict that the lowest excited core state is optically forbidden, implying that relaxation back to the ground state from this level should be inefficient and slow.

In this chapter we examine the competing surface and core models by investigating quantum dot absorption around the HOMO-LUMO transition (or "band edge" in solid state terminology). We study high quality CdSe quantum dots which have recently been used to observe and assign the quantum dot spectrum as a function of size (see chapters 2 and 3).[22,23] To reduce residual sample inhomogeneities such as size, shape, and structural distributions which conceal spectroscopic details we use transient differential absorption (TDA) spectroscopy.[10-22] This technique measures the absorption change induced by a spectrally narrow pump beam. TDA spectra (pump off minus pump on) contain both bleached transitions and induced absorptions arising from dots optically excited by the pump. Since only a small subset of the sample distribution is excited, the data reveal absorption information with inhomogeneous broadening greatly reduced.

Previous work has shown that quantum dot TDA results are strongly dependent on the method of dot preparation.[10-22] Until recently all dots grown in doped silicate glasses showed broad bleaches [full width at half maximum (FWHM) ~100meV][11-16] while dots grown by wet chemical synthesis, which we refer to as "colloid" samples, exhibited a narrow bleach (~20meV).[17,21] More recent samples, carefully prepared doped glasses[19,20] as well as our colloidal samples,[18,22] have both a narrow and broad bleach component. Due to the similar behavior of these samples, which seems to be independent of the method of preparation, as well as the steady improvement in sample quality in recent years, these newer samples should better reflect intrinsic quantum dot absorption properties. Here we investigate the narrow and broad bleach components observed in

these samples and discuss their band edge absorption in the context of the two proposed (surface and core) models discussed above. We find that our results are more consistent with the recently proposed core models.[33-38] In addition, our results explain the large "Stokes" shift observed in the inhomogeneous luminescence of CdSe quantum dots which is inconsistent with previous models.[27]

4.2 Experimental

We prepare CdSe quantum dots according to the method of Ref. 39. In this procedure the wet chemical synthesis is followed by size-selective precipitation to further diminish the size distribution. Highly monodisperse (<4% rms) samples are obtained which contain slightly prolate (aspect ratio 1.0 to 1.3), near defect-free, wurtzite crystallites with well passivated surfaces.[39-41] The dots exhibit strong band edge luminescence with a quantum yield (at 10K) greater than 0.1 and measured as high as 0.9. The intensity of deep trap emission, which dominates the luminescence behavior of dots prepared by many other methods, is size-dependent in our samples. Negligible in our largest dots, it slowly increases with decreasing size and becomes significant only in our smallest size samples.

We investigate two different size CdSe samples: A) ~56Å and B) ~35Å diameter.[42] While we focus on these samples, measurements have been performed on a much larger (>12) sample series. The results reported are representative of the complete data set and are highly reproducible. The dots were isolated and redispersed in tri-n-butyl-phospine with *o*-terphenyl added (200mg/ml) to form an optically clear organic glass at cryogenic temperatures. We have also performed measurements on dots embedded in PVB polymer films (see chapter 2) and find that the specific choice of matrix (organic glass or polymer) has negligible effect on our results. The samples are placed between sapphire flats separated by a 0.5mm thick Teflon spacer and mounted in a helium cryostat. All spectra are obtained at 10K.

The experimental apparatus used to measure absorption and TDA spectra is similar to that shown in chapter 2 (Fig. 2.2). For absorption, a spectrally broad probe pulse is produced by exciting a mixture of several laser dyes with the third harmonic of a 50Hz Q-

switched Nd:YAG laser (Continuum NY60-50) with ~7ns pulses. After focusing the dye emission onto the sample, the transmitted light is dispersed by a 0.25m spectrometer (Aries FF250) and detected with a 5ns-gated optical multichannel analyzer, or OMA (Princeton Instruments IRY-700G).

TDA spectra are obtained by comparing transmitted probe light, measured as in absorption, with and without the application of a spectrally narrow pump pulse. The pump beam is produced by a diode-pumped, Q-switched Nd:YLF/dye laser system (Spectra-Physics TFR-5230) with ~7ns pulses. The intensity of the pump beam was carefully controlled to ensure linear absorption, checked via luminescence. Both pump and probe lasers are electronically synchronized with a digital pulse generator (Stanford Research Systems DG535) to allow control of pulse timing. In a typical experiment the pump pulse arrives at the sample ~30ns before the probe pulse to ensure that no scattered pump light is observed by the gated detector. The experimental repetition rate, 50Hz, allows the samples to completely recover between successive pulses. Pump induced emission collected with the transmitted probe beam is corrected for by separately measuring the signal caused by the pump beam by itself and subtracting it from the pump-probe signal.

Gated photoluminescence is measured using the TDA apparatus described above without the probe beam. We record cw photoluminescence (PL) and photoluminescence excitation (PLE) using a commercial spectrofluorometer (SPEX Fluorolog-2). This instrument consists of two double (0.22m) spectrometers. The first selects the desired excitation wavelength from the emission of a xenon arc lamp. The second chooses the emission wavelength detected by a photomultiplier tube (R928).

4.3 Observations

Typical results for our quantum dots are shown in Fig. 4.1. Four electronic transitions are resolved in the low temperature absorption spectrum of sample A (Fig. 4.1a). These transitions (as well as two more at higher energy not shown in Fig. 4.1) are discussed and assigned in our size-dependent studies (see chapters 2 and 3).[22,23] Figure

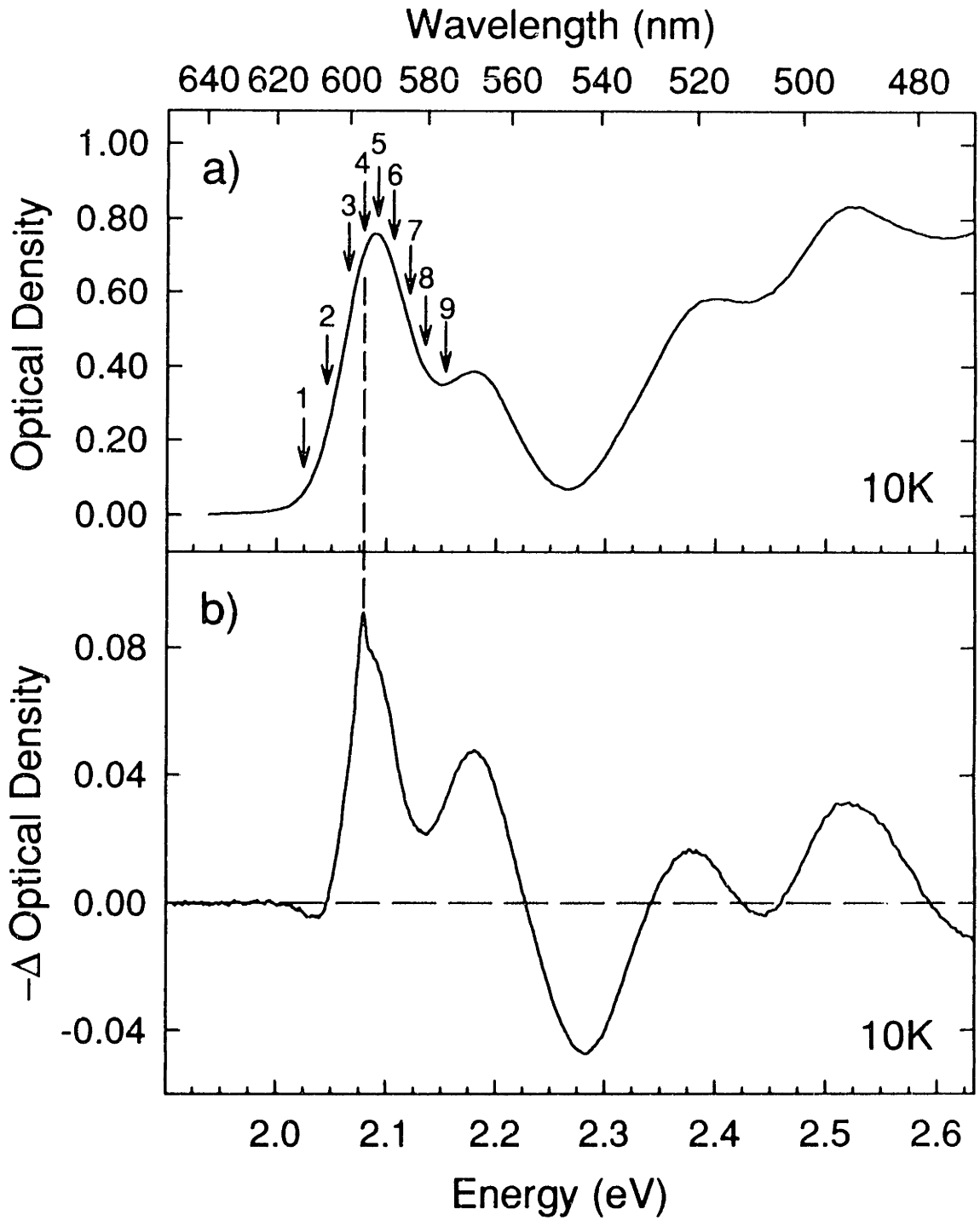

FIG. 4.1 (a) Absorption spectrum for sample A. The numbered arrows denote the pump positions used in the TDA results of Figs. 4.2 and 4.3. The pump energies are: 2.024, 2.045, 2.065, 2.079, 2.092, 2.106, 2.121, 2.135, and 2.154 eV (for curves 1 to 9). (b) A typical TDA spectrum for sample A (arrow 4) plotted as negative change in optical density. Positive (negative) peaks are bleaches (induced absorptions).

4.1b presents the TDA spectrum when the pump energy is just below the first absorption peak (arrow 4). The shape is nearly identical to the TDA results of Ref. 18. Bleaches appear at the position of ground state absorptions while induced absorptions occur below (at 2.03eV), between (at 2.28 and 2.45eV), and above (>2.6eV) these features. Although the transitions are more clearly resolved in the TDA spectrum (Fig. 4.1b) than in the absorption spectrum (Fig. 4.1a), the majority of the features remain relatively broad and comparable in linewidth to bleaches observed in most doped glass samples.[11-16] In addition, however, a single narrow bleach occurs at the pump energy. This feature, which is not an artifact caused by scattered pump light,[43] is similar in width (6.5meV, FWHM) to those reported for early colloidal particles exhibiting a narrow bleach.[17,21] (Below we consistently use the terms "broad" and "narrow" to distinguish linewidths of order 50meV from those of order 5meV.) Our samples, therefore, exhibit bleaches at the band edge which have both a broad and a narrow component.

Figure 4.2 shows a series of TDA spectra for sample A obtained with the pump positions from Fig. 4.1a (arrows 1-9). Figure 4.3 presents the same data obtained with higher (4x) spectral resolution. While the data are normalized for comparison in both figures, on an absolute scale the bleach intensity rapidly decreases as the pump is tuned red. The bleach intensity in curve 1 is nearly an order of magnitude less than curve 4. Figures 4.2 and 4.3 show that the narrow feature follows the pump energy and rides over the broad bleach. In addition the ratio of the narrow to broad bleach decreases as the pump is tuned to higher energy. The narrow bleach, which is clearly visible in curves 1-4 of Fig. 4.3, almost vanishes when the pump is above the first absorption maximum (Fig. 4.3, curves 6-8).

Figure 4.4 compares high resolution TDA and gated emission spectra obtained with identical pump energies (arrow 1 from Fig. 4.1a) for sample A. While broad inhomogeneous band edge emission (which we refer to as "full luminescence") is observed when our samples are excited well above their first transition, excitation on the red tail of the first absorption feature optically selects a subset of the dot distribution. The resulting fluorescence line narrowed (FLN) spectrum reveals a vibrational (longitudinal optical

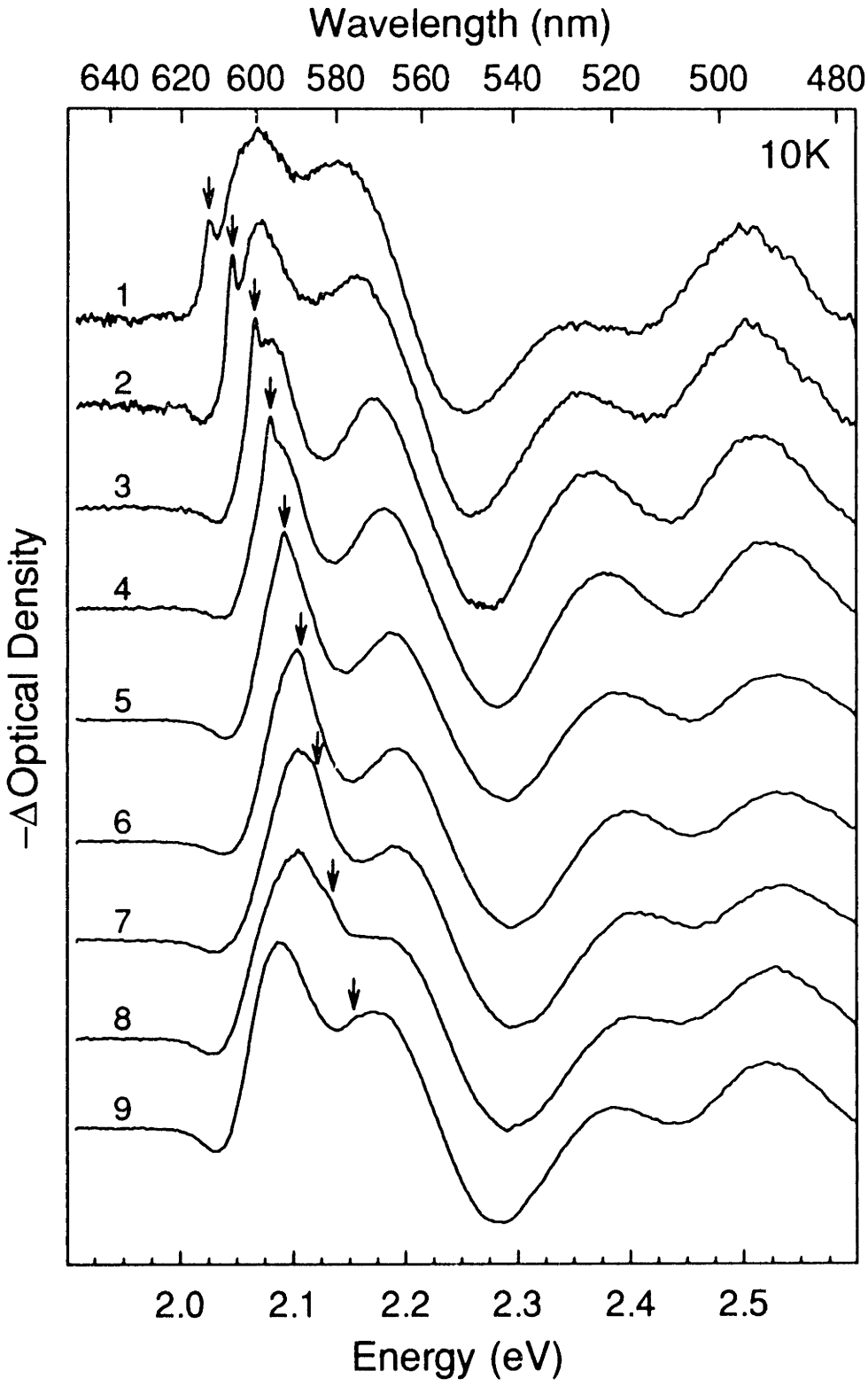

FIG. 4.2 Normalized TDA spectra for sample A as a function of pump energy. The numbers and arrows refer to the pump positions shown in Fig. 4.1.

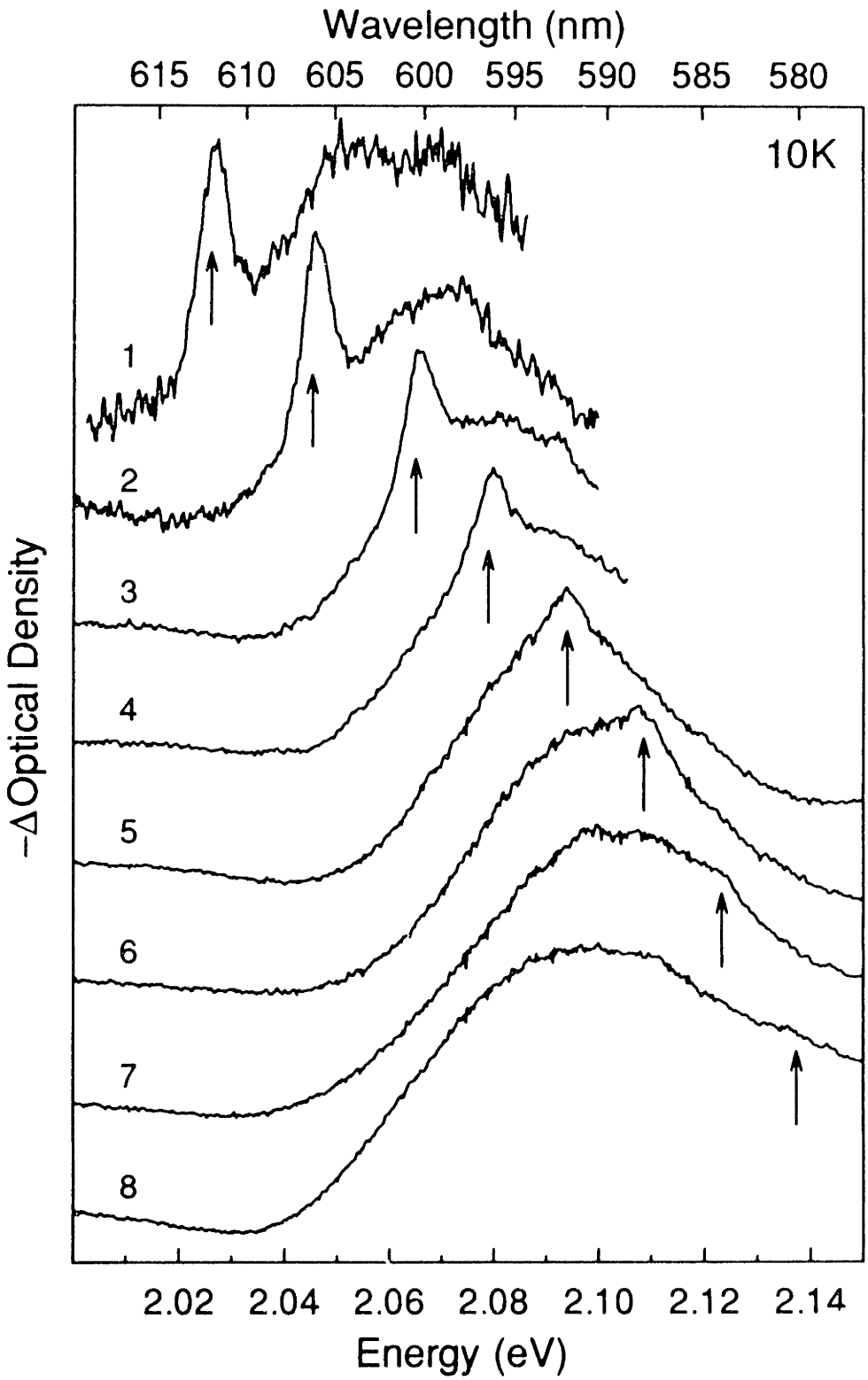

FIG. 4.3 Normalized TDA spectra for sample A as in Fig. 4.2 obtained with four times higher spectral resolution.

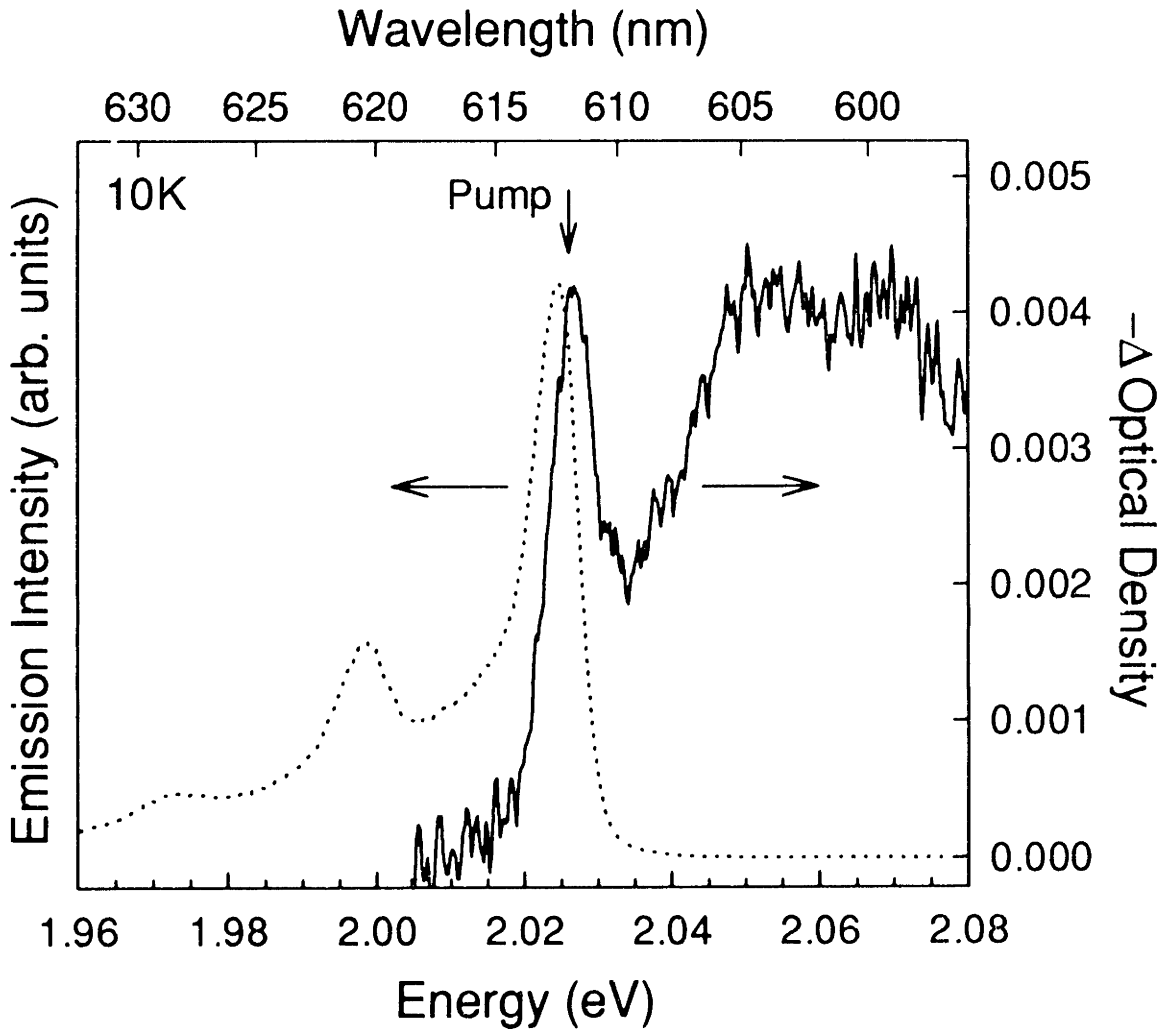

FIG. 4.4 A comparison of gated FLN emission (dotted line) and the TDA spectrum (solid line) for sample A using pump position 1 of Fig 4.1a. Longitudinal optical (LO) phonon replicas are observed in the FLN data.

[LO] phonon) progression of narrow emission lines,[8,9,18] as seen in Fig. 4.4. Since these lines decay with a time constant of several hundred nanoseconds[9,44] and imply electron-phonon coupling larger than that predicted for quantum dot core states[45,46] they have previously been assigned to emission from shallow surface traps.[8,9,18] Figure 4.4 demonstrates the strong similarity between the first emission line in FLN (the zero-LO-phonon line) and the narrow bleach feature. Both have identical linewidths and appear nearly resonant with the pump energy. The discrepancy in their positions is due to a small Stokes shift observed in emission. The similar behavior of these two lines is not peculiar to this sample. Their linewidths increase together with decreasing dot size, as discussed in chapter 5.[21]

The structure observed in the bleach is also observed in photoluminescence excitation (PLE) results, as demonstrated in Fig. 4.5 for sample B. To obtain the PLE spectrum we monitor a narrow spectral band on the blue edge of the full luminescence (arrow in Fig. 4.5c) while scanning the excitation energy (see chapters 3 and 6). PLE, like TDA, measures a subset of the full sample distribution and quantum dot features observed in absorption are more clearly resolved with this technique.[18,22-24] However, since PLE spectra are obtained via luminescence, TDA and PLE yield slightly different and complementary information. PLE provides an alternative method to check our TDA results.

Figure 4.5 compares a PLE spectrum (Fig. 4.5c) with absorption (Fig. 4.5a) and TDA (Fig. 4.5b) results for sample B. As in TDA, the PLE spectrum exhibits both narrow (α, α') and broad (β) components in the band edge absorption. The relative intensity of the narrow to broad lines is also comparable to the TDA results. However, unlike the TDA results where only one narrow feature is resolved, two narrow lines (α, α') are present in Fig. 4.5c. The second feature, α', which is separated from α by the LO-phonon frequency ($210cm^{-1}$),[47] appears due to electron-phonon coupling. Since phonon replicas are not clearly resolved in the TDA spectra, LO-phonon coupling in absorption is expected to be weak. Instead, α' appears mainly due to the strong coupling observed in FLN emission. As demonstrated in Fig. 4.4, the narrow absorption line seen in the TDA

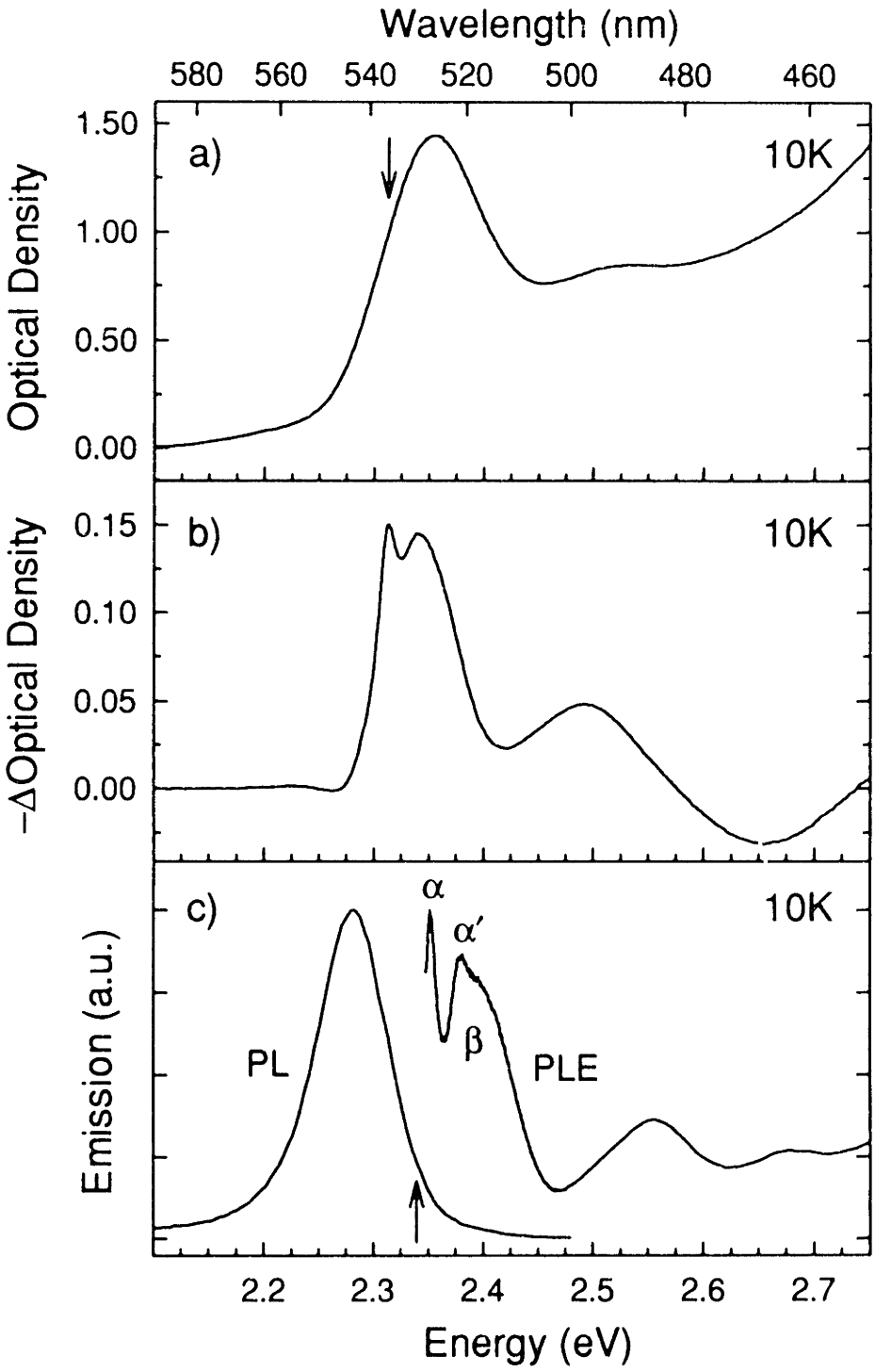

FIG. 4.5 a) Absorption spectrum for sample B. The arrow marks the pump position used in b. b) TDA spectrum for sample B. c) Full luminescence and PLE spectra for sample B. In luminescence the sample was excited at 2.655eV. PLE emission was monitored at 2.339eV (arrow) with a ~1meV bandpass. Both narrow (α, α′) and broad (β) PLE features are observed.

spectrum produces a series of emission lines. In PLE these two effects are combined so that a replica (α') of the narrow absorption line (α) occurs. In Fig. 4.5c α (α') is due to dots which emit from the zero- (one-) LO-phonon line.

4.4 "Single Dot" Absorption Lineshape

The pump-induced bleach spectrum, $-\Delta OD$, can be simulated as a function of frequency, ν, by evaluating

$$-\Delta OD(\nu) = C \int_{-\infty}^{\infty} A(\nu - \nu') \left\{1 - S(\nu_{pump} - \nu')\right\} D(\nu' - \nu_0)\, d\nu', \qquad (4.1)$$

where $A(\nu - \nu')$ represents a dimensionless "single dot" lineshape function[48] centered at ν', $S(\nu_{pump} - \nu')$ is a frequency-dependent "saturation factor" which accounts for the decrease in absorption due to the pump, and $D(\nu' - \nu_0)$ represents an inhomogeneous distribution centered at ν_0. C is a scaling factor of the appropriate units. We assume that S has the form[49]

$$S(\nu_{pump} - \nu') = \frac{1}{1 + I_R\, A(\nu_{pump} - \nu')}, \qquad (4.2)$$

where I_R is the ratio of the pump intensity (I_{pump}) to the saturation intensity (I_{sat}), and that D is normalized,

$$\int_{-\infty}^{\infty} D(\nu' - \nu_0)\, d\nu' = 1. \qquad (4.3)$$

We also assume in our calculations that both D and A are Gaussian. Equation (4.1) reduces to that used in Ref. 17 when $I_{pump} << I_{sat}$.

We model the band edge absorption behavior of sample A using Eq. (4.1). We simultaneously fit the TDA results (Fig. 4.3) and the absorption spectrum (Fig. 4.1a) using standard nonlinear least squares methods[50] to obtain the single dot absorption shown in Fig. 4.6b. The lowest two features in this lineshape, one narrow (FWHM 4.1meV, labeled 1 in Fig. 4.6b) and one broad (FWHM 33meV, labeled 2) are the band edge features of interest. Due to the sample distribution (D) they combine to form the first peak in absorption, as shown in the simulated absorption spectrum (Fig. 4.6a). A third line (FWHM 82meV, labeled 3 in Fig. 4.6b) is included in the model lineshape simply to

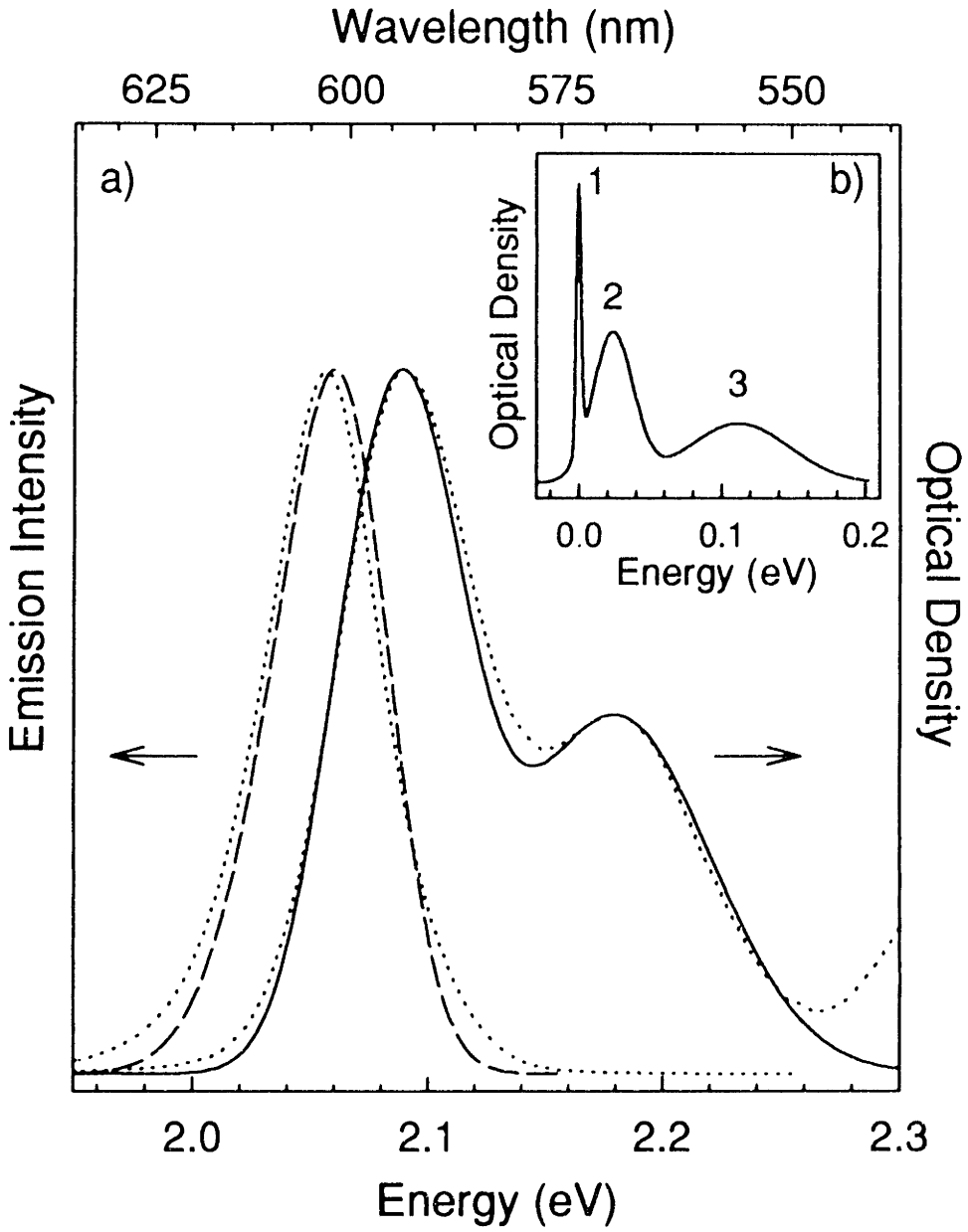

FIG. 4.6 (a) Simulated absorption (solid line) and full luminescence (dashed line) spectra for sample A. The experimental absorption and emission (dotted lines) are shown for comparison. To simulate the luminescence we assume that all emission comes from a vibrational progression of narrow lines like those in Fig. 4.4. A 31meV (33meV) shift exists between the simulated (experimental) luminescence and absorption. (b) The "single dot" absorption lineshape for sample A used in our simulations. The energy scale is relative to the center of feature 1 (FWHM 4.1meV). Features 2 (FWHM 34meV) and 3 (FWHM 82meV) are 24meV and 112meV higher in energy, respectively. The relative oscillator strength of features 2 and 3 are each ~4.6 times greater than feature 1.

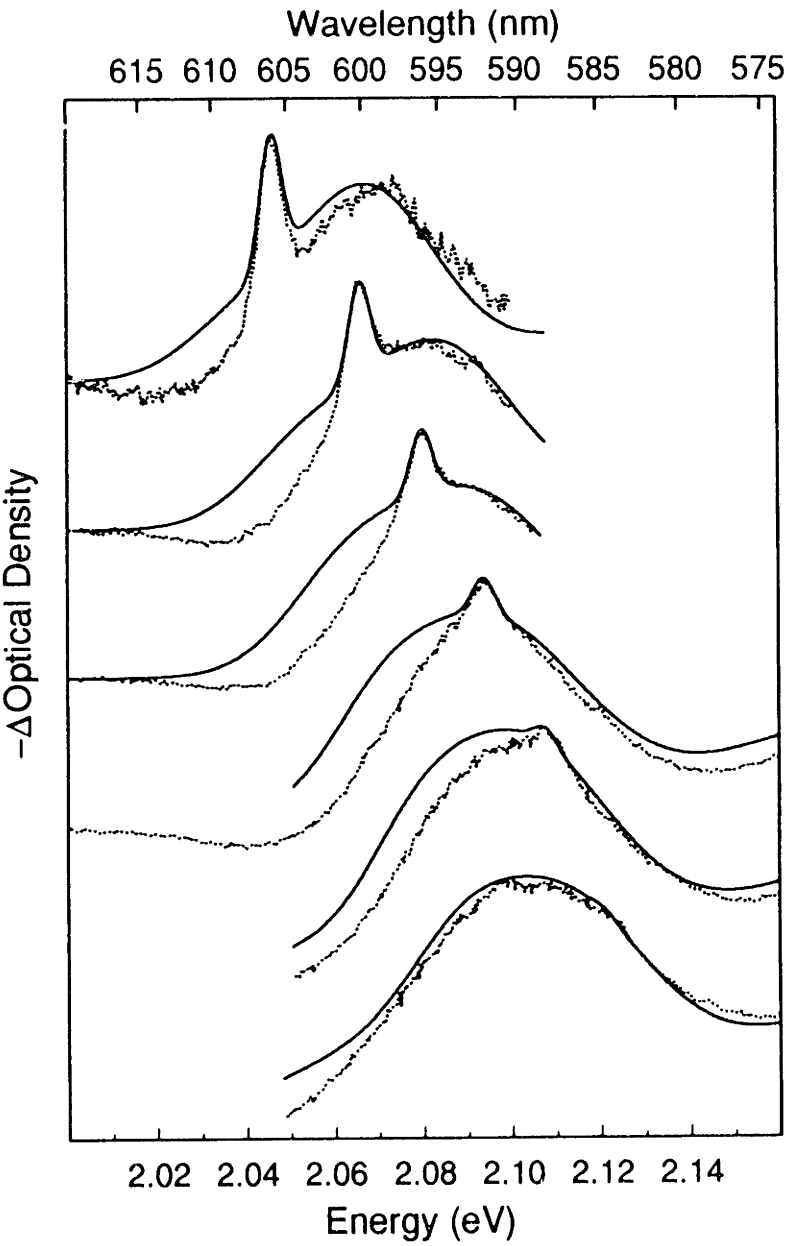

FIG. 4.7 Simulated TDA spectra (solid lines) and experimental results (dotted lines), normalized for comparison. Deviations on the red edge of the spectra are caused by an induced absorption not included in our model. The pump intensity is assumed to be well below saturation ($I_R \ll 1$). Our model includes nine adjustable parameters. Seven describe the three Gaussians in the single dot lineshape (three for linewidths, two for relative positions, and two for relative intensities; see Fig. 4.6b). Two describe the distribution function D (FWHM 47meV, center 2.068eV). The width of D corresponds roughly to a 4% standard deviation in dot diameter, consistent with TEM measurements ($\sigma \sim 4\%$) on samples of similar quality.

represent the second peak in absorption ($2S_{3/2}1S_e$) and will not be discussed further. With these features the entire TDA data set from Fig. 4.3 is reproduced including the disappearance of the narrow bleach with increasing energy, as demonstrated in Fig. 4.7. Deviation from experiment at lower energies occurs due to an induced absorption in this region ignored by the model.

In addition to the agreement in Fig. 4.7, the lineshape in Fig. 4.6b is strongly supported by its ability to reproduce the large "Stokes" shift in full luminescence. Although, as seen in Fig. 4.4, a small shift (2meV) is observed between the pump energy and the first narrow emission line in FLN, a much larger shift (33meV) is observed between the full luminescence and the first absorption feature (dashed lines in Fig. 4.6a). This large shift cannot be explained by the inhomogeneous sample distribution or the phonon progression in FLN emission.[27] It can be explained, however, with the single dot lineshape in Fig. 4.6b. We assume that emission occurs 2meV below the narrow absorption feature, as required by Fig. 4.4. Since most of the band edge absorption originates in the broad absorption feature (2), the large shift seen in full luminescence is caused by relaxation of the excitation from the broad absorption line to the narrow emission feature. The much smaller shift observed in FLN (Fig. 4.4) is from dots which are directly excited into their narrow absorption feature (1). To test this picture Fig. 4.6a compares the simulated full luminescence with experimental data. Since our global fitting procedure did not use luminescence to adjust the lineshape in Fig. 4.6b, this comparison is an independent check. The agreement in the large "Stokes" shift, 31meV (simulation) vs. 33meV (data), strongly supports our model lineshape.

We stress that, regardless of how the narrow and broad portions of the lineshape in Fig. 4.6b are assigned, this type of absorption best fits the data. We have tried many possibilities and always return to this shape. Reference 18 used LO phonon replicas to explain the shape of TDA spectra similar to that of Fig. 4.1b. Reference 22 speculated that a low energy "tail" due to surface states was responsible. We find that these explanations cannot account for our more complete data set and must therefore be revised.

4.5 Implications of the Lineshape

To explain the anomalous emission behavior of II-VI quantum dots, surface models[5-9] assume that dots absorb directly into core states (or states with mostly core character) and then relax rapidly into surface states. In these models the narrow FLN emission lines represent direct observation of surface state emission.[8] Our present data (Fig. 4.4) suggest that these FLN emission lines and the narrow bleach feature are closely related. If the narrow bleach feature is assigned to a core absorption while the narrow FLN emission lines are attributed to a surface state, as previously assumed, it is difficult to understand their strong similarities. It is more reasonable in the surface model to assign the narrow bleach feature (1 in Fig. 4.6b) to the same surface state observed in FLN emission. The broad feature (2 in Fig. 4.6b) may then be assigned to the lowest core absorption.

The narrow bleach then signifies surface state absorption. The long lifetime of the surface state, required to explain the emission results, implies that this state has very little oscillator strength. However, the narrow feature is clearly observed in the TDA spectra. In the model lineshape (Fig. 4.6b) it is quite strong, containing roughly one fifth of the total band edge (features 1 and 2) oscillator strength. Therefore, our data and the surface model appear to be in contradiction. While Fig. 4.4 implies that the narrow bleach is a surface state absorption, this feature absorbs much too strongly to be the long lived emitting state.

One possible explanation for this inconsistency is that, due to relaxation of the excitation after the absorption event, the initially excited surface state localizes further. Emission from the same state could be less efficient due to the decreased overlap of the carriers. Such a relaxation could explain the long emission lifetime as well as the Stokes shift observed in FLN emission (Fig. 4.4). However, it is unlikely that the dramatic change in localization required to explain the large decrease in oscillator strength would lead to such a small Stokes shift (~2meV). Therefore, we dismiss this explanation.

Another possibility is that due to differences in the bleaching mechanism the TDA experiment overestimates the relative strength of the surface state absorption. For example, if the narrow bleach were caused by the occupation of the surface state (state filling) while the broad bleaches were caused by the trapped carrier induced Stark effect

(see chapter 2),[10,22] the surface state may appear too large since state filling should be a more efficient bleaching mechanism than the Stark field. However, since PLE spectra (Fig. 4.5) which are independent of the bleaching mechanism clearly show narrow absorption features with intensities similar to the TDA results, we must conclude that this explanation is also incorrect.

Instead, we argue that the problem lies with the surface model itself, i.e. the assumption that the narrow FLN emission lines are due to surface states. While it is reasonable that the surface influences quantum dot optical behavior, the proposed band edge surface states appear inconsistent with our data. Therefore, an alternate description must be found to explain the long emission lifetime and the strong LO-phonon coupling observed in FLN emission.

Quantum dot core models have recently been proposed[33-38] which may provide this description. These models can rationalize the anomalous emission behavior using only core effects. They are based upon bulk effective mass theories which quantitatively describe quantum dot absorption behavior.[22,23,27] Previously, such theories have neglected subtle terms in the Hamiltonian which were unnecessary to explain the absorption data. In this case theory predicts that each quantum dot level is highly degenerate. However, when a more realistic Hamiltonian is considered each excited state is split into a multiplet of levels.[33-38] For example, while theory has previously assumed spherically shaped dots with a cubic (zinc blende) crystal lattice, our dots are slightly prolate (aspect ratio 1.0 to 1.3) with a hexagonal (wurtzite) lattice. These attributes partially lift degeneracies.[33,34] The wurtzite lattice splits states due to the crystal field of the hexagonal lattice (analogous to the bulk A-B splitting).[33] The nonspherical shape of the dots splits states due to the change in confinement along the long and short axes of the ellipsoid.[34] In addition to these effects the exchange interaction between the electron and hole also affects the degeneracies.[35-38] While the exchange splitting is extremely small in bulk CdSe excitons (0.13meV),[51] it should be significant in confined structures where the overlap of the carriers is increased.[35-38]

In a treatment of the first excited state ($1S_{3/2}1S_e$) which includes the effect of the hexagonal lattice, nonspherical shape, and the exchange interaction, the initial eight-fold

degeneracy is split into five sublevels.[37,38] For the exchange interaction the important quantum number is the total angular momentum, $N = F_h+F_e$, where F_h (F_e) is the hole (electron) angular momentum. When the crystal field and/or the nonspherical shape are also included, the projection of N along the unique crystal axis, N_m, must be considered. The five sublevels are then described by $|N_m|$: one sublevel with $|N_m|=2$, two with $|N_m|=1$, and two with $|N_m|=0$. Levels with $|N_m|>0$ are two-fold degenerate.

This band edge exciton fine structure is consistent with the single dot lineshape in Fig. 4.6b. Figure 4.8 compares the model lineshape with the positions of the multiplet lines calculated from Ref. 37, assuming an aspect ratio of 1.1. The sublevels are labeled by $|N_m|$. We use superscripts to distinguish upper (U) and lower (L) sublevels with the same $|N_m|$. Both the $|N_m|=2$ and 0^L sublevels are optically forbidden within the electric dipole approximation. Only three sublevels (solid lines) are optically active.[37,38] Therefore, in this model the narrow bleach feature is assigned to 1^L and the broad feature is assigned to a combination of 1^U and 0^U. The small Stokes shift observed in FLN emission (Fig. 4.4) arises from the relaxation from the initially excited 1^L sublevel into the lowest lying state, the $|N_m|=2$ sublevel.

Since the $|N_m|=2$ sublevel is optically forbidden, the band edge structure can also explain the emission behavior.[37,38] The separation between the $|N_m|=2$ and 1^L sublevels is related to the Stokes shift, which increases with decreasing size (see chapter 5).[21,38] In most sizes the $|N_m|=2$ sublevel, also referred to as the "dark exciton", is sufficiently separated from 1^L such that thermalization is unimportant (at 10K) and band edge emission occurs from the $|N_m|=2$ state. Since a change in angular momentum of 2 is required to return to the ground state, an additional unit of angular momentum must be provided, for example by a phonon. This process is inefficient and the emission lifetime is long. The need to involve phonons also rationalizes the strong LO-phonon coupling in the FLN luminescence (Fig. 4.4).[37,38] In large dots where the separation between the dark exciton and 1^L approaches kT (at 10K), the radiative lifetime decreases[9,44] due to thermalization into the optically allowed 1^L sublevel.[37,38]

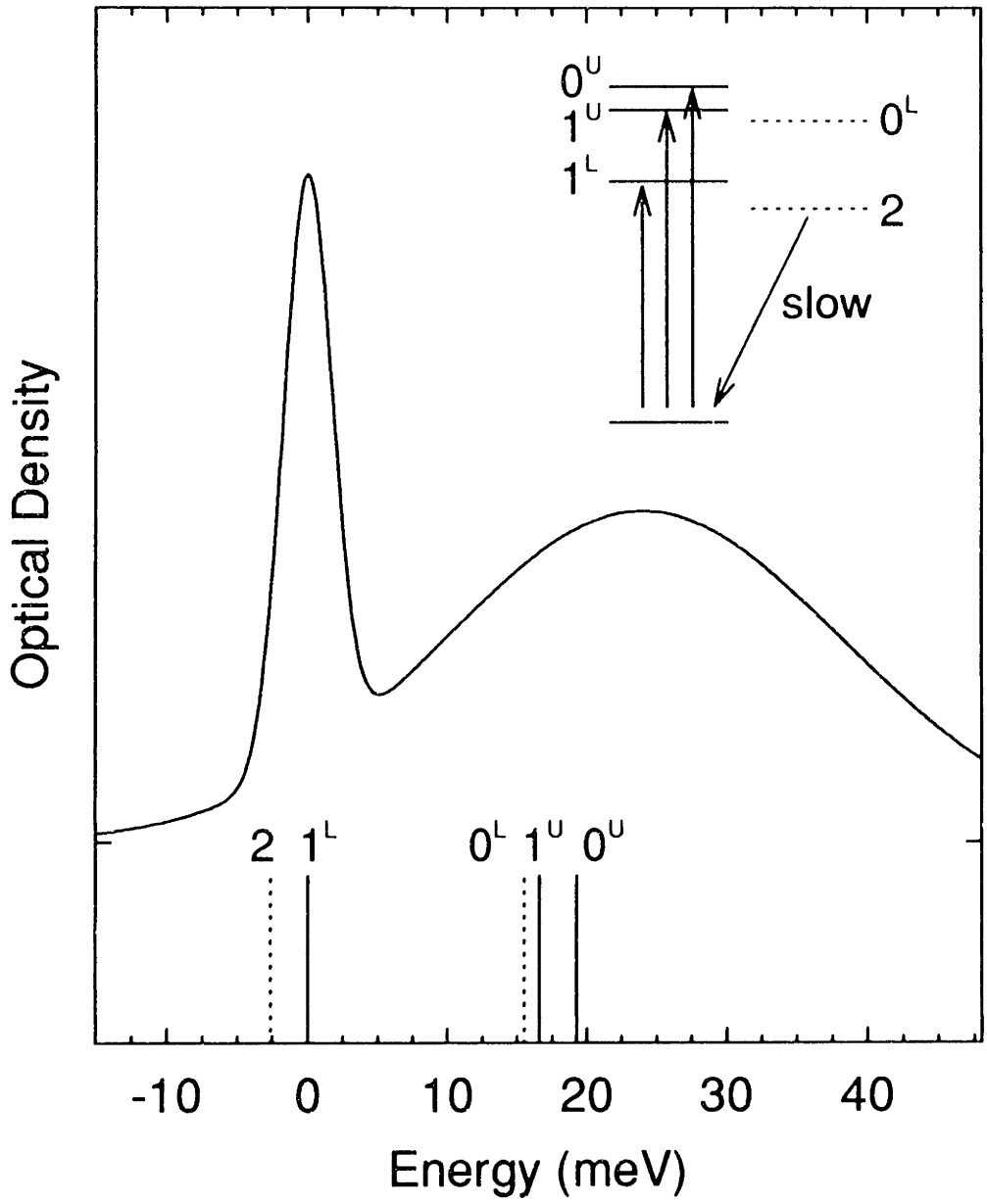

FIG. 4.8 Comparison of the single dot lineshape shown in Fig. 4.6b and the positions of multiplet lines calculated from Ref. 37 for the lowest excited state of 56Å diameter prolate dots with an aspect ratio of 1.1. The multiplet lines are labeled by $|N_m|$ with superscripts to distinguish upper (U) and lower (L) sublevels with the same $|N_m|$. Solid (dashed) lines are optically active (passive) levels. The absorbing and emitting states are qualitatively shown in an energy level diagram.

Although the $|N_m|=2$ and 1^L sublevels are observed as narrow emission and bleach features, respectively, the individual 1^U and 0^U sublevels, which combine to form the broad bleach, are not resolved. These lines may appear broad due to a combination of sample inhomogeneities and lifetime effects. When the pump excites dots which have their 1^L sublevel at the pump energy, the corresponding 1^U and 0^U bleaches may be smeared out due to size, shape, and structural inhomogeneities which cause variations in the sublevel spacings. In addition lifetime effects may cause the 1^U and 0^U sublevels to be inherently broad. While 1^L must flip a spin to relax to the $|N_m|=2$ level, 1^U and 0^U can rapidly relax without a spin flip into the 1^L and 0^L levels, respectively.[52] Therefore, 1^U and 0^U should be broader than 1^L. Such a rapid relaxation pathway exists for all higher excited state sublevels which are optically active and may explain the absence of additional narrow bleach features when the pump is tuned to higher energy.

Theoretical work[37,38] is considering all of these issues more quantitatively. Accurate prediction of the small Stokes shift, the intensity of the narrow and broad bleach components, and their size dependence, may better demonstrate the validity of this core model. These issues are pursued in chapters 5 and 6. If correct, the presence of exciton fine structure would have important implications. For example, recent femtosecond photon echo experiments have determined the various contributions to the homogeneous linewidth in CdSe quantum dots.[25,26] The presence of multiplet levels within the first inhomogeneous absorption line may contribute to the fast electronic dephasing measured in these systems.

4.6 Previous Results

Quantum dots prepared by other methods also show bleaches which have both broad and narrow band edge components. Klingshirn and co-workers[19,20] have reported TDA results for special CdSe and CdS_xSe_{1-x} doped glasses which exhibit bleaches similar to those shown in Fig. 4.2. When the dots are grown under conditions which avoid the coalescent stage of growth they observe a narrow feature at the pump energy which rides on top of a much broader bleach component. These similarities are significant because

they show that experimental TDA results obtained for colloidal and doped glass samples are beginning to converge.

To explain these results the coexistence of two different classes of quantum dots in doped glasses has been proposed.[19,20] Dots grown in the coalescent stage exhibit broad bleaches while dots grown which avoid the coalescent stage display narrow bleaches. This "two dot" model is consistent with the results of Klingshirn and co-workers[19,20] and can also explain why most quantum dot doped glasses[11-16] have only broad bleaches while older colloidal samples[17,21] have only narrow bleaches.

However, while we do not exclude slight variations in absorption properties in our samples, we do not believe that the two dot model explains our results. This model requires that the two classes of dots have dramatically different (broad and narrow) absorption properties. PLE data (Fig. 4.5) shows that the quantum yield in emission of the two dots must be nearly identical. (Otherwise, the absorption of the dots with higher quantum yield would dominate the PLE spectrum and the broad and narrow features would not appear as in the TDA spectra.) This result seems unlikely for dots which behave so differently in absorption. More importantly, the large "Stokes" shift in full luminescence cannot be explained with the two dot picture. These observations indicate that in our samples both features are present in a single dot. This behavior is consistent with the multiplet structure shown in Fig. 4.8.

The question remains whether the variations in quantum dot TDA results (doped glasses[11-16] which exhibit only broad bleaches and older colloidal dots[17,21] which exhibit only narrow bleaches) can also be rationalized by our model lineshape and the underlying multiplet structure (Fig. 4.8). Unlike our current samples, most quantum dot doped glasses do not exhibit band edge emission, but emit weakly via deep trap states. The low quantum yield in emission of these samples implies that efficient nonradiative pathways exist. Perhaps the band edge absorption (1^L) and emission ($|N_m|=2$) features, which appear narrow in our spectra, are lifetime broadened in doped glasses by rapid nonradiative relaxation which is not present in our samples. In this case only broad bleach features would appear in the TDA spectrum of doped glasses. Previous colloidal dots, discussed further in chapter 5, are similar to our present samples in that they emit from

narrow band edge features.[21] Accordingly, a narrow bleach feature also appears in their TDA spectra. This feature is much stronger than in Figs. 4.2 and 4.3. However, a recent reexamination of these samples shows that the broad bleaches are also present. They are simply much broader than in Fig. 4.6b. This situation may result from the poor quality of these early colloids. Since distributions in dot shape and crystal structure affect the multiplet spacings discussed above,[37,38] feature 2 in Fig. 4.6b, which arises from the 1^U and 0^U sublevels, would be further broadened. Therefore, in these older colloidal samples the broad bleach may be washed out by the inhomogeneities such that the narrow bleach feature dominates the TDA spectrum.

4.7 Conclusion

Our transient differential absorption (TDA) measurements demonstrate structure within the first absorption feature of CdSe quantum dots. We reproduce the experimental results for 56Å diameter dots with a single dot lineshape which contains both a narrow (FWHM 4.1meV) and a broad (34meV) component in the band edge absorption. This absorption lineshape is further supported by its ability to explain the large "Stokes" shift observed in the full luminescence. We find that surface models which have been proposed to explain the anomalous emission behavior of II-VI quantum dots are inconsistent with our data. However, core models, which completely ignore the surface, can explain our results. The observed band edge absorption structure is consistent with and is experimental evidence for the exciton fine structure recently predicted by theory.[33-38] We assign the narrow absorption feature to the lower $|N_m|=1$ sublevel of the first excited state while the broad absorption feature is assigned to a combination of the upper $|N_m|=1$ and $|N_m|=0$ sublevels. The band edge emitting state is the optically forbidden $|N_m|=2$ level or "dark exciton". The combination of a set of discrete states in the first absorption feature and an optically forbidden lowest state has important implications for both the study and the potential applications of these quantum dots.

4.8 References

1. Al. L. Efros and A. L. Efros, Fiz. Tekh. Poluprovodn. **16**, 1209 (1982) [Sov. Phys. Semicond. **16**, 772 (1982)].
2. L. E. Brus, J. Chem. Phys. **80**, 4403 (1984).
3. C. H. Henry and K. Nassau, Phys. Rev. B **1**, 1628 (1970).
4. L. Bányai, P. Gilliot, Y. Z. Hu, and S. W. Koch, Phys. Rev. B **45**, 14136 (1992).
5. M. O'Neil, J. Marohn, and G. McLendon, J. Phys. Chem. **94**, 4356 (1990).
6. A. Eychmüller, A. Hässelbarth, L. Katsikas, and H. Weller, Ber. Bunsenges. Phys. Chem. **95**, 79 (1991).
7. A. Hässelbarth, A. Eychmüller, and H. Weller, Chem. Phys. Lett. **203**, 271 (1993).
8. M. G. Bawendi, P. J. Carroll, W. L. Wilson, and L. E. Brus, J. Chem. Phys. **96**, 946 (1992).
9. M. Nirmal, C. B. Murray, and M. G. Bawendi, Phys. Rev. B **50**, 2293 (1994).
10. E. F. Hilinski, P. A. Lucas, and Y. Wang, J. Chem. Phys. **89**, 3435 (1988).
11. P. Roussignol, D. Ricard, C. Flytzanis, and N. Neuroth, Phys. Rev. Lett. **62**, 312 (1989).
12. N. Peyghambarian, B. Fluegel, D. Hulin, A. Migus, M. Joffre, A. Antonetti, S. W. Koch, and M. Lindberg, IEEE J. Quantum Electronics **QE-25**, 2516 (1989).
13. S. H. Park, R. A. Morgan, Y. Z. Hu, M. Lindberg, S. W. Koch, and N. Peyghambarian, J. Opt. Soc. Am. B **7**, 2097 (1990).
14. V. Esch, B. Fluegel, G. Khitrova, H. M. Gibbs, Xu Jiajin, K. Kang, S. W. Koch, L. C. Liu, S. H. Risbud, and N. Peyghambarian, Phys. Rev. B **42**, 7450 (1990).
15. K. I. Kang, A. D. Kepner, S. V. Gaponenko, S. W. Koch, Y. Z. Hu, and N. Peyghambarian, Phys. Rev. B **48**, 15449 (1993).
16. K. Kang, A. D. Kepner, Y. Z. Hu, S. W. Koch, N. Peyghambarian, C.-Y. Li, T. Takada, Y. Kao, and J. D. Mackenzie, Appl. Phys. Lett. **64**, 1487 (1994).
17. A. P. Alivisatos, A. L. Harris, N. J. Levinos, M. L. Steigerwald, and L. E. Brus, J. Chem. Phys. **89**, 4001 (1988).
18. M. G. Bawendi, W. L. Wilson, L. Rothberg, P. J. Carroll, T. M. Jedju, M. L. Steigerwald, and L. E. Brus, Phys. Rev. Lett. **65**, 1623 (1990).
19. U. Woggon, S. Gaponenko, W. Langbein, A. Uhrig, and C. Klingshirn, Phys. Rev. B **47**, 3684 (1993).
20. S. V. Gaponenko, U. Woggon, M. Saleh, W. Langbein, A. Uhrig, M. Müller, and C. Kingshirn, J. Opt. Soc. Am. B **10**, 1947 (1993).
21. D. J. Norris, M. Nirmal, C. B. Murray, A. Sacra, and M. G. Bawendi, Z. Phys. D **26**, 355 (1993).
22. D. J. Norris, A. Sacra, C. B. Murray, and M. G. Bawendi, Phys. Rev. Lett. **72**, 2612 (1994).
23. D. J. Norris and M. G. Bawendi, Phys. Rev. B (submitted).
24. W. Hoheisel, V. L. Colvin, C. S. Johnson, and A. P. Alivisatos, J. Chem. Phys. **101**, 8455 (1994).
25. R. W. Schoenlein, D. M. Mittleman, J. J. Shiang, A. P. Alivisatos, and C. V. Shank, Phys. Rev. Lett. **70**, 1014 (1993).
26. D. M. Mittleman, R. W. Schoenlein, J. J. Shiang, V. L. Colvin, A. P. Alivisatos, and C. V. Shank, Phys. Rev. B **49**, 14435 (1994).
27. A. I. Ekimov, F. Hache, M. C. Schanne-Klein, D. Ricard, C. Flytzanis, I. A. Kudryavtsev, T. V. Yazeva, A. V. Rodina, and Al. L. Efros, J. Opt. Soc. Am. B **10**, 100 (1993).
28. J. B. Xia, Phys. Rev. B **40**, 8500 (1989).
29. G. B. Grigoryan, E. M. Kazaryan, Al. L. Efros and T. V. Yazeva, Fiz. Tverd. Tela **32**, 1772 (1990) [Sov. Phys. Solid State **32**, 1031 (1990)].
30. K. J. Vahala and P. C. Sercel, Phys. Rev. Lett. **65**, 239 (1990).
31. P. C. Sercel and K. J. Vahala, Phys. Rev. B **42**, 3690 (1990).
32. S. W. Koch, Y. Z. Hu, B. Fluegel and N. Peyghambarian, J. Crystal Growth **117**, 592 (1992).
33. Al. L. Efros, Phys. Rev. B **46**, 7448 (1992).
34. Al. L. Efros and A. V. Rodina, Phys. Rev. B **47**, 10005 (1993).
35. S. Nomura, Y. Segawa and T. Kobayashi, Phys. Rev. B **49**, 13571 (1994).

36. M. Chamarro, C. Gourdon, P. Lavallard and A. I. Ekimov, Jpn. J. Appl. Phys. **34**, Suppl. 34-1, 12 (1995).
37. Al. L. Efros and M. Rosen (in preparation).
38. M. Nirmal, D. J. Norris, M. Kuno, M. G. Bawendi, Al. L. Efros, and M. Rosen (submitted).
39. C. B. Murray, D. J. Norris and M. G. Bawendi, J. Am. Chem. Soc. **115**, 8706 (1993).
40. L. R. Becerra, C. B. Murray, R. G. Griffin, and M. G. Bawendi, J. Chem. Phys. **100**, 3297 (1994).
41. J. E. Bowen Katari, V. L. Colvin, and A. P. Alivisatos, J. Phys. Chem. **98**, 4109 (1994).
42. Sizes reported are estimated from extensive size dependent transmission electron microscopy (TEM) and small angle x-ray measurements and are based on the wavelength of the first absorption peak.
43. The narrow bleach is observed even with a microsecond delay between the pump and probe and is not caused by scattered light from the nanosecond pump pulse.
44. Band edge fluorescence lifetimes are size dependent and increase with decreasing size.
45. S. Schmitt-Rink, D. A. B. Miller, and D. S. Chemla, Phys. Rev. B **35**, 8113 (1987).
46. S. Nomura and T. Kobayashi, Phys. Rev. B **45**, 1305 (1992).
47. *Landolt-Bornstein Numerical Data and Functional Relationships in Science and Technology*, New Series, Group III, Vol. 17b, edited by K. H. Hellwege (Springer-Verlag, Berlin, 1982).
48. By "single dot" lineshape we mean the lineshape required by each dot in our model to reproduce the TDA results. This lineshape may only be an approximation to the true single dot lineshape if multiple inhomogeneities are present, not all of which are removed by the TDA experiment.
49. A. E. Siegman, *Lasers*, (University Science Books, Mill Valley, CA, 1986), Chap. 30.
50. W. H. Press, B. P. Flannery, S. A. Teukolsky, and W. T. Vetterling, *Numerical Recipes in C* (Cambridge University Press, Cambridge, 1988), Chapter 14.
51. V. P. Kochereshko, G. V. Mikhailov, and I. N. Ural'tsev, Fiz. Tverd. Tela **25**, 769 (1983) [Sov. Phys. Solid State **25**, 439 (1983)].
52. This can easily be shown by writing the states of the coupled basis $|N\ ,\ N_m\rangle$ in terms of the uncoupled basis $|F_h\ M_h\ ;\ F_e\ M_h\rangle$. States such as $|1,\pm1\rangle$ (1^U) and $|2,\pm1\rangle$ (1^L) are both linear combinations of the same uncoupled states, simply with different coefficients. Therefore, relaxation from 1^U to 1^L does not require the electron or hole to flip spin.

Chapter 5

Excitonic Fine Structure in Emission: Observation of the "Dark Exciton"*

5.1 Introduction

To rationalize the extremely long radiative lifetimes present in II-VI quantum dots (~1μs at 10K), "surface models" have been proposed.[1-5] These models assume that immediately after the absorption event the photoexcited electron and/or hole is trapped at the dot/matrix interface. Surface-localization decreases electron-hole overlap and explains the slow recombination times. In essence, band edge emission is rationalized as a "surface effect". In chapter 4 we found that transient differential absorption (TDA) results appear inconsistent with these models. Absorption structure within the lowest excited state suggests that band edge emission is not caused by shallow surface traps. Therefore, an alternative explanation is required to explain the anomalous emission behavior of these systems.

New quantum dot "core models",[6] which were discussed in the last chapter, may provide an explanation.[7-12] These models extend effective mass treatments previously used to describe quantum dot absorption spectra[13-15] (see chapters 2 and 3). They include the effects of the internal crystal field and non-spherical shape of our dots, (which are wurtzite and slightly prolate),[16,17] as well as the electron-hole exchange interaction. In this case the first excited state ($1S_{3/2}1S_e$), which is 8-fold degenerate in standard quantum dot theoretical treatments, is split into five sublevels. In chapter 4 we show that these sublevels are consistent with the band edge absorption structure in TDA results. This band-edge-exciton fine structure is also significant since the lowest sublevel, referred to as the "dark exciton", is optically forbidden. Therefore, relaxation of the initially excited

---

* Chapter 5 is based on: D. J. Norris *et al.*, Z. Phys. D **26**, 355 (1993) and M. Nirmal *et. al.*, Phys. Rev. Lett. (submitted).

electron-hole pair into this state may explain the long radiative lifetimes observed in these systems.

In this chapter we examine the band-edge-exciton fine structure predicted by theory[7-12] and compare with emission results. We show that, although the calculated structure is strongly dependent on the size and shape of the dots, the model quantitatively explains the Stokes shift observed in the luminescence of our samples using only experimentally obtained parameters. Our emission data, therefore, provide strong supporting evidence for the band-edge-exciton fine structure and its implications for quantum dot optical behavior.

5.2 Experimental

To obtain size-dependent emission results we study eight CdSe samples ranging from ~23Å to ~83Å in mean diameter. The room temperature absorption spectra for this series is shown in Fig. 5.1. Since these samples, prepared according to the synthetic procedure reported in Ref. 18, represent one of the earliest quantum dot size series, they are more polydisperse than samples in other chapters which are obtained by newer techniques.[16,17] Typically they have size distributions (rms) between 8 and 10%. For optical measurements the dots were dispersed in tri-n-octyl-phosphine oxide, sealed under argon between sapphire flats, and cooled to 10K in a continuous flow helium cryostat (Janis Supertran).

The emission apparatus is shown in Fig. 5.2. Each sample is excited by the pulsed (~7ns) output of a 10 Hz Q-switched Nd:YAG/dye laser system (Continuum YG660-10 and TDL60). Band edge emission was dispersed by a single grating (600g/mm) 0.66m spectrometer (Jobin Yvon HR640) and detected by a 5ns-gated, intensified optical multichannel analyzer, or OMA (Princeton Instruments IRY-700G).

We also compare band edge absorption and emission features by simultaneously obtaining both emission and transient differential absorption (TDA) measurements on the same samples. A second sample series, similar to that shown in Fig. 5.1, is used in these experiments. To be optically clear at cryogenic temperatures, these samples were prepared as poly(vinyl butyral) polymer films as in chapter 2. The TDA apparatus is described in chapter 2 (Fig. 2.2).

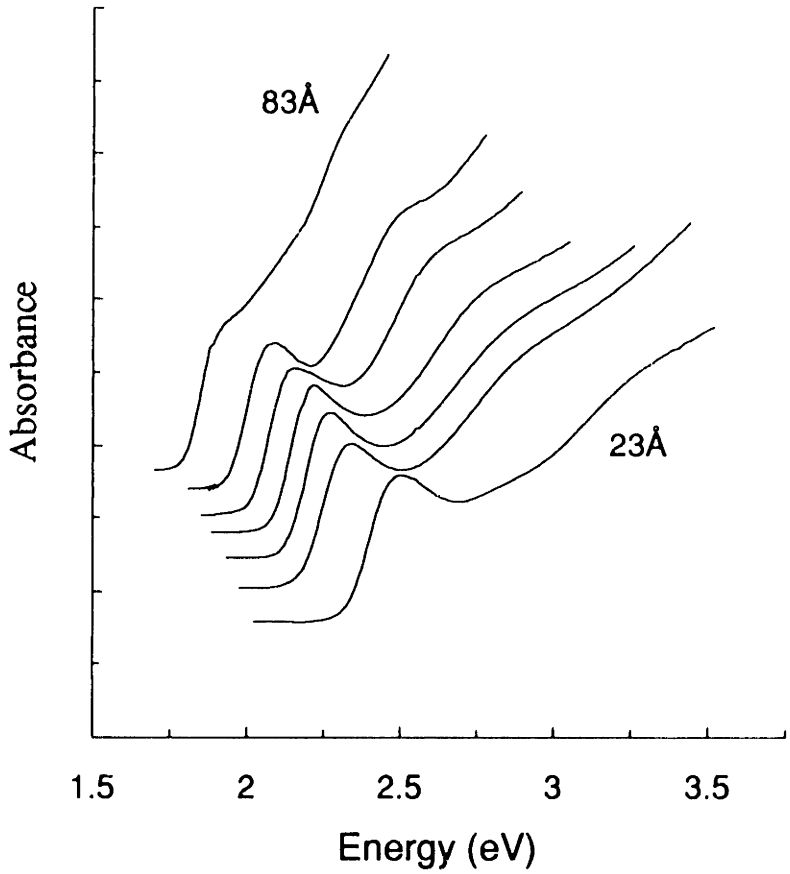

FIG. 5.1 Room temperature absorption spectra for CdSe quantum dots used in emission studies. The mean crystallite diameters are measured by TEM and range from 23Å to 83Å. Since these samples represent one of the earliest quantum dot size series, they are more polydisperse than samples in other chapters which are obtained by newer techniques (Refs. 16 and 17).

5.3 Theoretical Predictions

For spherical dots within the spherical band approximation,[30,31] quantum dot effective mass models predict that the lowest excited state ($1S_{3/2}1S_e$) is 8-fold degenerate. However, anisotropy in the internal crystal structure and/or shape of the dots lifts this degeneracy. In our dots, which are prolate with a wurtzite crystal structure[16,17] (long axis parallel to the unique "c" axis of the hexagonal lattice), the band edge state is split into two 4-fold degenerate levels, analogous to the bulk "A-B splitting" (see Fig. 3.13). The

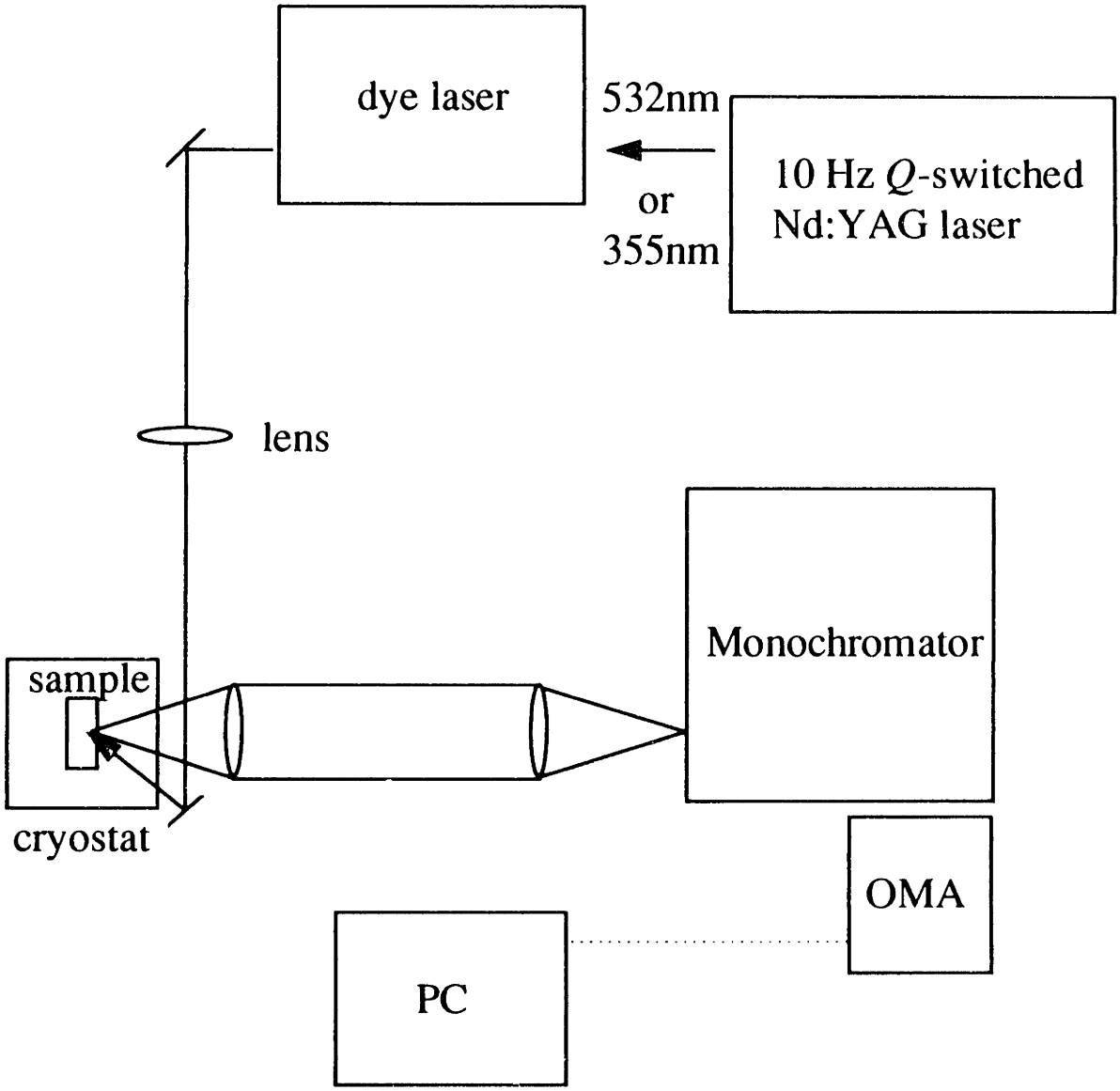

FIG. 5.2 FLN apparatus. The pulsed (~7ns) output of a 10 Hz *Q*-switched Nd:YAG/dye laser system was used to excite each sample. Band edge emission, dispersed by a 0.66m single grating (600g/mm) spectrometer, was detected using a 5ns-gated, intensified, optical multichannel analyzer (OMA).

net splitting (Δ) is the sum of the internal crystal field (Δ_{int}) and asymmetric shape components (Δ_{asym}),

$$\Delta(\beta,\mu,a) = \Delta_{int} + \Delta_{asym} \quad (5.1),$$

where β is the effective mass ratio of the bulk A and B bands along the "c" axis, a is the effective dot radius, defined as

$$a = \tfrac{1}{2}[b^2 c]^{1/3} \quad (5.2),$$

and μ, the degree of ellipticity, is

$$\mu = \frac{c}{b} - 1 \quad (5.3),$$

where c (b) is the major (minor) dot axis.[7,8]

The band edge state is further split by the electron-hole exchange interaction. Since this term is proportional to the spatial overlap between the electron and hole, an enhanced exchange effect is expected in low dimensional structures due to carrier confinement and has been confirmed in GaAs/GaAlAs quantum wells.[19] A further enhancement is predicted in QDs due to the three dimensional confinement of the electron and hole.[20] The exchange Hamiltonian in CdSe is,[21]

$$\hat{H}_{exch} = -\tfrac{2}{3} \cdot \varepsilon_{exch} \cdot (a_0)^3 \cdot \delta(\bar{r}_e - \bar{r}_h) \cdot (\hat{\sigma} \cdot \hat{J}) \quad (5.4),$$

where σ is the electron Pauli spin 1/2 matrix, $\mathbf{J}$ is the hole spin 3/2 matrix, a_0 is the lattice constant and ε_{exch} is the exchange strength constant (~320 meV in CdSe). Equation 5.4 mixes the electron and hole spin states and in bulk CdSe splits the fourfold degenerate A exciton into an optically active singlet and passive triplet by $\hbar\omega_{ST} \simeq 0.13$ meV.[22]

For CdSe quantum dots, the band edge exciton structure can be determined by including both the anisotropy (Eq. 5.1) and exchange terms (Eq. 5.4) within the framework of perturbation theory.[11] The initially 8-fold degenerate band edge exciton ($1S_{3/2}1S_e$) is split into 5 states. The good quantum number for the exchange interaction is the total angular momentum, $N = F_h + F_e$, where F_h (F_e) is the hole (hole) angular momentum. When the anisotropy terms are also included, the projection of the angular

momentum along the unique crystal axis, N_m, must be considered. Therefore, the 5 sublevels are labeled by $|N_m|$. States with $|N_m|>0$ are two-fold degenerate.

The sublevel energies can be expressed in terms of Δ and the size dependent exchange contribution[11]

$$\eta = \left(\frac{a_B}{a}\right)^3 \hbar\omega_{ST}\,\chi \qquad (5.5),$$

where a_B is the exciton Bohr radius and χ is a constant which in CdSe equals 0.78.[11] In terms of Δ and η, the size dependent energies of the five sublevels are[11]

$$\begin{aligned} \varepsilon_2 &= -\frac{3\eta}{2} - \frac{\Delta}{2} \\ \left.\begin{matrix}\varepsilon_{1U}\\ \varepsilon_{1L}\end{matrix}\right\} &= \frac{\eta}{2} \pm \sqrt{\frac{(2\eta-\Delta)^2}{4} + 3\eta^2} \\ \left.\begin{matrix}\varepsilon_{0U}\\ \varepsilon_{0L}\end{matrix}\right\} &= \frac{\eta}{2} + \frac{\Delta}{2} \pm 2\eta \end{aligned} \qquad (5.6).$$

The ordering of the levels in spherically-shaped, wurtzite dots is indicated in Fig. 5.3a. These states can be classified into two groups which converge to the bulk A and B excitons, respectively: $|N_m|=2$, 1^L and $|N_m|=0^L$, 1^U, 0^U. The superscripts U and L distinguish upper and lower states with the same angular momentum projection. Figure 5.3b shows that the crystallite shape strongly influences the band edge structure. For prolate dots (μ=0.3) the levels cross and the lowest state is either the $|N_m|=2$ or 0^L level, depending on the radius. For our samples transmission electron microscopy (TEM) and small angle x-ray (SAX) measurements indicate that the ellipticity ranges between 0 and 0.3, increasing with size.[16,17] In this case we obtain the band edge structure shown in Fig. 5.3c.[23] As in spherical dots, the $|N_m|=2$ level is the lowest excited state for all sizes.

In general the states fan out with decreasing size due to enhancement of the exchange term. Equation 5.4 implies that as quantum confinement increases the overlap of the electron and hole, the exchange interaction increases in strength. This effect is clearly demonstrated in the calculated exchange splitting between the $|N_m|=2$ and 1^L states in the smallest dots (~12.5 meV). The corresponding bulk value is two orders of magnitude smaller (0.13 meV).[22]

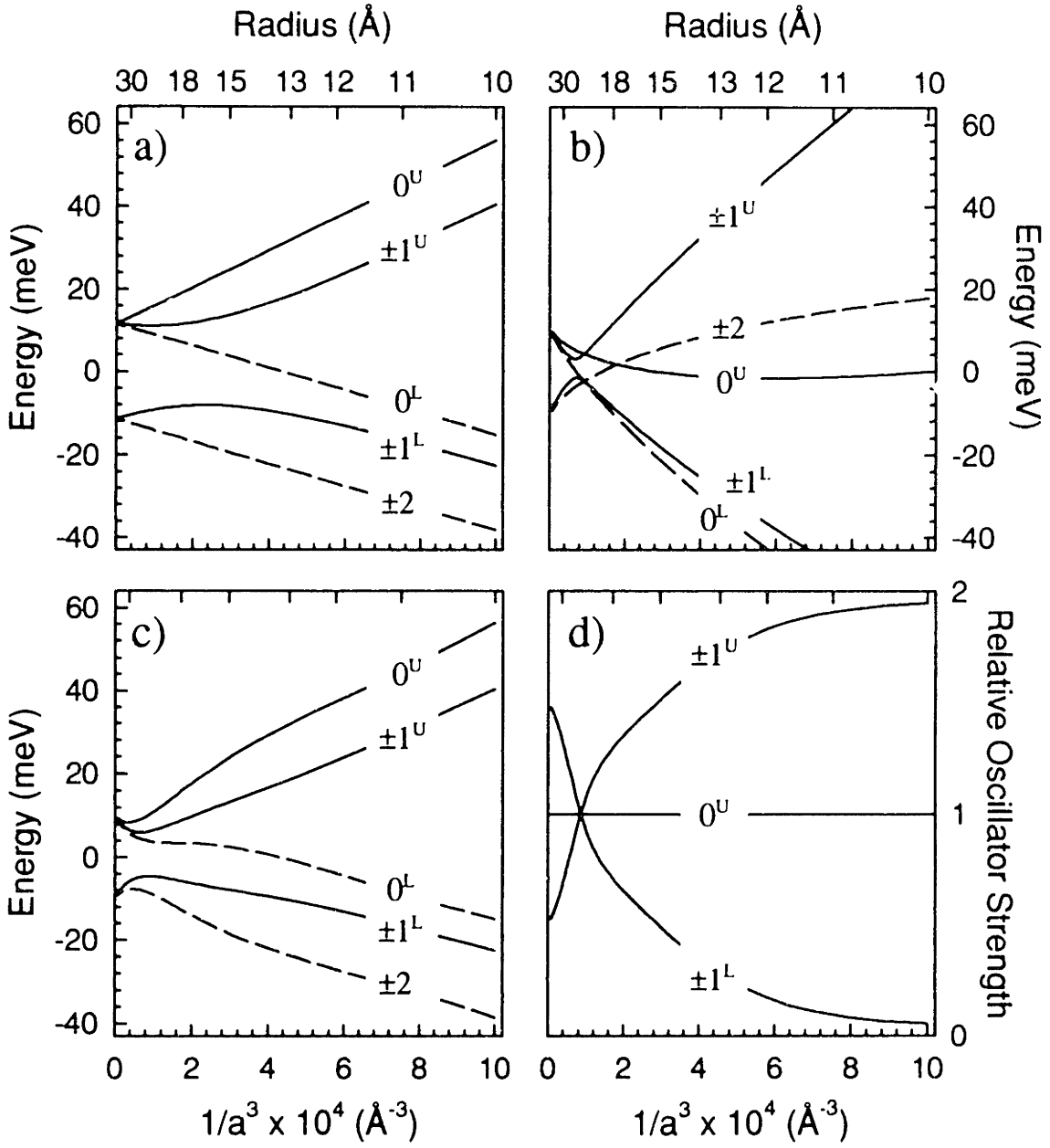

FIG. 5.3 Calculated band edge exciton ($1S_{3/2}1S_e$) structure vs. $1/a^3$ in CdSe quantum dots for various shapes: (a) spherical (μ=0), (b) prolate (μ=0.3), and (c) a size-dependent ellipticity, $\mu[a]$, consistent with transmission electron microscopy (TEM) and small angle x-ray (SAX) measurements. Dashed (solid) lines indicate optically passive (active) levels. (d) Oscillator strengths vs. $1/a^3$ for the optically active states in c relative to the 0^U. In all calculations we use literature values: a_B=56Å,[13] Δ_{exch}=0.13 meV,[22] and β=0.28.[15]

Theory also predicts that the oscillator strengths of the optically active levels are strongly modified by the exchange term. Following the approach of Ref. 7 the transition probabilities for randomly oriented quantum dots can be written as[11]

$$\left.\begin{matrix} P_{0U} \\ P_{0L} \end{matrix}\right\} = \frac{(1 \pm 1)^2 \, KP^2}{9}$$

$$\left.\begin{matrix} P_{1U} \\ P_{1L} \end{matrix}\right\} = \frac{4KP^2}{9}\left(\frac{2\sqrt{f^2+d} \mp f \pm \sqrt{3d}}{2\sqrt{f^2+d}}\right) \qquad (5.7),$$

where P is the Kane interband matrix element,

$$f = (-2\eta+\Delta)/2, \qquad (5.8)$$

$$d = 3\eta^2, \qquad (5.9)$$

and K is the square of the radial overlap integral

$$K = \frac{2}{a}\left|\int dr\, r \sin(\pi r/a)\, R_0(r)\right|^2 \qquad (5.10).$$

$R_0(r)$ is the hole radial function in the band edge exciton ($1S_{3/2}1S_e$). Note that Eq. 5.7 predicts that 0^L is optically passive.

In Fig. 5.3d the relative strength of the sublevels is plotted as a function of dot size. For all sizes the $|N_m|=2$ and 0^L levels are optically passive within the electric dipole approximation. The strength of the remaining three optically active levels are size dependent. This effect can be understood in terms of two opposing limits. In small dots the exchange term dominates and the good quantum number is the total angular momentum, N. In the absence of the internal crystal field and shape asymmetry ($\Delta=0$), the exchange term splits the band edge exciton into two states: $N=2$ and $N=1$. The $N=2$ state is optically forbidden. Since the 1^L sublevel is correlated to the $N=2$ state in the large exchange limit, we expect this sublevel to be only weakly allowed in small dots. In large dots, where the exchange term is negligible, the sublevels converge to A- and B-like excitons, both 4-fold degenerate. These two states each possess half of the total band edge oscillator strength. Therefore in large dots, the combined strength of 0^U and 1^U, which converge to the B-like exciton, is equal to the strength of 1^L, which converges to the A-like exciton. We discuss these effects further in chapter 6.

5.4 The Luminescence Stokes Shift

Previous quantum dot studies have shown that "single dot" emission information can be obtained via fluorescence line narrowing (FLN) spectroscopy.[5,29] By exciting each sample on the red edge of its first absorption feature, this technique optically selects the "largest" crystallites in the sample distribution. Thus inhomogeneous broadening is greatly reduced.

Figure 5.4 shows FLN results for the entire size series in Fig. 5.1. For comparison the spectra are plotted relative to the excitation energy. In each spectrum two LO-phonon lines are observed, separated by the LO-phonon frequency, ~25meV. A small amount of the excitation pulse is also detected as a narrow spike at zero energy. From these data several pieces of size-dependent information can be obtained. Most importantly, we can study the Stokes shift between the excitation energy and the peak of the zero-LO-phonon line. This shift is strongly size dependent, ranging from ~20 to ~2 meV in this size series. According to the predicted band edge structure (Fig. 5.3c), excitation on the red edge of the absorption spectrum probes the lowest optically active level (1^L). The emission is then shifted due to efficient relaxation to the band edge $|N_m|=2$ state. In Fig. 5.5 the Stokes shift data are compared with the calculated size dependent splitting between the $|N_m|=2$ and 1^L states. We obtain good agreement with no adjustable parameters, using only literature values: a_B=56Å,[3] Δ_{exch}=0.13meV,[16] β=0.28,[4] and $\mu[a]$.[17,23] Therefore, we find strong evidence for the band edge structure in our FLN emission results. In the smallest crystallites, however, the exchange splitting underestimates the observed FLN Stokes shift. This discrepancy may be due to an additional vibrational component since exciton-acoustic phonon coupling is predicted to scale as $1/a^2$.[24]

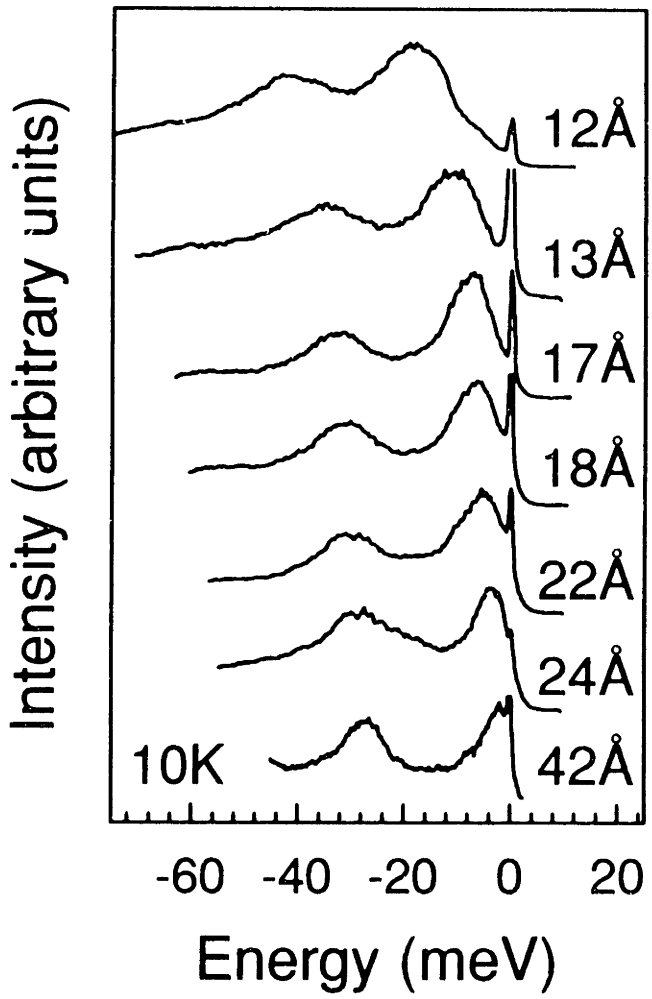

FIG. 5.4 Normalized FLN spectra for CdSe quantum dots shown in Fig. 5.1. Mean radii are determined from TEM measurements. A small amount of the pump laser is included for reference in each spectrum and set to zero energy for comparison.

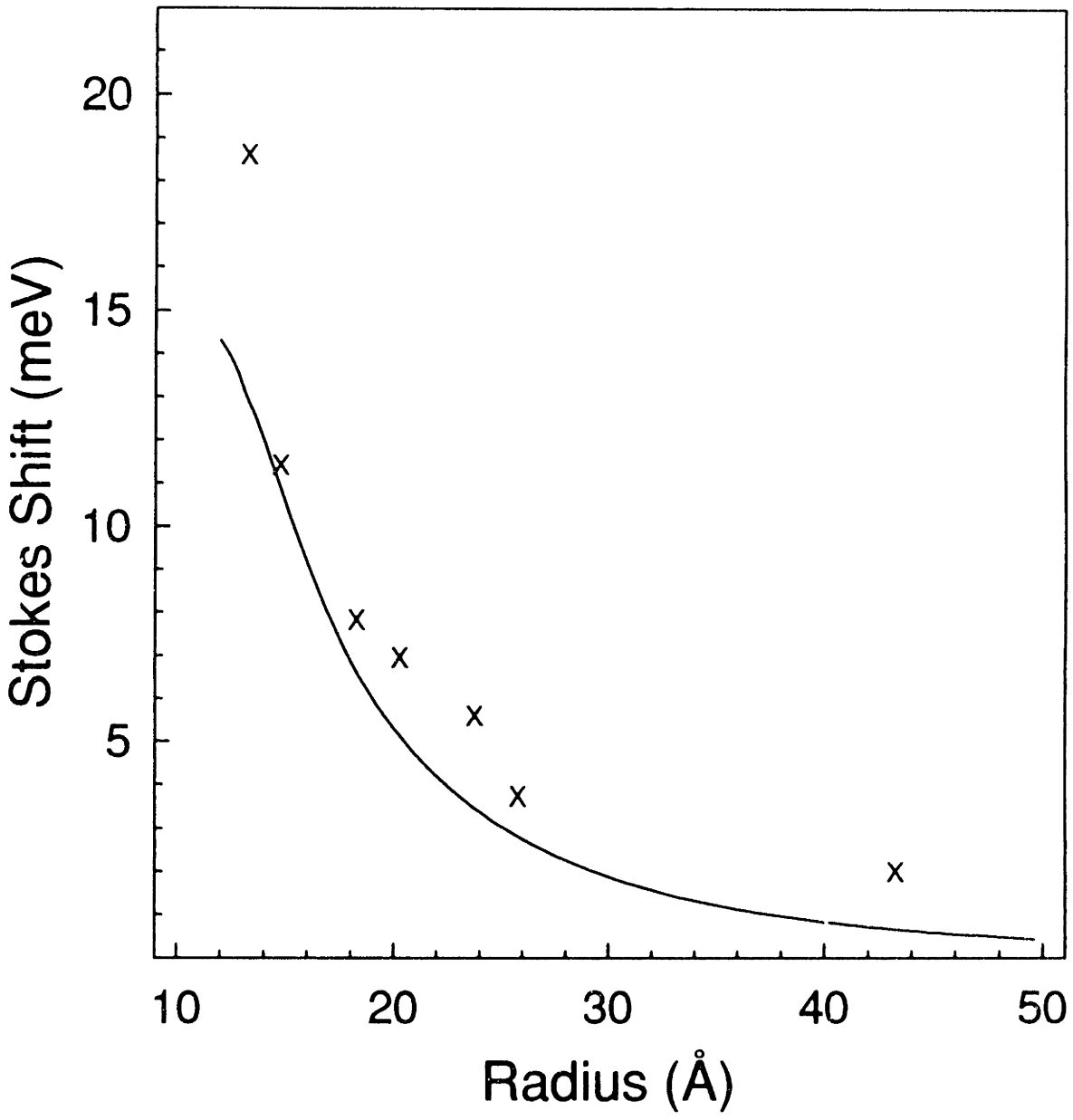

FIG. 5.5 Size dependence of the Stokes shift (x) between the pump position and the peak of the zero-LO-phonon-line, extracted from the FLN data in Fig. 5.4. The solid line is the calculated size dependent splitting between the $|N_m|=2$ and 1^L sublevels from Fig. 5.3c.

5.5 The Longitudinal Optical (LO) Phonon Frequency

Another size-dependent trend which can be extracted from the FLN results is the size dependence of the LO phonon frequency, shown in Fig. 5.6. Since the wavevector of the confined phonon is proportional to $1/a$ we plot the LO phonon frequency versus this coordinate to estimate the dispersion of the LO phonon mode. A red shift in the LO phonon frequency with decreasing radius is clearly observed. Very recent Raman studies on higher quality CdSe samples, prepared via the method of Ref. 16, confirm the presence of a red shift, although smaller in magnitude.[27] Such a decrease in frequency is expected as phonon confinement increases due to the negative dispersion of the bulk LO phonon mode. However, previous studies on CdS quantum dots show no phonon shift with size.[25] Studies on CdS(Se) quantum dot alloys even suggest a blue shift with decreasing size.[26] These results have been explained by invoking a strain-induced shift due to quantum dot surface tension. All of these results imply that the LO phonon frequency in quantum dots is strongly sample dependent.

5.6 The "Single Dot" Linewidth

Figure 5.4 also suggests that the homogenous linewidth of the emitting state is strongly size dependent. The linewidth of the zero-LO-phonon line increases with decreasing size. However, since the FLN spectrum is a convolution of both the absorption and emission linewidths, FLN alone cannot determine the linewidth of the emitting state. By combining FLN with TDA spectra, which depend only on the absorbing state, both contributions to the "single dot" linewidth can be determined. In Fig. 5.7 FLN and TDA results for the polymer film sample series is shown. For each sample identical pump energies were used in FLN and TDA. Each sample is excited on the red edge of its first absorption feature. Since the samples are among those which we described as "older colloidal" samples in chapter 4, the narrow bleach feature dominates the TDA spectrum. The broad bleach which appears in the TDA results of chapter 4 is much weaker in these

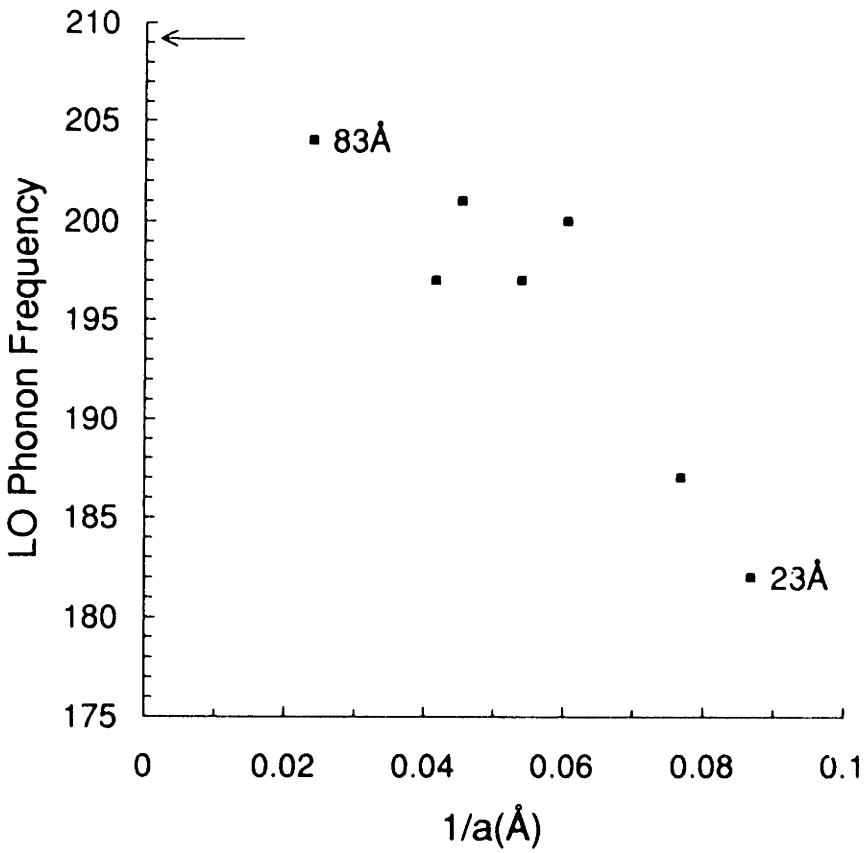

FIG. 5.6 LO phonon frequency (cm^{-1}) vs. $1/a$. Since the confined phonon wavevector is proportional to $1/a$ this plot represents the LO phonon dispersion. The data is extracted from the FLN spectra in Fig. 5.4. The black arrow designates the bulk LO phonon frequency from Ref. 28.

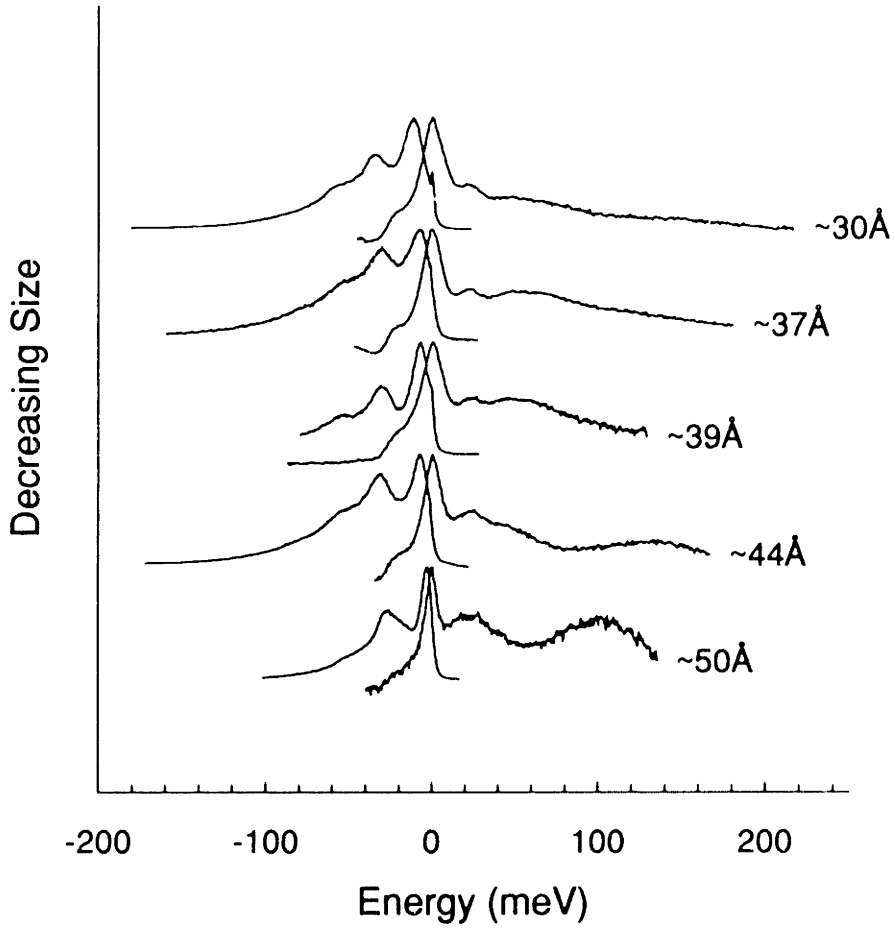

FIG. 5.7 Normalized FLN intensity (left) and TDA spectra (right) vs. energy for a series of CdSe quantum dots. All spectra were obtained at 10K. For comparison the excitation energy for each sample, identical in FLN and TDA, has been set to zero. In TDA, plotted as negative change in optical density (-ΔOD), positive signal refers to a bleach in the ground state absorption. Sizes are mean diameters extrapolated from transmission electron microscopy (TEM) measurements.

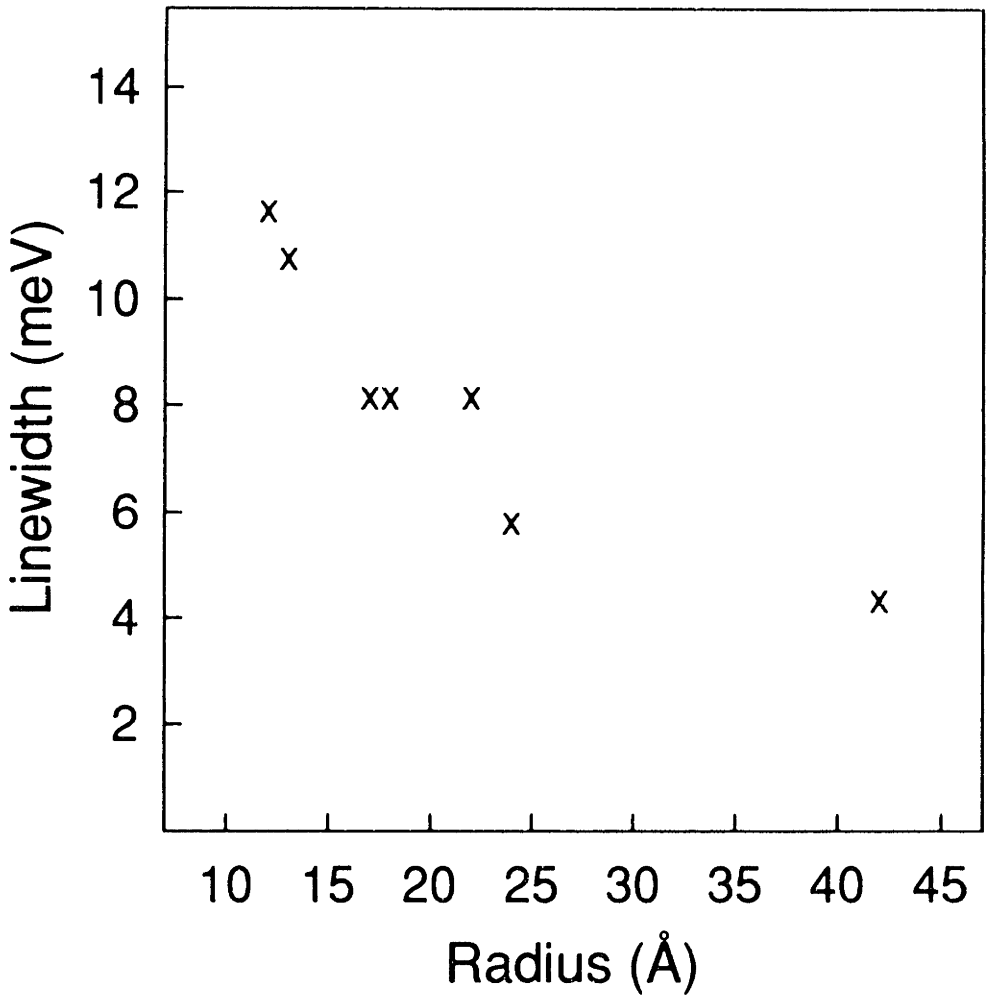

FIG. 5.8 "Single dot" emission linewidth (full width at half maximum) vs. quantum dot radius, extracted from Fig. 5.3

samples. Inspection of Fig. 5.7 indicates that the zero-phonon-line in the FLN spectrum and the narrow bleach feature from the TDA spectrum have very similar linewidths. Indeed, when "single dot" information is extracted from these features quantitatively, the linewidth of the absorbing and emitting states are identical within experimental error. Therefore, we assume this constraint and return to the larger size series in Fig. 5.4. We deconvolute the "single dot" emission (or absorption) lineshape, which is plotted vs. radius in Fig. 5.8.

In chapter 4 we argued that the strong similarity between the narrow absorption and emission features observed in FLN and TDA results (Fig. 4.4) is inconsistent with models which use surface traps to explain band edge emission. The absorbing state and the long-lived, surface-localized emitting state were expected to have very different lineshapes. Our current results show that this similarity is not peculiar to sample A from chapter 4, but rather a more general property of CdSe quantum dots. While these results again appear to conflict with the surface model, they are consistent with the band-edge-exciton fine structure. We expect the $|N_m|=2$ and 1^L sublevels to have similar lineshapes, as observed. Therefore, these results continue to support the band-edge-exciton fine structure predicted by theory.

5.7 Conclusion

In this chapter we investigate the band-edge-exciton splittings predicted by quantum dot theories. We consider how the size and shape of the dots influences the band-edge-exciton fine structure and compare the theoretical predictions with fluorescence line narrowed (FLN) emission results. We find that the size dependence of the luminescence Stokes shift, extracted from our data, is quantitatively reproduced by the predicted splitting between the lowest optically allowed sublevel (1^L) and the "dark exciton" ($|N_m|=2$). Therefore, our results are strong evidence for the predicted band-edge-exciton fine structure and the observation of the "dark exciton" in emission.

We also compare FLN and TDA spectra to investigate the "single dot" linewidth for the absorbing and emitting states. We find that for each sample the absorbing and emitting state linewidths are identical within our experimental error and increase with decreasing

size. This is again consistent with the observation of two sublevels ($|N_m|$=2 and 1^L) within the band-edge-exciton. According to the model,[11] these sublevels are expected to have similar linewidths.

5.8 References

1. M. O'Neil, J. Marohn, and G. McLendon, J. Phys. Chem. **94**, 4356 (1990).
2. A. Eychmüller, A. Hässelbarth, L. Katsikas, and H. Weller, Ber. Bunsenges. Phys. Chem. **95**, 79 (1991).
3. A. Hässelbarth, A. Eychmüller, and H. Weller, Chem. Phys. Lett. **203**, 271 (1993).
4. M. G. Bawendi, P. J. Carroll, W. L. Wilson, and L. E. Brus, J. Chem. Phys. **96**, 946 (1992).
5. M. Nirmal, C. B. Murray, and M. G. Bawendi, Phys. Rev. B **50**, 2293 (1994).
6. By "core models" we mean those which completely ignore the surface.
7. Al. L. Efros, Phys. Rev. B **46**, 7448 (1992).
8. Al. L. Efros and A. V. Rodina, Phys. Rev. B **47**, 10005 (1993).
9. S. Nomura, Y. Segawa and T. Kobayashi, Phys. Rev. B **49**, 13571 (1994).
10. M. Chamarro, C. Gourdon, P. Lavallard and A. I. Ekimov, Jpn. J. Appl. Phys. **34**, Suppl. 34-1, 12 (1995).
11. Al. L. Efros, M. Rosen, M. Kuno, M. Nirmal, D. J. Norris, and M. G. Bawendi (in preparation).
12. M. Nirmal, D. J. Norris, M. Kuno, M. G. Bawendi, Al. L. Efros, and M. Rosen (submitted).
13. A. I. Ekimov, F. Hache, M. C. Schanne-Klein, D. Ricard, C. Flytzanis, I. A. Kudryavtsev, T. V. Yazeva, A. V. Rodina, and Al. L. Efros, J. Opt. Soc. Am. B **10**, 100 (1993).
14. D. J. Norris, A. Sacra, C. B. Murray, and M. G. Bawendi, Phys. Rev. Lett. **72**, 2612 (1994).
15. D. J. Norris and M. G. Bawendi, Phys. Rev. B (submitted).
16. C. B. Murray, D. J. Norris and M. G. Bawendi, J. Am. Chem. Soc. **115**, 8706 (1993).
17. C. B. Murray, Ph.D. Thesis, Massachusetts Institute of Technology, 1995.
18. C. B. Murray, M. Nirmal, D. J. Norris, and M. G. Bawendi, Z. Phys. D **26S**, 231 (1993).
19. M. Potemski, J. C. Maan, A. Fasolino, K. Ploog, and G. Weimann, Surf. Sci. **229**, 151 (1990).
20. T. Takagahara, Phys. Rev. B **47**, 4569 (1993).
21. G. L. Bir and G. E. Pikus, *Symmetry and Strain-Induced Effects in Semiconductors* (Wiley, New York 1975).
22. V. P. Kochereshko, G. V. Mikhailov, and I. N. Ural'tsev, Sov. Phys. Solid State **25**, 439 (1983).
23. We approximate the size-dependent ellipticity, $\mu(a)$, by fitting experimental aspect ratio results from Refs. 16 and 17 to a polynomial.
24. S. Nomura and T. Kobayashi, Solid State. Commun. **82**, 335 (1992).
25. J. J. Shiang, A. N. Goldstein, and A. P. Alivisatos, J. Chem. Phys. **92**, 3232 (1990).
26. G. Scamarcio, M. Lugara, D. Manno, Phys. Rev. B **45**, 13792 (1992).
27. J. J. Shiang, R. K. Grubbs, and A. P. Alivisatos, Phys. Rev. B (submitted).
28. *Landolt-Bornstein Numerical Data and Functional Relationships in Science and Technology*, New Series, Group III, Vol. 17b, edited by K. H. Hellwege (Springer-Verlag, Berlin, 1982).
29. M. G. Bawendi, W. L. Wilson, L. Rothberg, P. J. Carroll, T. M. Jedju, M. L. Steigerwald, and L. E. Brus, Phys. Rev. Lett. **65**, 1623 (1990).
30. A. Baldereschi and N. O. Lipari, Phys. Rev. B **8**, 2697 (1973).
31. In the spherical band approximation, outlined in Ref. 30 for the charged impurity problem, only terms of spherical symmetry in the Luttinger Hamiltonian are considered in first order. Cubic "warping" terms are neglected but may be added as a small perturbation.

Chapter 6

Further Evidence of Exciton Fine Structure: Size Dependence of Band Edge Absorption and Emission Features*

6.1 Introduction

Nanometer scale semiconductor crystallites (or quantum dots) provide an opportunity to investigate excitons which are confined in all three dimensions. In these so-called zero-dimensional materials an electron-hole pair generated by optical absorption is spatially confined by the quantum dot boundary. If the quantum dots are small compared to the exciton Bohr radius, they exhibit optical properties which differ dramatically from the bulk material. The bulk valence and conduction bands are quantized and discrete transitions which increase in energy with decreasing size appear in the quantum dot spectrum.[1,2] These general properties have been demonstrated by numerous optical studies on II-VI dots such as CdS and CdSe.[3] However, more detailed investigations have been hindered by the inability to produce high quality samples of varying size. Recently developed synthetic methods,[4] which yield II-VI quantum dots ranging from ~15 to ~120Å in diameter with extremely narrow size distributions (<4% rms), now allow many more issues to be addressed.

In chapters 2 and 3 we used such a series of high quality CdSe dots to follow the size evolution of ten transitions in the quantum dot optical spectrum.[5] In general these absorption features are well described by effective mass models which incorporate the complexities of the CdSe valence band.[6-10] However, while these models predict that the lowest energy electron-hole pair state ($1S_{3/2}1S_e$ – which we will refer to as the "band edge exciton") is 8-fold degenerate, we also observe structure within the first absorption feature

---

* Much of chapter 6 will appear in print: D. J. Norris, Al. L. Efros, M. Rosen, and M. G. Bawendi, Phys. Rev. B. (submitted).

of our samples. Such structure has been predicted to arise in the band edge exciton due to the nonspherical shape and internal crystal structure of our dots,[11,12] which are slightly prolate with a wurtzite lattice.[4] Both effects should split the band edge exciton into two 4-fold degenerate states, analogous to the bulk "A-B splitting" (see Fig. 3.13).[11,12] In addition the exchange interaction between the electron and hole should strongly modify the band edge exciton structure.[13-16] The exchange splitting, while negligible in the bulk, should be strongly enhanced by quantum confinement.[13] When all of these effects are combined, the resulting band edge structure has important implications for quantum dot optical behavior. For example, the lowest quantum dot level is predicted to be optically forbidden and this may explain the long (~1μs at 10K) radiative lifetimes observed in these systems.[15]

To further test these models, in this chapter we present the size dependence of the band edge absorption structure in CdSe quantum dots. In chapter 4 we reported the band edge structure of a ~30Å effective radius[17] sample using transient differential absorption (TDA) spectroscopy.[18] This technique reduces residual sample inhomogeneities present in even the highest quality QD samples. In this chapter we use two simpler optical methods, photoluminescence excitation (PLE) and fluorescence line narrowing (FLN) spectroscopies, to reduce inhomogeneities and obtain absorption and emission information for each sample in our size series. Our new data support our previous conclusion[18] that the absorption structure is the band edge exciton fine structure predicted by theory.[11-16]

6.2 Experimental

We study eight CdSe samples (A-H) with mean effective radii ranging from ~15Å (A) to ~50Å (H).[17] The dots are prepared according to the method of Ref. 4. In this procedure the wet chemical synthesis is followed by size-selective precipitation to further narrow the size distribution. Nearly monodisperse (σ<4%) samples are obtained which contain near defect-free, wurtzite crystallites with well passivated surfaces.[4,19-21] The dots are prolate with an aspect ratio ranging between 1.0 and 1.3, increasing with dot size.[4,21] The long axis is parallel to the unique "c" axis of the wurtzite lattice. Our samples exhibit

strong band edge luminescence with a quantum yield (at 10K) greater than 0.1 and measured as high as 0.9.

For optical measurements five of the samples were isolated from their growth solution and redispersed in n-hexane with a small amount of tri-n-octyl-phosphine (TOP) added. The remaining three, which were prepared to obtain absorption as well as PLE and FLN data, were redispersed in tri-n-butyl-phosphine (TBP) with *o*-terphenyl added (250 mg/ml) to form an optically clear organic glass at cryogenic temperatures. We find no difference between these two solvent mixtures in our results. An excess of TBP or TOP, both surface capping groups, maintains surface passivation and preserves the high photoluminescence quantum yield.[21] Each sample solution is sealed between sapphire flats separated by a 0.5mm thick Teflon spacer and mounted in a helium cryostat. All spectra are obtained at 10K.

PLE and FLN measurements are recorded with a commercial spectrofluorometer (Spex Fluorolog-2). This instrument consists of two double (0.22m) spectrometers. The first selects the desired excitation energy from the emission of a xenon arc lamp. The second selects the emission energy detected by a photomultiplier tube (R928) with photon counting electronics. Under typical experimental conditions the combined resolution of our instrument was ~1.5meV (FWHM).

6.3 Results

Figure 6.1a shows absorption and emission results for sample B (~19Å effective radius). The emission spectrum, referred to as "full luminescence", is obtained by exciting the sample well above its first transition so that emission occurs from the entire sample distribution. While no structure is observed within the band edge absorption and emission features, residual sample inhomogeneities conceal band edge spectral features. FLN and PLE spectroscopies, demonstrated in Fig. 6.1b, can provide higher resolution and reveal band edge structure.[22] In FLN a subset of the sample distribution is optically excited, revealing a significantly narrowed and structured spectrum. For example, when sample B is excited on the low energy side of its first absorption feature (downward arrows in Fig.

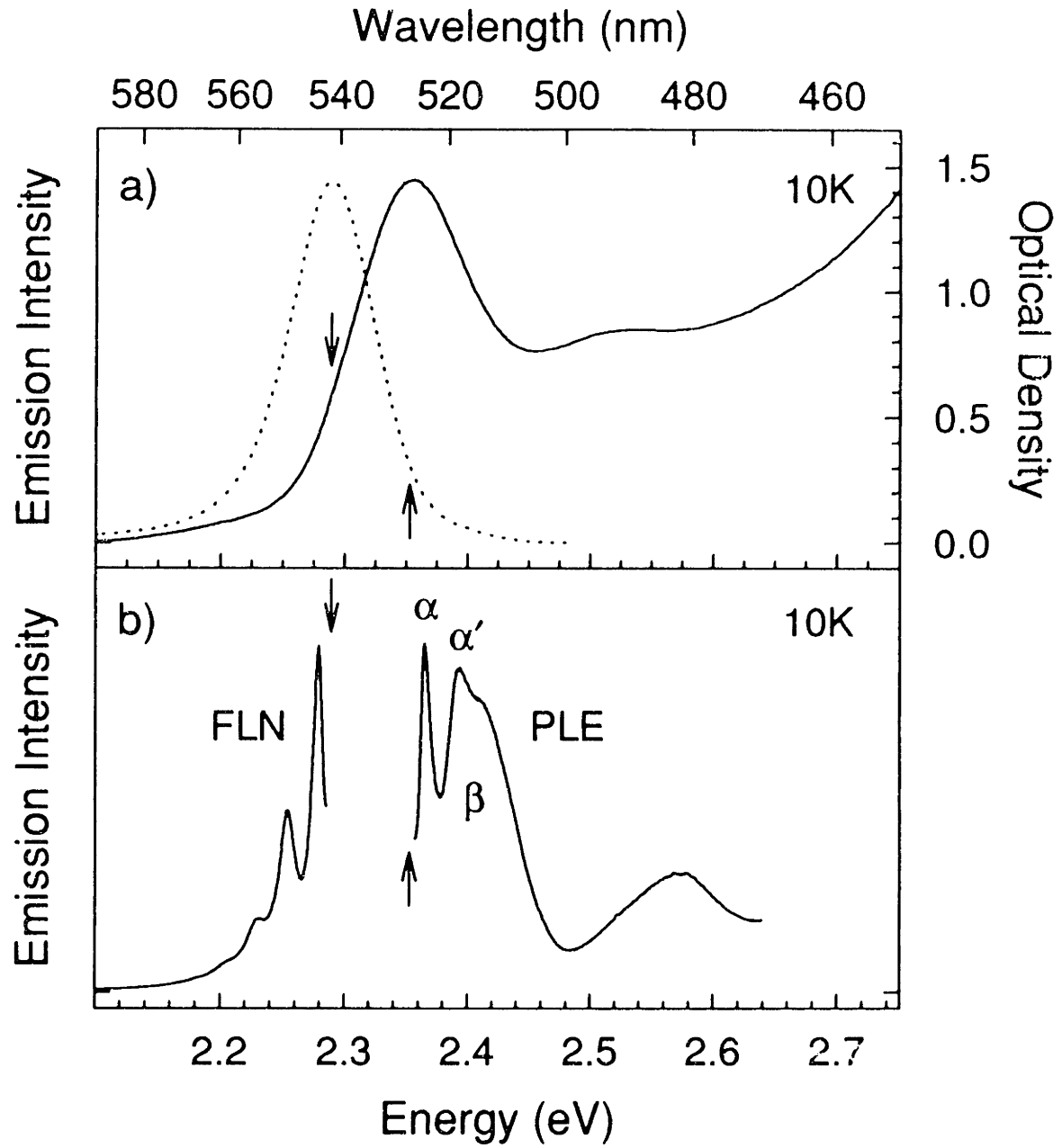

FIG. 6.1 (a) Absorption (solid line) and full luminescence (dotted line) spectra for sample B, ~19Å effective radius. (b) FLN and PLE spectra for sample B. A LO-phonon progression is observed in FLN. Both narrow (α,α') and broad (β) absorption features are resolved in PLE. The downward (upward) arrows denote the excitation (emission) position used for FLN (PLE).

6.1) a longitudinal optical (LO) phonon progression is clearly resolved. This FLN spectrum can be used to extract a model "single dot" emission lineshape.[26] PLE can similarly be used to extract "single dot" absorption information by monitoring a narrow spectral band (upward arrows) of the full luminescence while scanning the excitation energy. As seen in Fig. 6.1b, additional structure in the first absorption feature is resolved with this technique. A narrow feature (α), its LO phonon replica (α'), and a broader feature (β) are observed. Due to this increase in resolution, PLE has become a standard technique to obtain QD absorption information.[5,22-25]

For a particular sample, the overall shape of the band edge PLE structure depends on where we monitor the full luminescence. Similarly, FLN results depend on the excitation position. For example, Fig. 6.2 shows seven FLN and PLE scans for sample B. For each pair of FLN/PLE results (numbered 1-7) the FLN excitation energy and PLE emission energy are identical. These energies are represented by arrows and shown with the full luminescence. As the PLE emission position is moved to lower energy (from 1 to 7), the broad underlying feature (β) broadens and additional phonon replicas of the narrow feature (α) appear. The highest resolution in PLE is thus obtained when the emission is monitored on the blue edge of the full luminescence, probing the "smallest" dots in the distribution.[22,27] In contrast to PLE, the FLN spectra broaden as the excitation position is moved to higher energy, eventually approaching the full luminescence in curve 1. The highest resolution in FLN is obtained by exciting the sample on the red edge of the first absorption feature, probing the "largest" dots in the distribution.[22,27]

These trends originate in the inhomogeneous sample distribution. In FLN, the "single dot" emission lineshape is convoluted with unwanted absorption information. Any dot which has an absorption feature at the excitation energy is excited. In PLE, the "single dot" absorption lineshape is convoluted with unwanted emission information. The PLE experiment simultaneously monitors dots which emit from different LO-phonon lines. In both cases, the fractions of dots which have a particular absorption feature or phonon-line at the excitation or emission position is determined by the sample distribution. However, despite this contamination of the PLE and FLN results, "single dot" absorption and

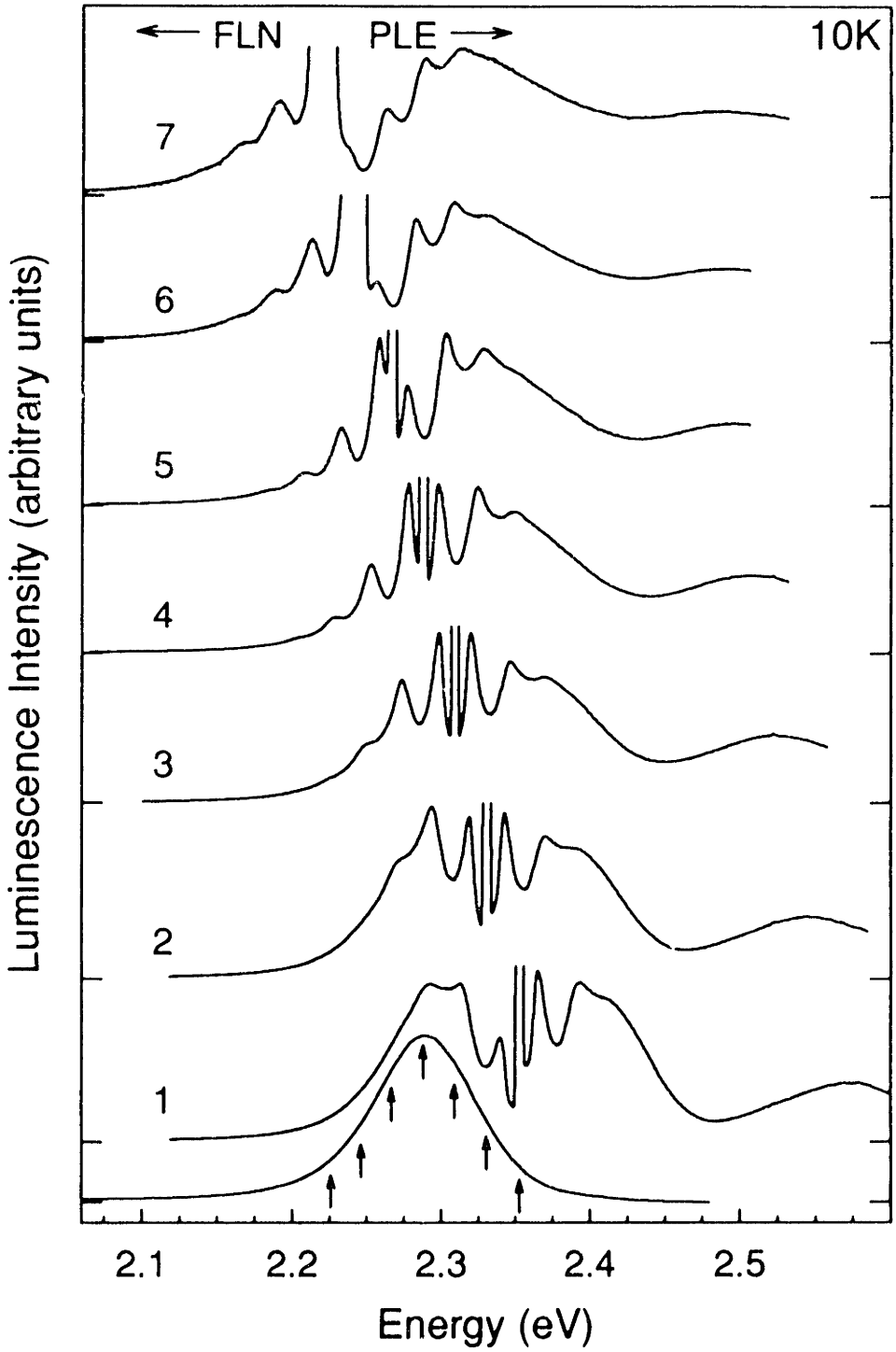

FIG. 6.2 Normalized FLN and PLE data for sample B for various emission and excitation positions. For each FLN/PLE pair, the FLN excitation and PLE emission energies are identical. These energies are designated by arrows and shown with the full luminescence. FLN emission becomes sufficiently weak in curves 6 and 7 that the zero-phonon-line of the emitting state is obscured by scattered excitation light.

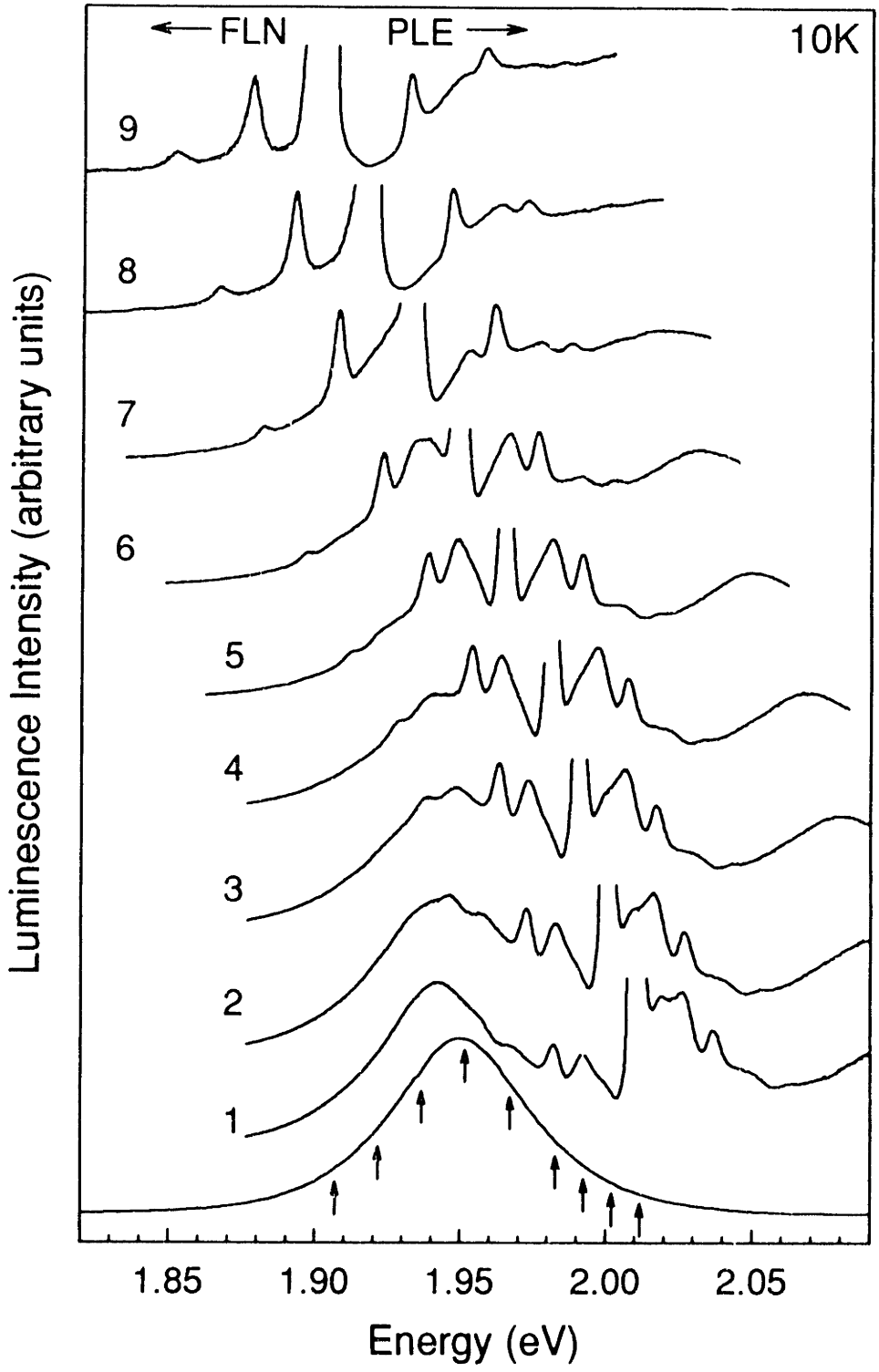

FIG. 6.3 Normalized FLN and PLE data for sample G (~44Å effective radius) as in Fig. 6.2. For each FLN/PLE pair, the FLN excitation and PLE emission energies are the same. These energies are designated by arrows and shown with the full luminescence.

emission lineshapes[26] can be extracted from a complete data set such as that in Fig. 6.2. For each sample in our size series (A-H) we record a similar FLN/PLE data set. Here we present complete and representative sets for samples B (Fig. 6.2) and G (Fig. 6.3). The remainder are shown in the appendix.

The compete data set for sample G is shown in Fig. 6.3 to demonstrate the particularly interesting band edge structure which develops in larger dots. Figure 6.4 shows curve 2 from Fig. 6.3 in more detail. Although the spectra for sample G (Fig. 6.4) appear more complex than for sample B (Fig. 6.1b), the primary difference is that the broad absorption feature (β in Fig. 6.1b) is now split into two features (β_1 and β_2 in Fig. 6.4). In addition the linewidths of β_1 and β_2 are comparable to the linewidth of α. In other words, while in sample B three band edge states are resolved: a narrow emitting state, a narrow absorbing state (α), and a broad absorbing state (β), in sample G four band edge states are present: a narrow emitting state and three narrow absorbing states (α, β_1 and β_2). Although the emission still arises from a single LO-phonon progression, as indicated by curve 9 in Fig. 6.3, the absorption structure causes three overlapping phonon progressions to appear in the FLN and PLE results in Fig. 6.4. Each progression can be assigned to one of the three absorbing features (horizontal brackets in Fig. 6.4). For example, the FLN feature labeled β_2 and its replica are observed because of absorption by a subset of dots into β_2 followed by relaxation into the emitting state. We note that since the separation between α and the emitting state (the Stokes shift) is ~1 meV in dots of this size, the zero-phonon-line of α is obscured by scattered excitation light in PLE. Similarly, in FLN the zero-phonon-line of the emitting state is obscured for those dots which absorb directly into α. However, higher replicas due to α are clearly observed in both FLN and PLE.

The size evolution of the band edge structure is shown in Fig. 6.5 which compares FLN/PLE results for each sample in our series. The PLE spectrum with the highest resolution is shown. For each FLN/PLE pair the FLN excitation and PLE emission energies are the same and the data are plotted relative to this energy. The actual excitation/emission positions are indicated with arrows in the full luminescence spectra, shown in Fig. 6.6.

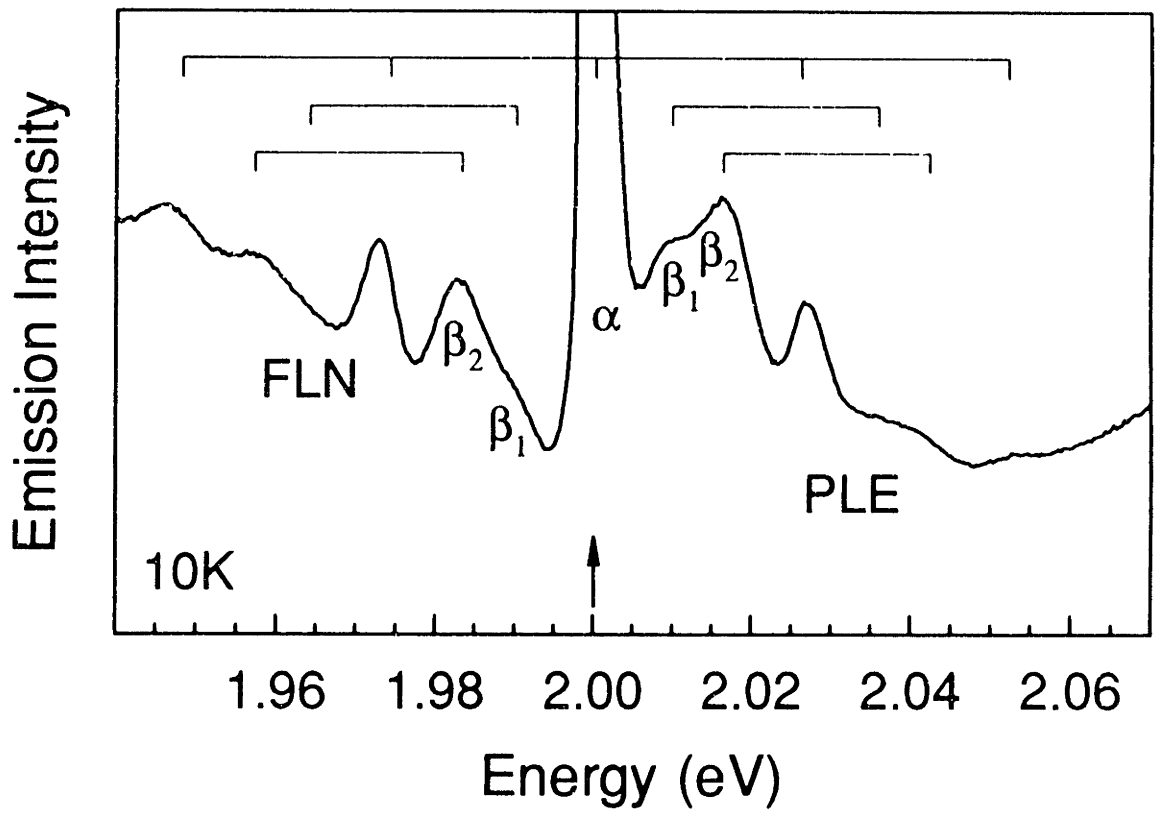

FIG. 6.4 Detail of FLN and PLE data for sample G (curve 2 from Fig. 6.3). Although emission arises from a single emitting state and its LO-phonon replicas, three overlapping LO-phonon progressions are observed in FLN due to the three band edge absorption features (α, β_1 and β_2). Horizontal brackets connect the FLN and PLE features with their LO-phonon replicas. The arrow denotes both the FLN excitation and PLE emission energies (2.000 eV).

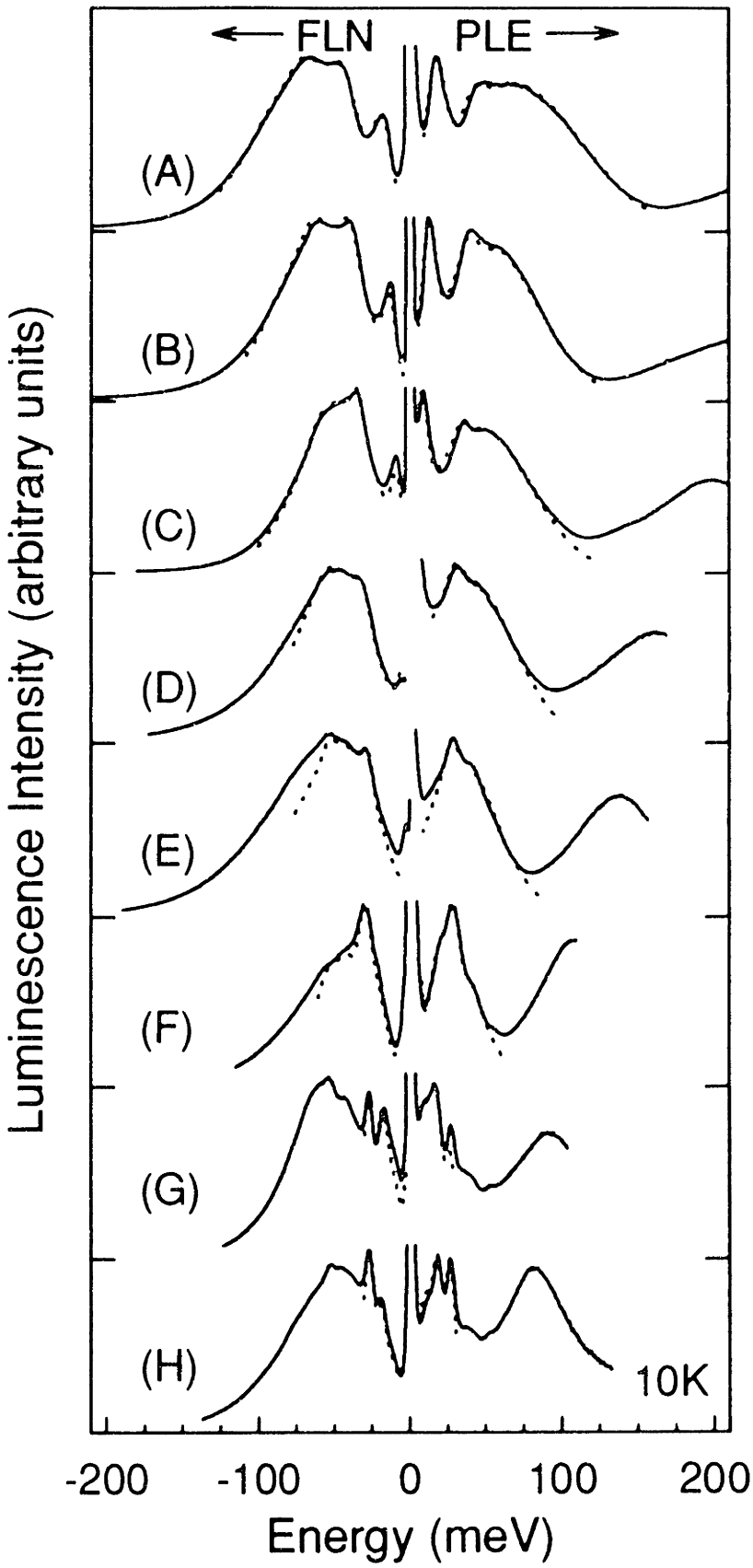
FLN
PLE
(A)
(B)
(C)
(D)
(E)
(F)
(G)
(H)
10K
Luminescence Intensity (arbitrary units)
-200
-100
0
100
200
Energy (meV)

FIG. 6.5 The size dependence of band edge FLN/PLE spectra. In each pair of FLN/PLE results (solid lines) the FLN excitation and the PLE emission energies are identical and indicated by arrows in the full luminescence spectra in Fig. 6.6. For each sample the PLE spectrum with the highest resolution is shown. The FLN (PLE) data are plotted relative to the excitation (emission) energy. Dotted lines show the best fit obtained by the global fitting procedure. For samples A-E nine parameters were adjusted: $\gamma_{1,0}$, $\gamma_{2,0}$, γ_d, ν_o, Δ_1, Δ_2, C_2/C_1, S_a, and S_e. For samples F-H three more parameters were required: $\gamma_{3,0}$, Δ_3, and C_3/C_1. We assume that $\omega_{LO} = 26\text{meV}$,[42] $\gamma_0 = \gamma_{1,0}$,[45] and $\gamma_{n(\ell,m)} = 1.5\,\gamma_{0(\ell,0)}$ for $n \neq 0$ in emission ($m \neq 0$ in absorption).

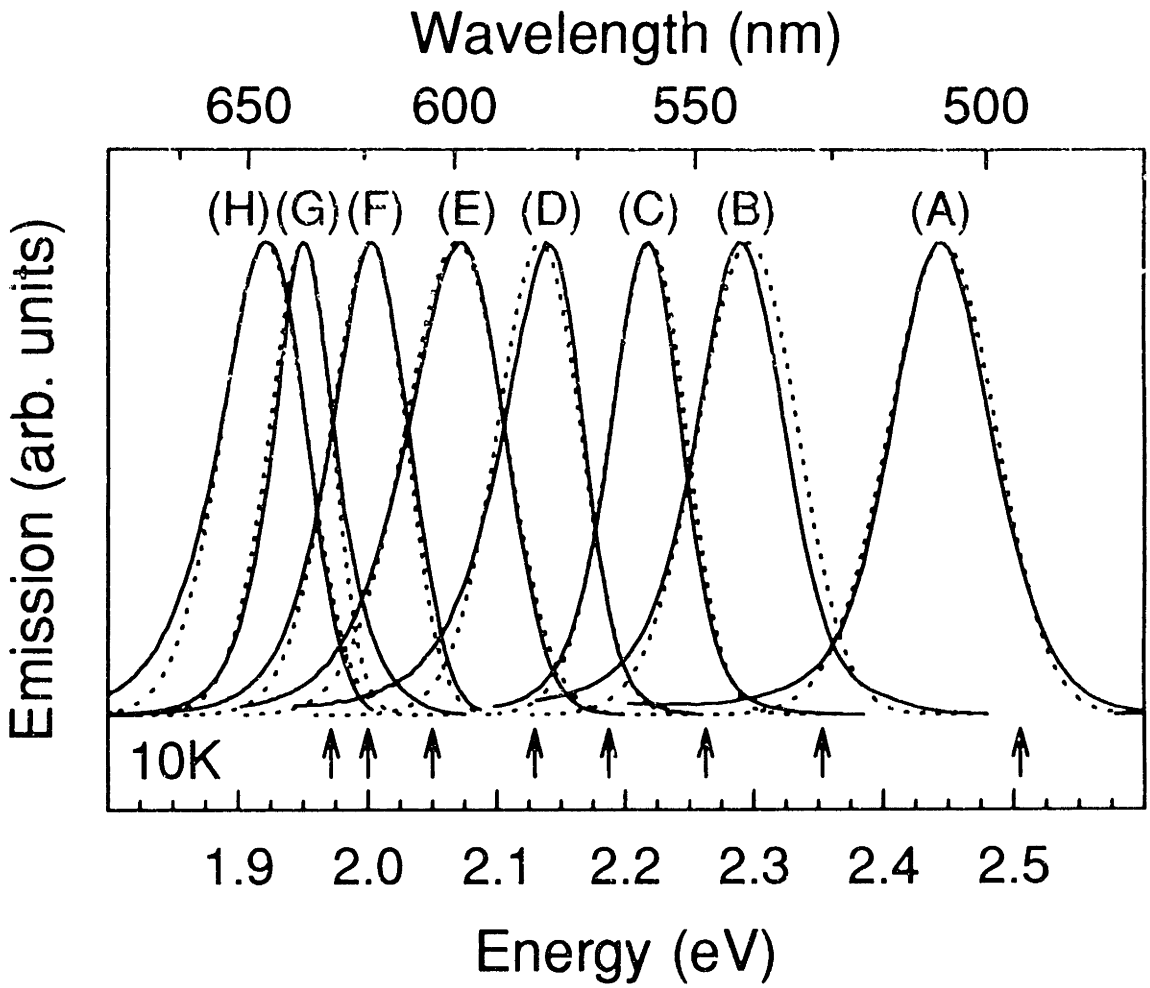

FIG. 6.6 Full luminescence spectra for our size series (solid lines). Arrows indicate the FLN excitation positions and PLE emission positions (eV) used in Fig. 6.5: A) 2.505, B) 2.353, C) 2.263, D) 2.187, E) 2.129, F) 2.050, G) 2.000, and H) 1.971. Dotted lines show the best fit obtained by the global fitting procedure.

From Fig. 6.5 we determine the underlying band edge structure by simulating the FLN and PLE results. The FLN and PLE emission signals (E_{FLN} and E_{PLE}) are convolutions of the single dot absorption cross section (A), the single dot emission lineshape (E), and a probability distribution function (D). D incorporates the various contributions, such as size and shape variations, to the inhomogeneous broadening and indicates what fraction of the sample emits at a particular wavelength. Following Ref. 28 we evaluate the convolution integrals

$$\left.\begin{array}{l} E_{FLN}(\nu_{em})\big|_{\nu_{exc}} \\ E_{PLE}(\nu_{exc})\big|_{\nu_{em}} \end{array}\right\} = C \int A(\nu_{exc},\nu')\, E(\nu_{em},\nu')\, D(\nu',\nu_o)\, d\nu' \qquad (6.1)$$

where the excitation and emission positions (ν_{exc} and ν_{em}) are fixed in FLN and PLE, respectively. C is a constant with the appropriate units which incorporates experimental parameters. We assume that $D(\nu',\nu_o)$ is a normalized Gaussian centered at ν_o with linewidth γ_d, and that

$$A(\nu_{exc},\nu') = \sum_{\ell=1}^{2\text{ or }3} \sum_{m=0}^{2} \frac{C_\ell}{\sqrt{2\pi\gamma_{\ell,m}^2}} \frac{(S_a)^m}{m!} \exp\left(- \frac{\left[\nu_{exc} - (\nu' + \Delta_\ell + m\omega_{LO})\right]^2}{2\gamma_{\ell,m}^2} \right), \qquad (6.2)$$

$$E(\nu_{em},\nu') = \sum_{n=0}^{4} \frac{1}{\sqrt{2\pi\gamma_n^2}} \frac{(S_e)^n}{n!} \exp\left(- \frac{\left[\nu_{em} - (\nu' - n\omega_{LO})\right]^2}{2\gamma_n^2} \right), \qquad (6.3)$$

where ν' is the position of the zero-phonon line in emission. The absorption lineshape includes either 2 (samples A-E) or 3 (F-H) absorbing states, each shifted Δ_ℓ from ν' and with integrated area C_ℓ. Thus Δ_1 is the Stokes shift between the lowest absorbing state and the emitting state. $S_{a(e)}$ is the exciton-LO-phonon coupling strength in absorption (emission) and, assuming a displaced-Harmonic-oscillator model for LO-phonon coupling, is equivalent to the Huang-Rhys parameter.[29,30] We consider the first five (three) LO phonon replicas in emission (absorption), separated by ω_{LO}, the LO phonon frequency. The n^{th} (m^{th}) replica of the emitting (ℓ^{th} absorbing) state has linewidth $\gamma_{n(\ell,m)}$.

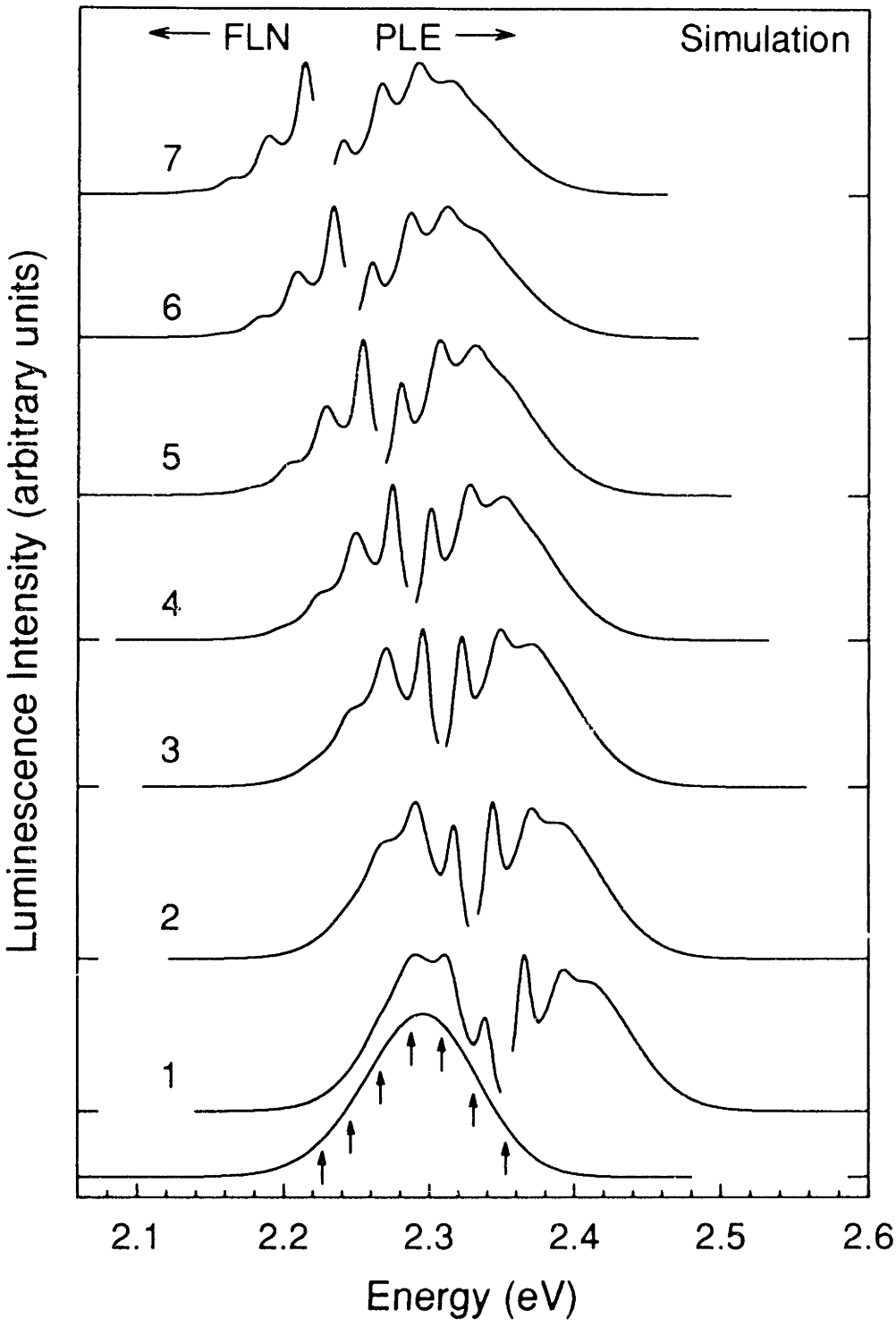

FIG. 6.7 Simulation of FLN/PLE spectra for sample B using the same excitation and emission positions for FLN and PLE as in Fig 6.2. Arrows denote the FLN excitation and PLE emission positions and are shown with the simulated full luminescence.

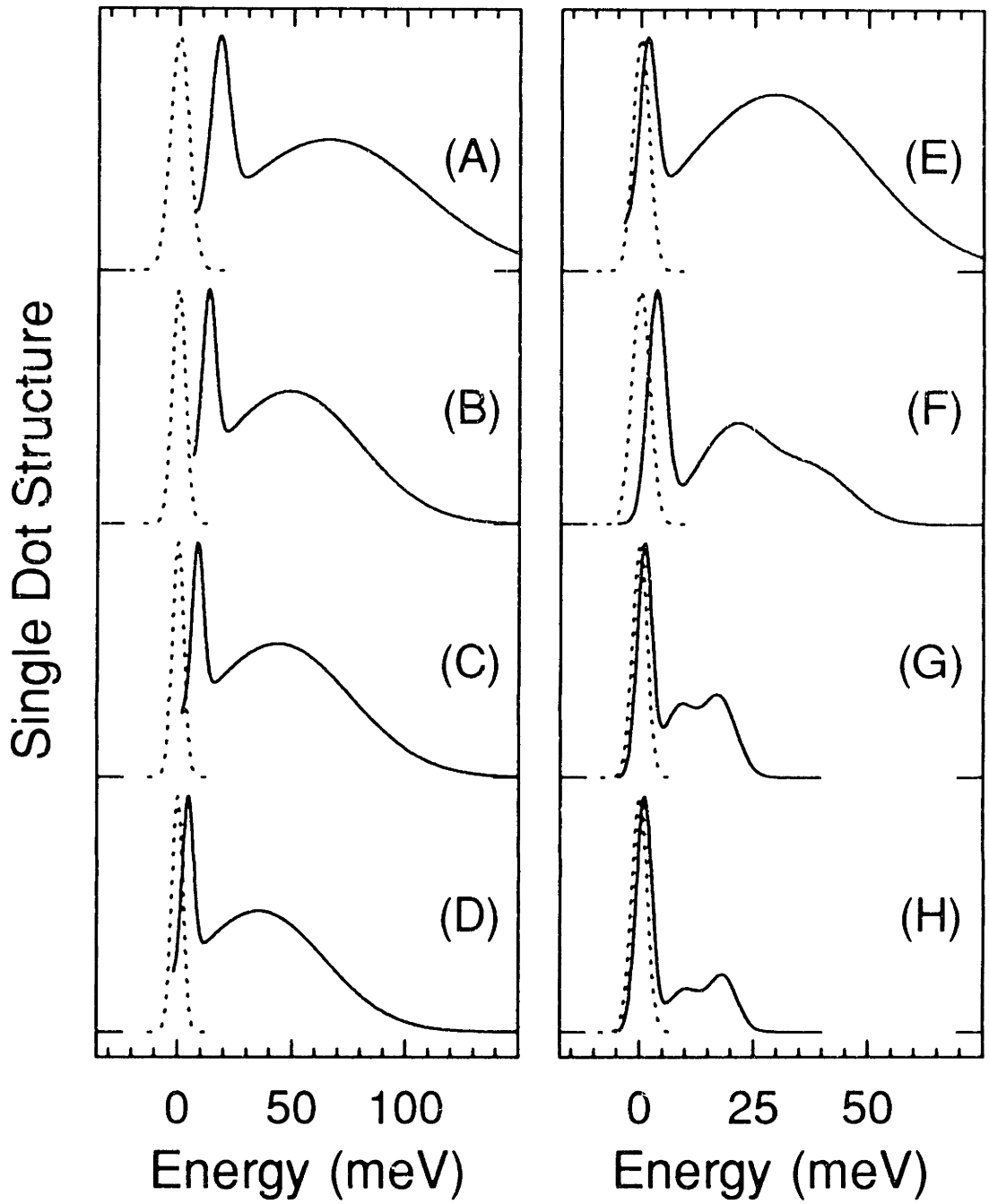

FIG. 6.8 Single dot absorption (solid lines) and emission (dotted lines) structure for samples A-H required to fit the FLN/PLE data in Figs. 6.5 and 6.6. The positions are shown relative to the emitting state. For clarity the LO-phonon replicas are not included. Note the factor of 2 difference in energy axes between samples A-D and E-H.

For each sample we reproduce the FLN, PLE, and full luminescence[31] data from Figs. 6.5 and 6.6 using Eqs. 1-3. The parameters are varied using standard nonlinear least squares methods.[32] The best fits obtained are shown as dotted lines in Figs. 6.5 and 6.6. The complete FLN/PLE data set for each sample can then be simulated and compared with experiment. Figure 6.7 shows the simulated analog of Fig. 6.2, demonstrating that our model can reproduce the trends in both FLN and PLE spectra. From the fitting procedure we extract single dot band edge structures for each sample, shown in Fig. 6.8 without LO-phonon replicas. The position of band edge absorption (solid line) and emission (dotted line) features are plotted relative to the energy of the emitting state. The three absorption features (α, β_1 and β_2) discussed above for sample G are also resolved in samples F and H. In smaller sizes (A-H) only two features (α and β) are observed. The model lineshapes also indicate that with increasing size both the spacing between features and their linewidths decrease dramatically. Note the change in energy scale between samples A-D and E-H in Fig. 6.8.

For clarity Fig. 6.8 does not include LO-phonon coupling. Figure 6.9 shows the model absorption and emission lineshapes for sample B including LO-phonon coupling. As in all of our samples the absorption coupling constant for this sample (S_a=0.12) is significantly smaller than the emission coupling constant (S_e=0.45). For the entire size series S_a ranges between 0.08 and 0.2, consistent with recent Raman studies[33,34] which report S_a (the Huang-Rhys parameter) between 0.125 and 0.275 for CdSe QDs.[34] For the emitting state we find S_e between 0.36 and 0.5. The complete set of model lineshape parameters is summarized in Table 6.I. Sample distribution parameters are summarized in the appendix.

6.4 Discussion

The size dependence of the broad featureless transitions in the optical spectra of CdSe quantum dots[5,10] can be quantitatively described by effective mass models which include the complexity of the CdSe valence band.[6-10] For convenience these models assume spherical dots and work within the spherical band approximation[35,36] since more sophisticated treatments have not been required to explain experimental results. However,

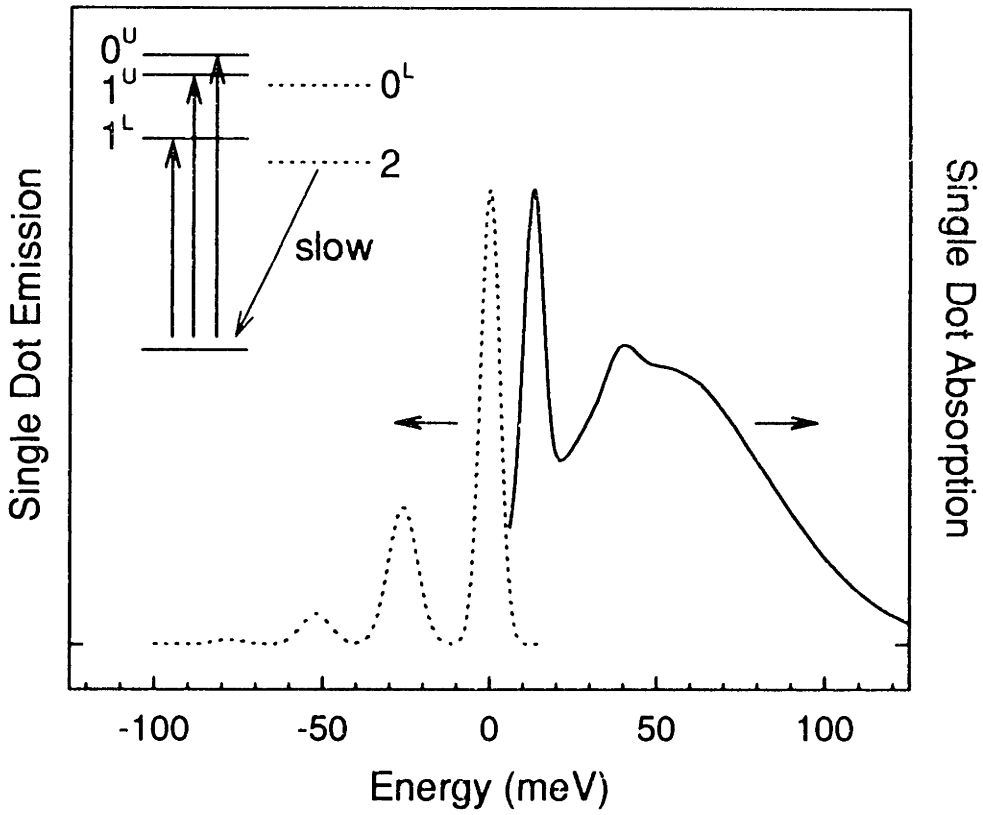

FIG. 6.9 Single dot absorption (solid line) and emission (dotted line) structure for sample B including LO-phonon coupling. An energy level diagram illustrates the band edge exciton structure predicted by Refs. 15 and 16. The sublevels are labeled by $|N_m|$ with superscripts to distinguish upper (U) and lower (L) sublevels with the same $|N_m|$. Optically active (passive) levels are shown as solid (dotted) lines.

Table 6.I. Effective radius and model lineshape parameters for samples A-H and TDA results. The integrated areas (C_i) are shown as percentages of the total band edge oscillator strength.

Sample	a(Å)	S_a	S_ϵ	Δ_1 (meV)	Δ_2 (meV)	Δ_3 (meV)	C_1 (%)	C_2 (%)	C_3 (%)	$\gamma_{1,0}$ (meV)	$\gamma_{2,0}$ (meV)	$\gamma_{3,0}$ (meV)
A	15	0.1	0.5	17.7	65.4	—	10.9	89.1	—	4.0	42	—
B	19	0.12	0.45	13.0	48.6	—	10.6	89.4	—	2.9	31	—
C	21	0.1	0.36	8.4	43.4	—	8.6	91.4	—	2.5	32	—
D	24	0.08	0.4	4.5	35.3	—	10.3	89.7	—	2.4	29	—
E	27	0.12	0.7	1.5	29.5	—	7.8	92.2	—	1.8	20	—
TDA*	30	—	—	2	26	—	17.9	82.1	—	1.7	14.4	—
F	33	0.2	0.5	3.5	20.5	38.5	27.5	47.2	25.3	2.0	8.0	8.0
G	44	0.2	0.4	1.0	8.8	17.6	40.9	27.6	31.5	1.6	3.6	3.6
H	50	0.2	0.4	1.0	10.0	18.6	54.7	23.4	21.9	1.7	4.0	3.0

* TDA data from chapter 4 (Ref. 18)

in this case they predict that the band edge exciton ($1S_{3/2}1S_e$) is 8-fold degenerate. Recent theoretical work[11-16] has extended these models to include the effects of the hexagonal lattice,[11] the nonspherical shape,[12] and the electron-hole exchange interaction.[13,14] When these terms are considered, the initially 8-fold degenerate band edge exciton is split into 5 sublevels.[15,16] For the exchange interaction the important quantum number is the total angular momentum, $N = F_h+F_e$, where F_h (F_e) is the hole (electron) angular momentum. When the crystal field of the hexagonal lattice and/or the nonspherical shape are also included, the good quantum number is the projection of N along the unique crystal axis, N_m. The five sublevels are then labeled by $|N_m|$: one sublevel with $|N_m|=2$, two with $|N_m|=1$, and two with $|N_m|=0$. Levels with $|N_m|>0$ are two-fold degenerate.

This exciton fine structure is illustrated in an energy level diagram in Fig. 6.9. The five sublevels are labeled by $|N_m|$ with superscripts to distinguish upper (U) and lower (L) sublevels with the same $|N_m|$. Only three of the five sublevels are optically active in the electric dipole approximation.[15,16] The lowest band edge state, $|N_m|=2$, is forbidden and is referred to as the "dark exciton". Relaxation of the electron-hole pair into this state can explain the long radiative lifetimes observed in CdSe quantum dots,[15] previously attributed to surface traps.[22,37-40] Since two units of angular momentum are required to return to the ground state from the $|N_m|=2$ sublevel, this transition is one-photon forbidden. However, less efficient, phonon-assisted transitions can occur, rationalizing the stronger LO phonon coupling of the emitting state (S_e) and the long radiative lifetimes (at 10K).[15]

In chapter 4 we showed that band edge absorption structure in TDA experiments is consistent with predicted band edge exciton splittings.[18] We observed both narrow (α) and broad (β) absorption features in the TDA spectrum. α was assigned to the lowest allowed transition, 1^L, and β to a combination of 1^U and 0^U. The emitting state was assigned to the "dark exciton". The assignment of β to a combination of 1^U and 0^U is further supported by the FLN/PLE results of this chapter. In larger samples (F-H) β_1 and β_2 can be assigned to the individual 1^U and 0^U sublevels, previously unresolved.

To test these assignments more quantitatively Fig. 6.10a shows the calculated band edge structure vs. effective radius using the theory of Refs. 15 and 16 (see chapter 4). For

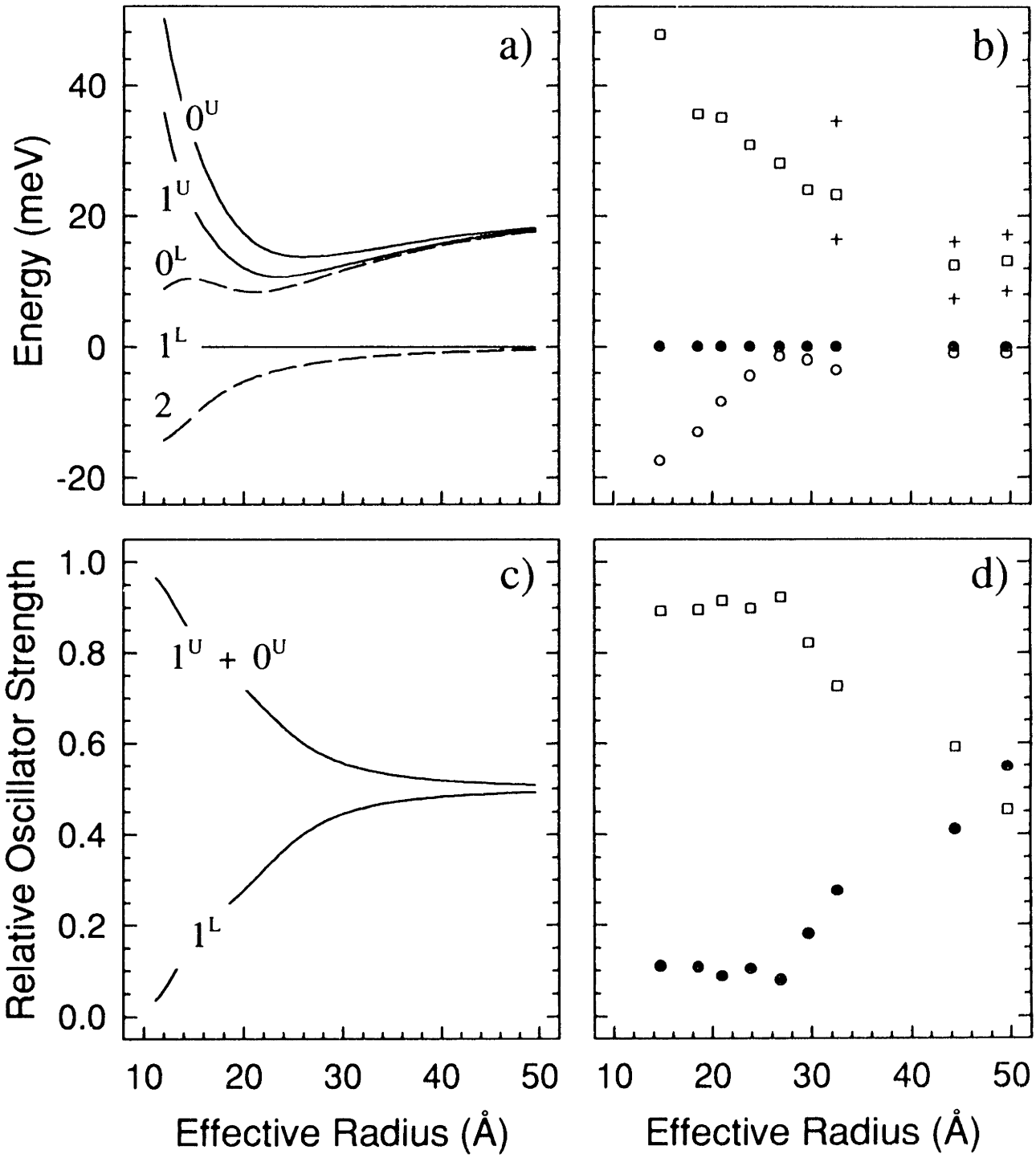
a)
b)
c)
d)
Energy (meV)
40
20
0
-20
0^U
1^U
0^L
1^L
2
Relative Oscillator Strength
1.0
0.8
0.6
0.4
0.2
0.0
$1^U + 0^U$
1^L
10
20
30
40
50
Effective Radius (Å)
Effective Radius (Å)

FIG. 6.10 (a) The band edge exciton ($1S_{3/2}1S_e$) structure vs. effective radius calculated from Ref. 16. The sublevels are labeled by $|N_m|$ with superscripts to distinguish upper (U) and lower (L) sublevels with the same $|N_m|$. Positions are relative to 1^L. Optically active (passive) levels are shown as solid (dashed) lines. (b) Position of the absorbing (• and □) and emitting (o) features from Fig. 6.8 and TDA results from Ref. 18. In samples F-H both the positions of β_1 and β_2 (+) and their weighted average (□) are shown. (c) Calculated relative oscillator strength of the optically allowed band edge sublevels vs. effective radius. The combined strength of 1^U and 0^U is shown. (d) Observed relative oscillator strength of the band edge sublevels: 1^L (•) and the combined strength of 1^U and 0^U (□).

this calculation we use literature values for the bulk A-B splitting (25 meV[41]), the bulk exchange splitting (0.13 meV[42]), the exciton Bohr radius (56Å[10]), and the aspect ratio vs. size.[43] The sublevels are plotted relative to the energy of 1^L. Optically active and passive levels are shown as solid and dashed lines, respectively. In large dots the sublevels converge to two 4-fold degenerate states, analogous to the bulk A and B excitons. In this limit these two states are split by the combined effect of the crystal field and the non-spherical shape of the dot. As the size of the dot decreases the exchange interaction is enhanced due to quantum confinement and the sublevels fan out. Figure 6.10b shows the position of the absorbing (• and ▯) and emitting (o) features from Fig. 6.8 and TDA results,[18] relative to the narrow absorption feature α (1^L). For samples F-H both the positions of β_1 and β_2 (+) and their weighted average (▯) are shown. Comparison with theory indicates that the model accurately reproduces many aspects of the data. Both the splitting between $|N_m|=2$ and 1^L (the Stokes shift) and the splitting between 1^L and the upper states (1^U and 0^U) are described reasonably well. This result is particularly significant since, although the predicted structure strongly depends on the theoretical input parameters,[15] only literature values were used in the theoretical calculation.

The predicted structure in Fig. 6.10a also helps rationalize why the 1^U and 0^U sublevels are not resolved in smaller dots (A-H). Previously we speculated (see chapter 4) that these features were much broader than 1^L due to lifetime effects and inhomogeneous broadening.[18] Lifetime broadening occurs in 1^U and 0^U since these levels each have a rapid relaxation pathway via 1^L and 0^L, respectively, while 1^L can relax only through a much slower spin-flip mechanism. However, since we do not expect the lifetime of the upper states (1^U and 0^U) to increase with increasing size, this mechanism cannot explain the decrease in their linewidths in large dots. According to Fig. 6.10a, inhomogeneous broadening can provide an explanation. The spacing between the emitting state and the upper states (1^U and 0^U) becomes less size dependent as the size is increased. Therefore, since size and shape distributions in our samples are fairly constant with size,[21] we expect inhomogeneous broadening of the upper states to decrease with size, becoming negligible in the largest dots. When this effect is combined with the general increase in

homogeneous linewidth of all absorption and emission features with decreasing size,[44,45] it is not surprising that 1^U and 0^U are only resolved in the largest dots.

Further quantitative evidence for our assignments is shown in Figures 6.10c and 6.10d, which compare theoretical and experimental values for the relative oscillator strength of the optically allowed sublevels.[15,16] In the theoretical plot the combined strength of the upper states (1^U and 0^U) is shown since these states are not individually resolved in many of our samples. Reasonable agreement between experiment and theory is observed. To understand the results we can consider two opposing limits. In large dots the states converge to A- and B-like excitons (as in Fig. 6.10a), each possessing half of the total band edge oscillator strength. Therefore, we expect 1^L and the combined upper states to each approach 0.5 in large sizes. In small dots the exchange interaction dominates and the crystal field and nonspherical shape effects become negligible. In this case the sublevels converge to two states labeled by the total angular momentum N: an optically forbidden 5-fold degenerate $N = 2$ state, and an optically allowed 3-fold degenerate $N = 1$ state. Since 1^L converges to the $N = 2$ state, we expect it to be only weakly allowed in small dots. 1^U and 0^U converge to the $N = 1$ state and therefore carry nearly all of the oscillator strength.

The agreement between experiment and theory in Fig. 6.10 indicates that our FLN and PLE results support the predicted band edge exciton fine structure. However, our results also demonstrate where theory may be improved. The model clearly fails to predict the observed splitting between 1^U and 0^U in large dots (Fig. 6.10b). In this size regime theoretical levels have already converged to the A- and B-like excitons. While this discrepancy would appear to indicate that theory underestimates the exchange splitting, a change in this parameter would also affect the Stokes shift, which is well described by the model. Further theoretical work is required to address this issue.

6.5 Conclusion

In this chapter we present photoluminescence excitation (PLE) and fluorescence line narrowing (FLN) results which exhibit structure within the first absorption feature of CdSe quantum dots. We study the size dependence of this structure by examining 8 CdSe

samples ranging from ~15Å to ~50Å in mean effective radius. Band edge exciton splittings have been predicted as a result of the hexagonal lattice and non-spherical shape of our dots as well as the electron-hole exchange interaction. To compare with these theories we extract single dot absorption and emission lineshapes from our data. We find that theory agrees well with the position and relative strengths of the absorption features in our model lineshapes, supporting our previous claim that band edge exciton fine structure is observed in these samples.

6.6 References:

1. Al. L. Efros and A. L. Efros, Fiz. Tekh. Poluprovodn. **16**, 1209 (1982) [Sov. Phys. Semicond. **16**, 772 (1982)].
2. L. E. Brus, J. Chem. Phys. **80**, 4403 (1984).
3. For a review see L. E. Brus, Appl. Phys. A **53**, 465 (1991).
4. C. B. Murray, D. J. Norris and M. G. Bawendi, J. Am. Chem. Soc. **115**, 8706 (1993).
5. D. J. Norris, A. Sacra, C. B. Murray, and M. G. Bawendi, Phys. Rev. Lett. **72**, 2612 (1994); D. J. Norris and M. G. Bawendi, Phys. Rev. B (submitted).
6. J. B. Xia, Phys. Rev. B **40**, 8500 (1989).
7. G. B. Grigoryan, E. M. Kazaryan, Al. L. Efros and T. V. Yazeva, Fiz. Tverd. Tela **32**, 1772 (1990) [Sov. Phys. Solid State **32**, 1031 (1990)].
8. K. J. Vahala and P. C. Sercel, Phys. Rev. Lett. **65**, 239 (1990); P. C. Sercel and K. J. Vahala, Phys. Rev. B **42**, 3690 (1990).
9. S. W. Koch, Y. Z. Hu, B. Fluegel and N. Peyghambarian, J. Crystal Growth **117**, 592 (1992).
10. A. I. Ekimov, F. Hache, M. C. Schanne-Klein, D. Ricard, C. Flytzanis, I. A. Kudryavtsev, T. V. Yazeva, A. V. Rodina, and Al. L. Efros, J. Opt. Soc. Am. B **10**, 100 (1993).
11. Al. L. Efros, Phys. Rev. B **46**, 7448 (1992).
12. Al. L. Efros and A. V. Rodina, Phys. Rev. B **47**, 10005 (1993).
13. S. Nomura, Y. Segawa and T. Kobayashi, Phys. Rev. B **49**, 13571 (1994).
14. M. Chamarro, C. Gourdon, P. Lavallard and A. I. Ekimov, Jpn. J. Appl. Phys. **34**, Suppl. 34-1, 12 (1995).
15. M. Nirmal, D. J. Norris, M. Kuno, M. G. Bawendi, Al. L. Efros, and M. Rosen (submitted).
16. Al. L. Efros, M. Rosen, M. Kuno, M. Nirmal, D. J. Norris, and M. G. Bawendi (in preparation).
17. Sizes reported are estimated from extensive size dependent transmission electron microscopy (TEM) and small angle x-ray measurements and are based on the energy of the first absorption peak. We report the effective radius of our prolate dots, defined as $a = [(b^2\ c)^{1/3}]/2$ where b (c) is the short (long) axis.
18. D. J. Norris and M. G. Bawendi, J. Chem. Phys. (in press).
19. L. R. Becerra, C. B. Murray, R. G. Griffin, and M. G. Bawendi, J. Chem. Phys. **100**, 3297 (1994).
20. J. E. Bowen Katari, V. L. Colvin, and A. P. Alivisatos, J. Phys. Chem. **98**, 4109 (1994).
21. C. B. Murray, Ph.D. Thesis, Massachusetts Institute of Technology, 1995.
22. M. G. Bawendi, W. L. Wilson, L. Rothberg, P. J. Carroll, T. M. Jedju, M. L. Steigerwald, and L. E. Brus, Phys. Rev. Lett. **65**, 1623 (1990).
23. W. Hoheisel, V. L. Colvin, C. S. Johnson, and A. P. Alivisatos, J. Chem. Phys. **101**, 8455 (1994).
24. C. R. M. de Oliveira, A. M. de Paula, F. O. Plentz Filho, J. A. Medeiros Neto, L. C. Barbosa, O. L. Alves, E. A. Menezes, J. M. M. Rios, H. L. Fragnito, C. H. Brito Cruz, and C. L. Cesar, Appl. Phys. Lett. **66**, 439 (1995).
25. P. A. M. Rodrigues, G. Tamulaitis, P. Y. Yu, and S. H. Risbud, Solid State Commun. (in press).

26. By single dot lineshape we mean the lineshape required by each dot in our model to reproduce the PLE and FLN results. The band edge structure in this lineshape may be an upper bound to the true structure if multiple inhomogeneities are present, not all of which are removed by experiment.
27. In addition to size, other inhomogeneities may influence the energy of the band edge exciton. We include these here in the descriptions "smallest" or "largest".
28. M. Nirmal, C. B. Murray, and M. G. Bawendi, Phys. Rev. B **50**, 2293 (1994).
29. S. Schmitt-Rink, D. A. B. Miller, and D. S. Chemla, Phys. Rev. B **35**, 8113 (1987).
30. M. C. Klein, F. Hache, D. Ricard, and C. Flytzanis, Phys. Rev. B **42**, 11123 (1990).
31. Full luminescence is simulated by setting $A(\nu_{ex}, \nu')$ constant in Eq. (1).
32. W. H. Press, B. P. Flannery, S. A. Teukolsky, and W. T. Vetterling, *Numerical Recipes in C* (Cambridge University Press, Cambridge, 1988), Chapter 14.
33. J. J. Shiang, S. H. Risbud, and A. P. Alivisatos, J. Chem. Phys. **98**, 8432 (1993).
34. J. J. Shiang, R. K. Grubbs, and A. P. Alivisatos, Phys. Rev. B (in press); J. J. Shiang, A. P. Alivisatos, K. B. Whaley, Phys. Rev. B (in press).
35. A. Baldereschi and N. O. Lipari, Phys. Rev. B **8**, 2697 (1973).
36. In the spherical band approximation, outlined in Ref. 35 for the charged impurity problem, only terms of spherical symmetry in the Luttinger Hamiltonian are considered in first order.
37. M. O'Neil, J. Marohn, and G. McLendon, J. Phys. Chem. **94**, 4356 (1990).
38. A. Eychmüller, A. Hässelbarth, L. Katsikas, and H. Weller, Ber. Bunsenges. Phys. Chem. **95**, 79 (1991).
39. A. Hässelbarth, A. Eychmüller, and H. Weller, Chem. Phys. Lett. **203**, 271 (1993).
40. M. G. Bawendi, P. J. Carroll, W. L. Wilson, and L. E. Brus, J. Chem. Phys. **96**, 946 (1992).
41. *Landolt-Bornstein Numerical Data and Functional Relationships in Science and Technology*, New Series, Group III, Vol. 17b, edited by K. H. Hellwege (Springer-Verlag, Berlin, 1982).
42. V. P. Kochereshko, G. V. Mikhailov, and I. N. Ural'tsev, Fiz. Tverd. Tela **25**, 769 (1983) [Sov. Phys. Solid State **25**, 439 (1983)].
43. Size dependent aspect ratio measurements from Ref. 21 are fit to a polynomial.
44. D. M. Mittleman, R. W. Schoenlein, J. J. Shiang, V. L. Colvin, A. P. Alivisatos, and C. V. Shank, Phys. Rev. B **49**, 14435 (1994); R. W. Schoenlein, D. M. Mittleman, J. J. Shiang, A. P. Alivisatos, and C. V. Shank, Phys. Rev. Lett. **70**, 1014 (1993).
45. D. J. Norris, M. Nirmal, C. B. Murray, A. Sacra, and M. G. Bawendi, Z. Phys. D **26**, 355 (1993).

6.7 Appendix

6.7.1 Tables:

Table 6A.I Effective radius (a), approximate 1st absorption peak maximum at room temperature, and sample distribution parameters for samples A-H. For each sample, the sample distribution center (ν_o) and linewidth (γ_d) are those obtained from the fitting procedure in chapter 6. We note that the Gaussian linewidths presented are standard deviations (as in Eqs. 6.2 and 6.3). The full width at half maximum of the Gaussian linewidths is 2.36 larger.

Sample	a (Å)	1st Absorption Peak Max (RT)	ν_o (eV)	γ_d (meV)
A	15	~510nm	2.4565	37.3
B	19	~542nm	2.3051	35
C	21	~562nm	2.2250	26
D	24	~584nm	2.1409	28.8
E	27	~604nm	2.0830	33
F	33	~628nm	2.0100	24
G	44	~650nm	1.9550	20
H	50	~656nm	1.9280	29

6.7.2 Figures:

Below the complete set of FLN/PLE data for each of the eight samples (A-H) analyzed in chapter 6 is presented. All optical data are obtained at 10K.

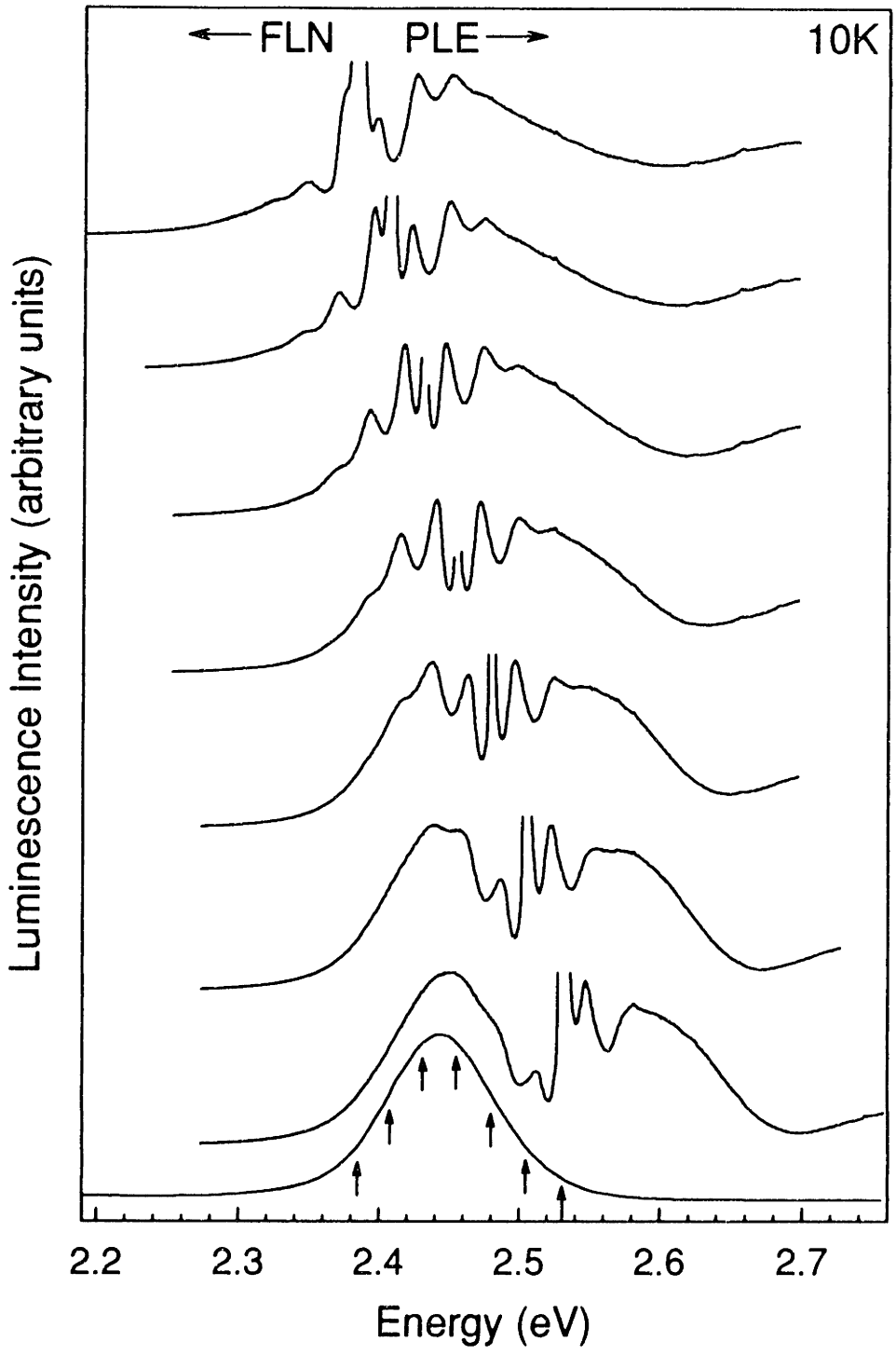

FIG. 6A.1 Normalized PLE and FLN data for sample A (~15Å effective radius) for various emission and excitation positions. For each FLN/PLE pair, the PLE emission and FLN excitation energies are identical. These energies are designated by arrows and shown with the full luminescence.

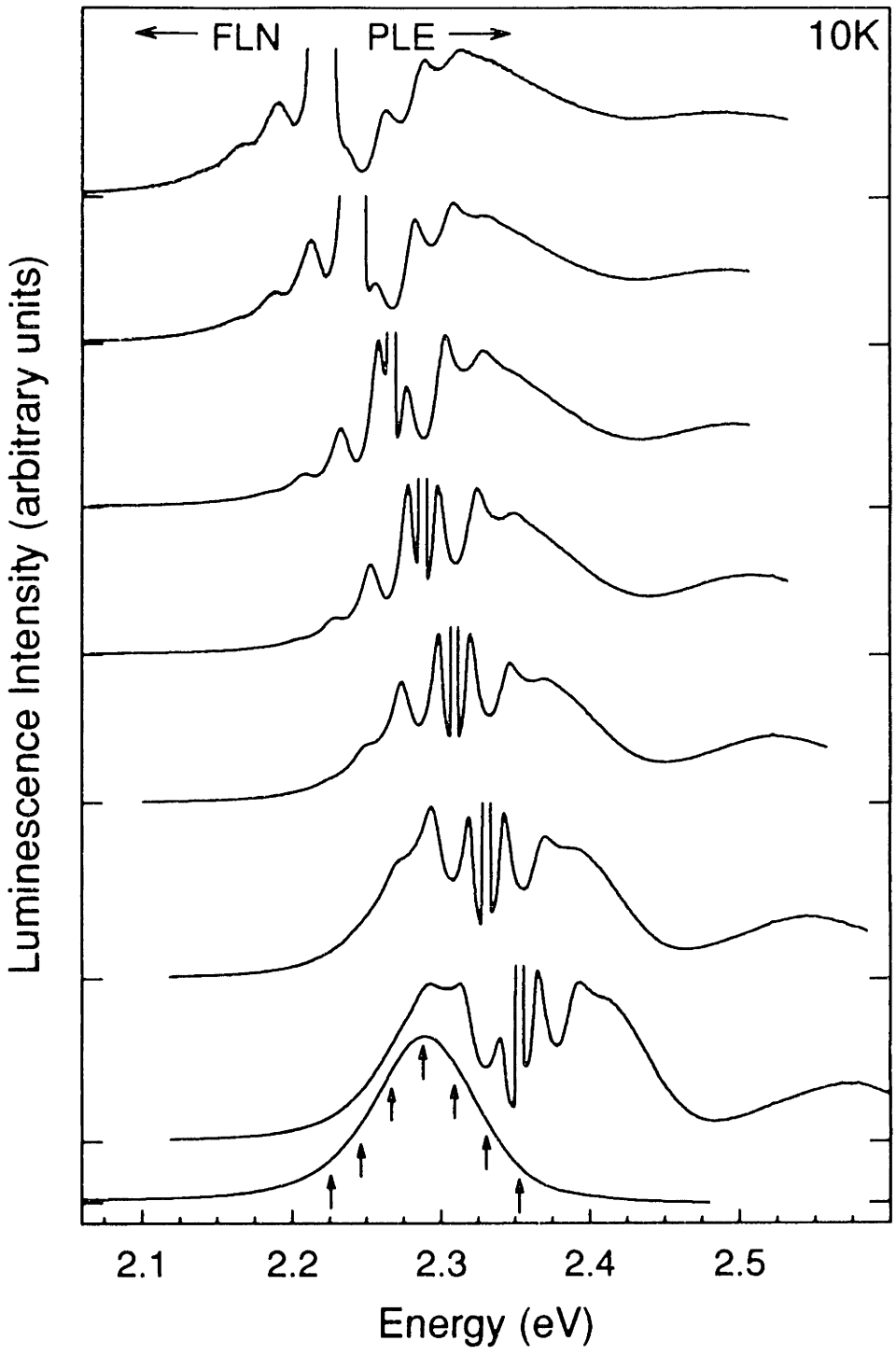

FIG. 6A.2 Normalized PLE and FLN data for sample B (~19Å effective radius) for various emission and excitation positions. For each FLN/PLE pair, the PLE emission and FLN excitation energies are identical. These energies are designated by arrows and shown with the full luminescence.

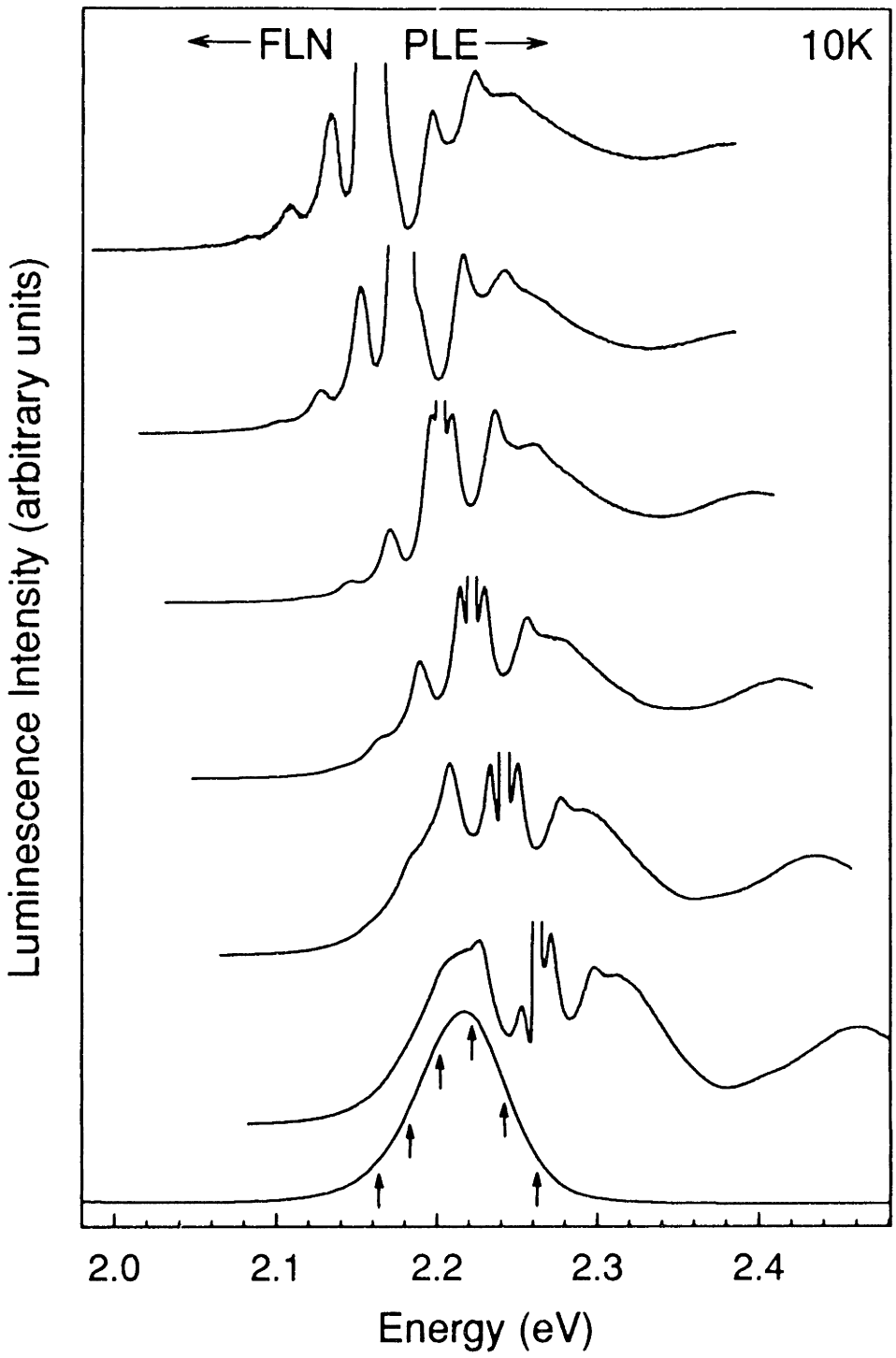

FIG. 6A.3 Normalized PLE and FLN data for sample C (~21Å effective radius) for various emission and excitation positions. For each FLN/PLE pair, the PLE emission and FLN excitation energies are identical. These energies are designated by arrows and shown with the full luminescence.

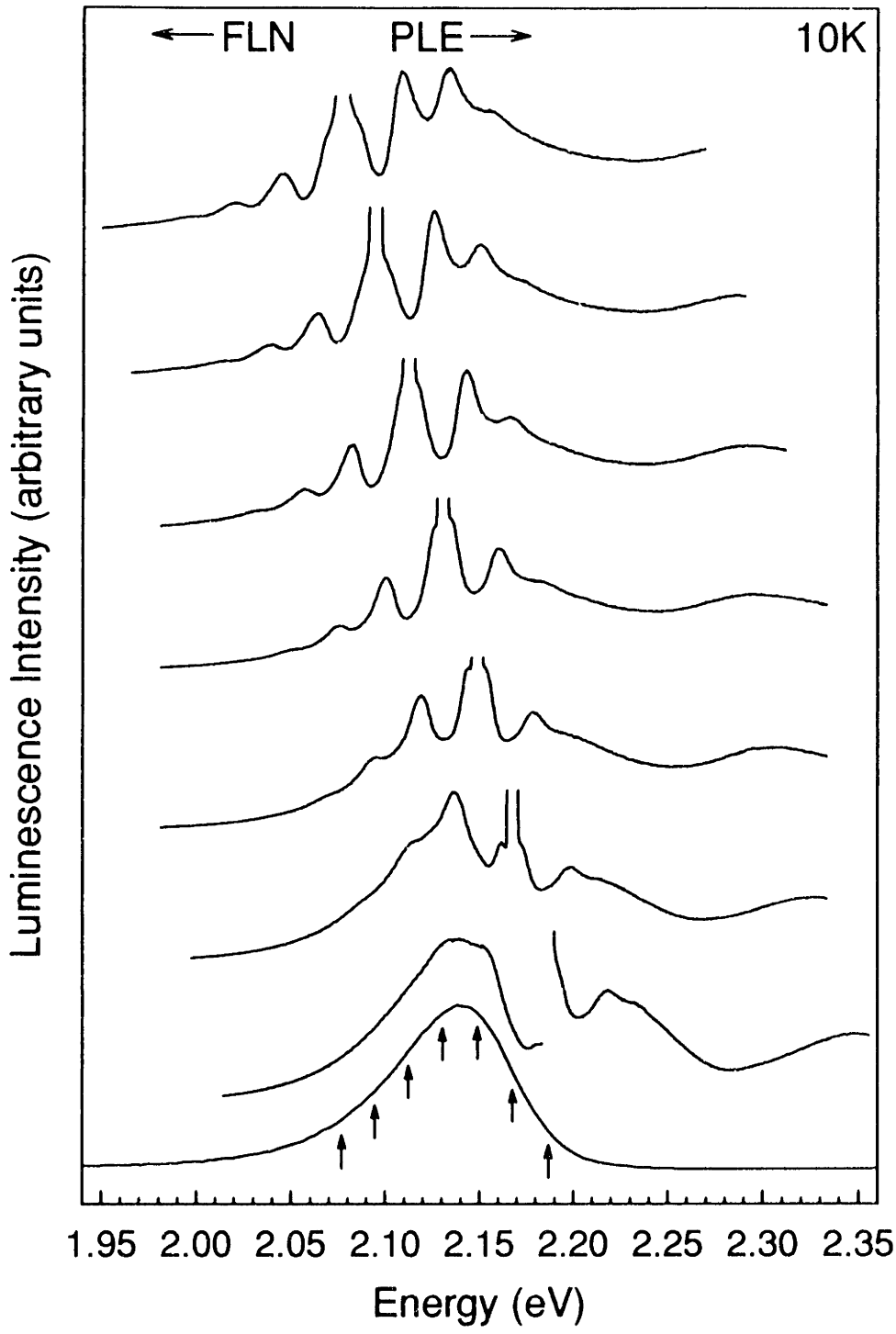

FIG. 6A.4 Normalized PLE and FLN data for sample D (~24Å effective radius) for various emission and excitation positions. For each FLN/PLE pair, the PLE emission and FLN excitation energies are identical. These energies are designated by arrows and shown with the full luminescence.

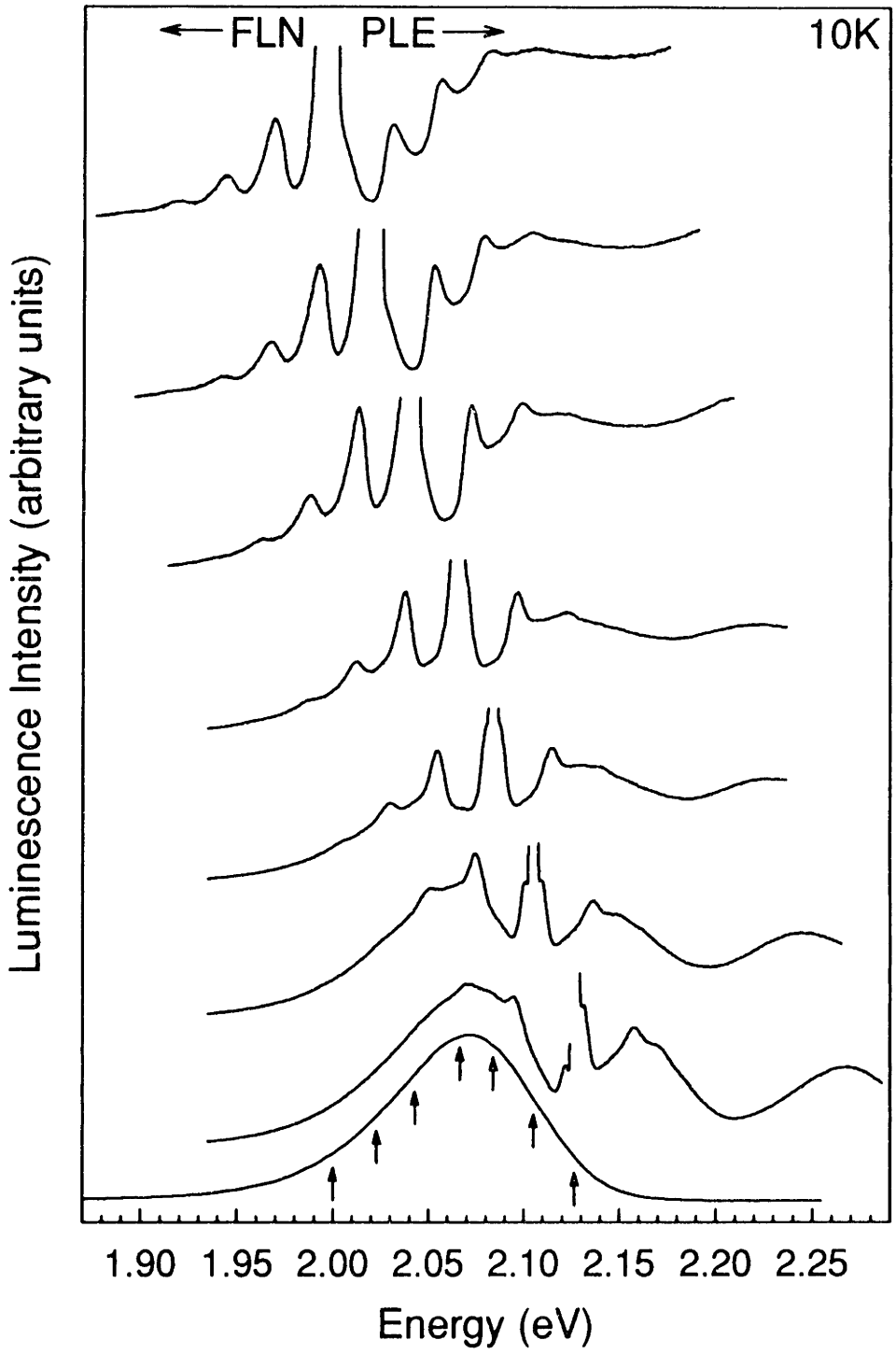

FIG. 6A.5 Normalized PLE and FLN data for sample E (~27Å effective radius) for various emission and excitation positions. For each FLN/PLE pair, the PLE emission and FLN excitation energies are identical. These energies are designated by arrows and shown with the full luminescence.

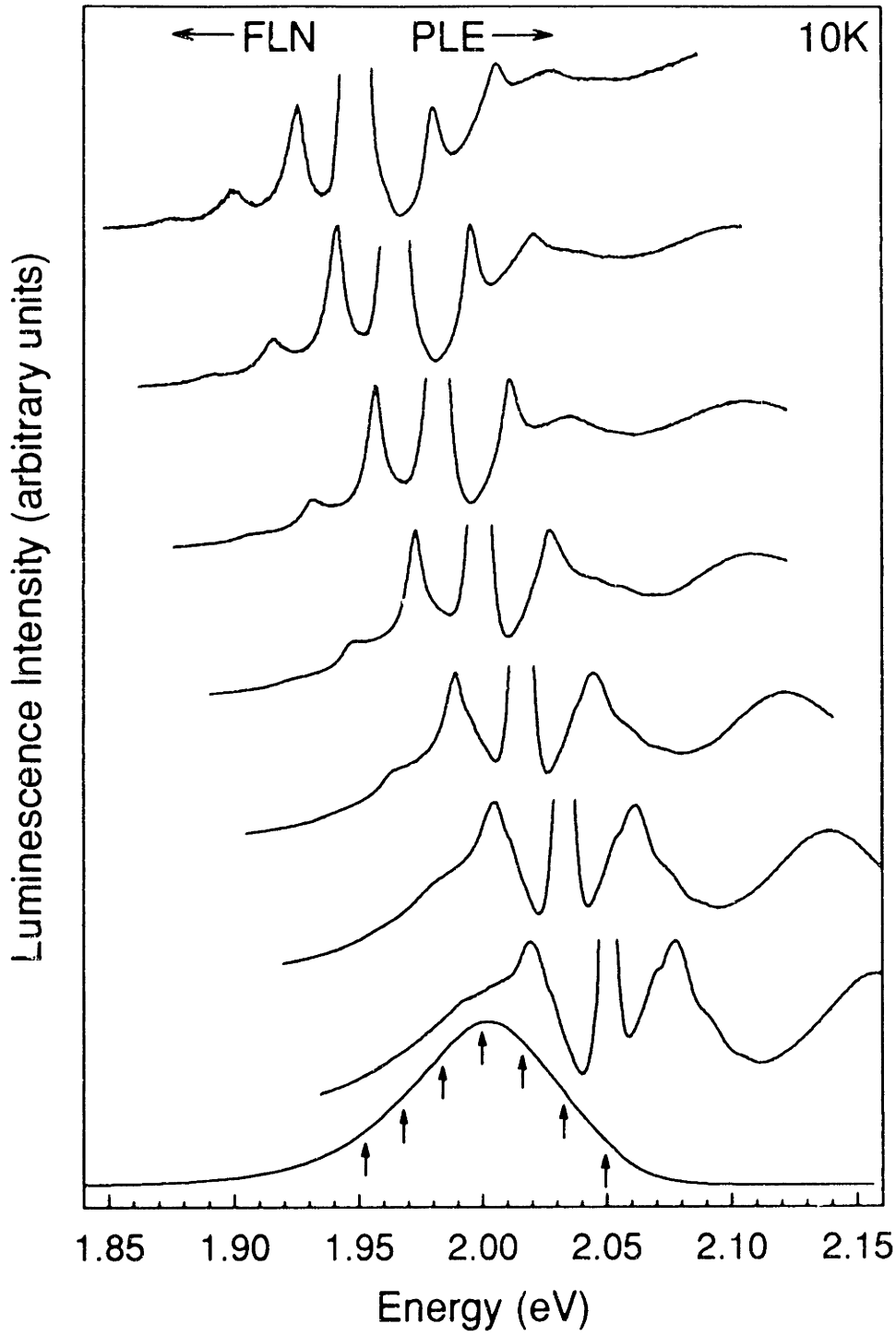

FIG. 6A.6 Normalized PLE and FLN data for sample F (~33Å effective radius) for various emission and excitation positions. For each FLN/PLE pair, the PLE emission and FLN excitation energies are identical. These energies are designated by arrows and shown with the full luminescence.

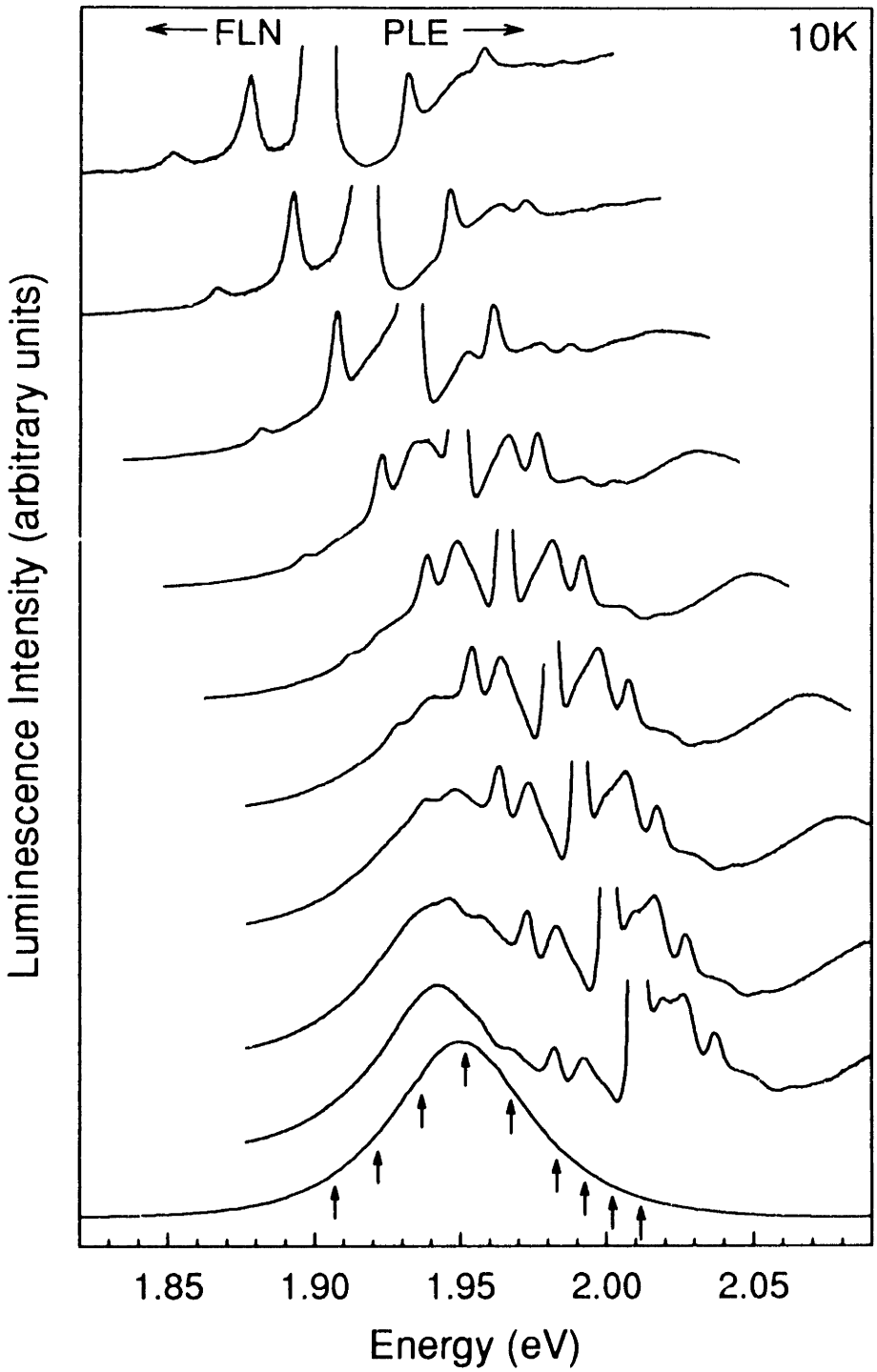

FIG. 6A.7 Normalized PLE and FLN data for sample G (~44Å effective radius) for various emission and excitation positions. For each FLN/PLE pair, the PLE emission and FLN excitation energies are identical. These energies are designated by arrows and shown with the full luminescence.

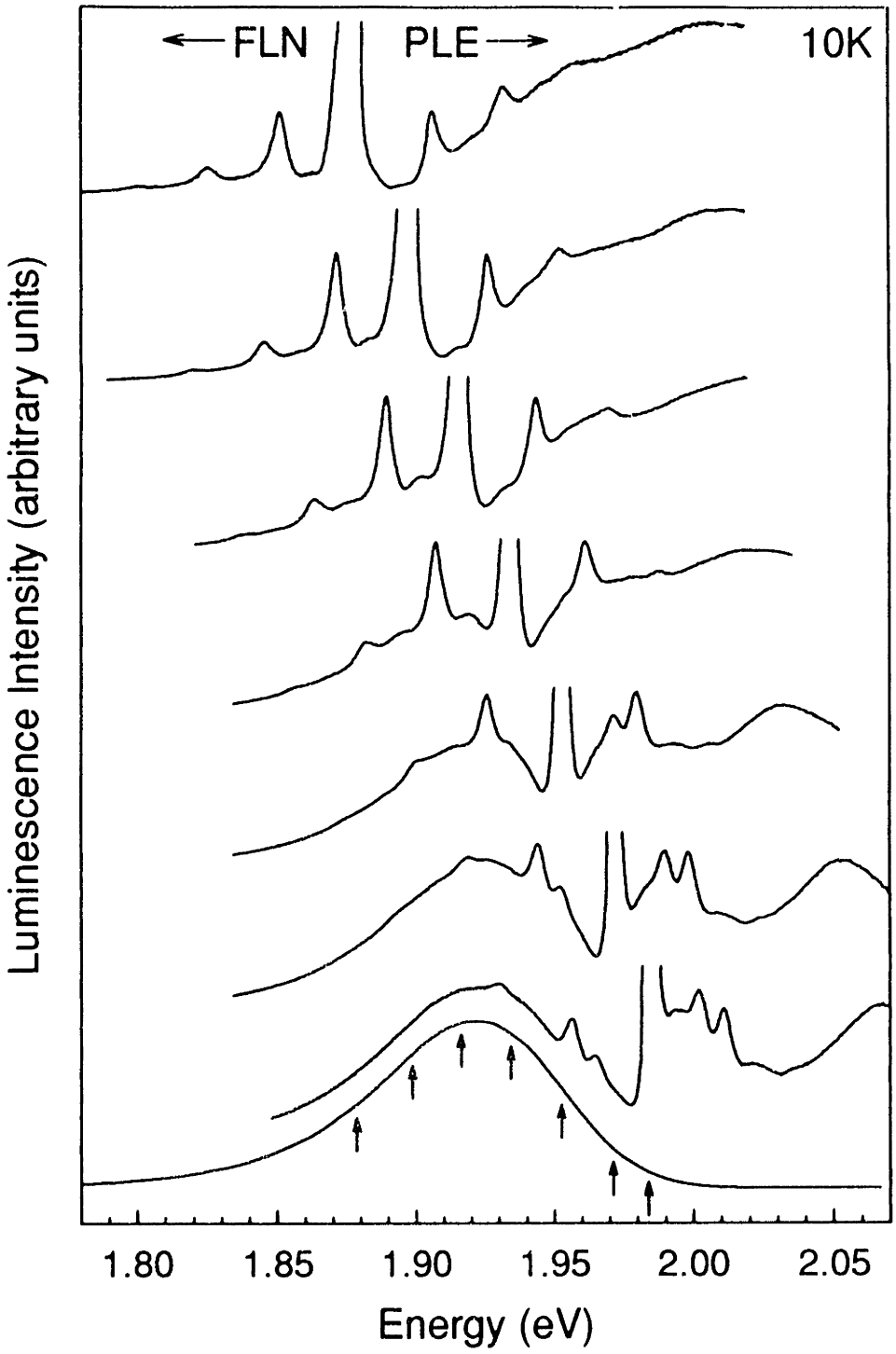

FIG. 6A.8 Normalized PLE and FLN data for sample H (~50Å effective radius) for various emission and excitation positions. For each FLN/PLE pair, the PLE emission and FLN excitation energies are identical. These energies are designated by arrows and shown with the full luminescence.

List of Publications

1. "Size Dependence of Exciton Fine Structure in CdSe Quantum Dots",
   D. J. Norris, Al. L. Efros, M. Rosen, and M. G. Bawendi; *Phys. Rev. B* (submitted).

2. "Measurement and Assignment of the Size-Dependent Optical Spectrum in CdSe Quantum Dots",
   D. J. Norris and M. G. Bawendi; *Phys. Rev. B* (submitted).

3. "Observation of the 'Dark Exciton' in CdSe Quantum Dots",
   M. Nirmal, D. J. Norris, M. Kuno, M. G. Bawendi, Al. L. Efros, and M. Rosen; *Phys. Rev. Lett.* (submitted).

4. "Structure in the Lowest Absorption Feature of CdSe Quantum Dots",
   D. J. Norris and M. G. Bawendi; *J. Chem. Phys.* (in press).

5. "Stark Spectroscopy of CdSe Nanocrystallites: The Significance of Transition Linewidths",
   A. Sacra, D. J. Norris, C. B. Murray, and M. G. Bawendi; *J. Chem. Phys.* (in press).

6. "Measurement of the Size Dependent Hole Spectrum in CdSe Quantum Dots",
   D. J. Norris, A. Sacra, C. B. Murray, and M. G. Bawendi; *Phys. Rev. Lett.* **72**, 2612 (1994).

7. "Synthesis and Characterization of Nearly Monodisperse CdE (E = S, Se, Te) Semiconductor Nanocrystallites",
   C. B. Murray, D. J. Norris, and M. G. Bawendi; *J. Am. Chem. Soc.* **115**, 8706 (1993).

8. "Size Dependent Optical Spectroscopy of II-VI Semiconductor Nanocrystallites (Quantum Dots)",
   D. J. Norris, M. Nirmal, C. B. Murray, A. Sacra, and M. G. Bawendi; *Z. Phys. D* **26**, 355 (1993).

9. "Surface Electronic Properties of CdSe Nanocrystallites",
   M. Nirmal, C. B. Murray, D. J. Norris, and M. G. Bawendi; *Z. Phys. D* **26**, 361 (1993).

10. "Synthesis and Structural Characterization of II-VI Semiconductor Nanocrystallites (Quantum Dots)",
    C. B. Murray, M. Nirmal, D. J. Norris, and M. G. Bawendi; *Z. Phys. D* **26S**, 231 (1993).

11. "Size-Dependent Spectroscopy and Photodynamics of Some II-VI Semiconductor Nanocrystallites (Quantum Dots)",
    M. Nirmal, C. B. Murray, D. J. Norris, and M. G. Bawendi; *Proc. SPIE - Int. Soc. Opt. Eng.* **1861**, 280 (1993).

Acknowledgment

This thesis would not have been possible without the continuous and unwavering support of my wife, Elizabeth. Always an encouragement in my efforts, she has selflessly endured many, many weekends and evenings alone, short vacations, and a student's stipend. She has never questioned my sanity and has learned to accept that "30 minutes" really means two hours. For her self-sacrifice I am deeply grateful.

I have also been fortunate to be among the first graduate students to work with my thesis advisor, Moungi Bawendi. Five years ago when considering research groups, Moungi advised me to consider the dangers of working for an Assistant Professor. I believe that this honest advice, which came from someone who at that time badly needed graduate students, is typical of Moungi's concern for his students. I have never regretted my decision to take the "risk" and feel that the education, training, and scientific philosophy which I have acquired in his group is all that I could have hoped for. For Moungi's time, patience, and concern I am thankful.

I would also like to thank my dear friend Sasha Efros at NRL. Not only has he helped ensure that the explanations of our results are "in the golf field", but he has been an invaluable resource and friend during my graduate education.

As for my fellow graduate students, long hours in lab have been made shorter by my fellow classmates and friends, Chris Murray and Manoj Nirmal. And by Bashir Dabbousi, Cherie Kagan, Ann Sacra, Ken Kuno, Fred Mikulec, and Steve Empedocles. I am grateful for the extensive help that I received with sample preparation, particularly from Chris, but also from Manoj, Ann, Bashir, Ken, and Eric Lee. I also thank Ann for pointing out many errors in my analysis.

Finally, I would like to acknowledge the National Science Foundation and Arthur D. Little for pre-doctoral fellowships.

Top Ten Quotes Overheard in Grad School:

10. "Institute Holiday? Oh, you mean no classes, right?"

9. "Maybe it'll help if you write down the Luttinger Hamiltonian."

8. "What do I care?"

7. "Home? I've been working over at CMSE."

6. "You stupid piece of ----!"

5. "Obviously you don't understand the principle behind this."

4. "Done? You're not done yet!"

3. "O.K. Here's what you're doing wrong."

2. "No one is interested in this work anymore so let's publish and move on."

1. "No Honor. No Code."